ISBN 978-82-326-4558-9 (printed version)
ISBN 978-82-326-4559-6 (electronic version)
ISSN 1503-8181

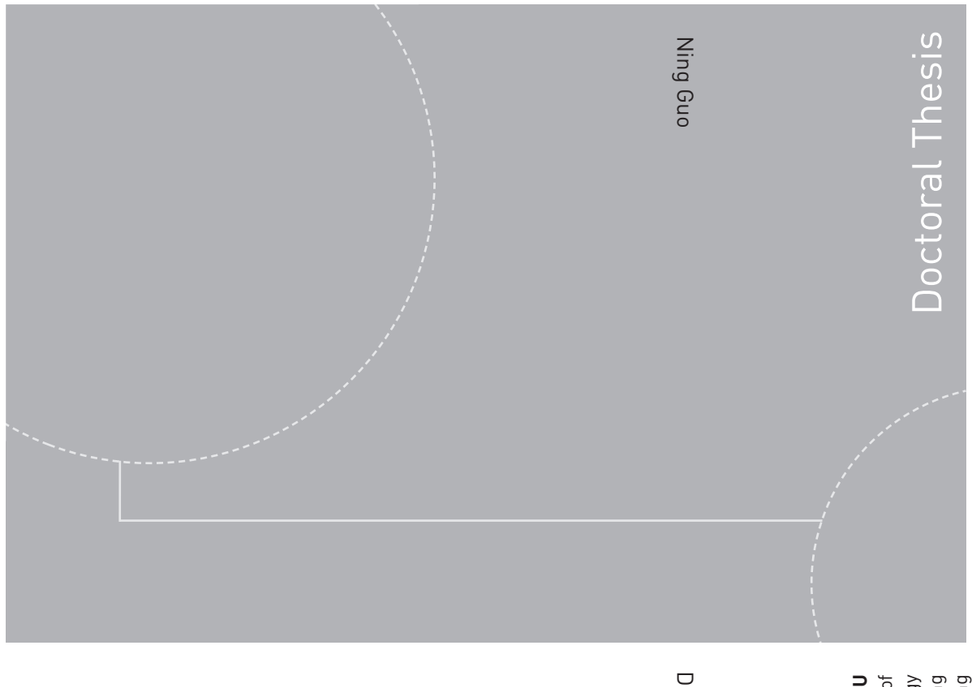

Doctoral theses at NTNU, 2020:103

Ning Guo

Modelling of reacting multi-phase flow for biomass gasification

A realistic approach of particle hydrodynamics and heat transfer under entrained flow gasification conditions

NTNU
Norwegian University of
Science and Technology

NTNU
Norwegian University of
Science and Technology

NTNU
Norwegian University of
Science and Technology
Faculty of Engineering
Department of Energy and Process Engineering

Doctoral theses at NTNU, 2020:103

NTNU

Ning Guo

Modelling of reacting multi-phase flow for biomass gasification

A realistic approach of particle hydrodynamics and heat transfer under entrained flow gasification conditions

Thesis for the degree of Philosophiae Doctor

Trondheim, March 2020

Norwegian University of Science and Technology
Faculty of Engineering
Department of Energy and Process Engineering

NTNU
Norwegian University of
Science and Technology

NTNU
Norwegian University of Science and Technology

Thesis for the degree of Philosophiae Doctor

Faculty of Engineering
Department of Energy and Process Engineering

ISBN 978-82-326-4558-9 (printed version)
ISBN 978-82-326-4559-6 (electronic version)
ISSN 1503-8181

Doctoral theses at NTNU, 2020:103

Printed by Skipnes Kommunikasjon as

PREFACE

This doctoral thesis is carried out at Norwegian University of Science and Technology (NTNU) under the supervision of Professor Terese Løvås and Associate Professor Tian Li.

The simulations of this work are conducted within the GAFT project (Gasification and FT-Synthesis of Lignocellulosic Feedstocks). The project is led by SINTEF Energy AS and funded by the Research Council of Norway, Avinor, Silva Green Fuel AS, Viken Skog SA, CAMBI ASA and ECOPRO AS. In addition, UNINET Sigma2 and NTNU HPC Group provided computational resources.

The experiments in this thesis were conducted at Division of Energy Science of Luleå University of Technology in Sweden, supported by Norbotten Research Council and Kempe Foundation.

In addition, the DNS data used in this work is supported by Research Council of Norway and Nature Science Foundation of China.

ABSTRACT

Entrained flow gasification of pulverized biomass is considered as one of the potential technology routes to produce syngas, which later can be used to produce second generation of biofuels via Fisher-Tropsch (FT) synthesis. To understand this process, modelling reacting multi-phase flows of biomass gasification is of interest. Computational fluid dynamics (CFD) simulations is a well-practiced tool to simulate such processes.

In many CFD simulations, biomass particles are assumed to be spherically shaped. This assumption is not in line with reality and could cause deviations from experiments, and its effects on simulation accuracy in terms of particle hydrodynamics and thermochemical conversions are not well investigated. As a first step to study this problem, a spheroidal shape assumption is made for pulverized particles and drag and torque models for spheroids are implemented into the open source CFD platform, OpenFOAM. It is then validated against various experiments and direct numerical simulation (DNS) data. This validated model is then applied to conduct non-reactive simulations in a configuration similar to entrained flow gasification of pulverized biomass. When compared with the traditional spherical method, this spheroid model predicted more diverse distributions of particle residence time and local concentrations, which may alter particle thermochemical conversion under reactive condition.

To investigate the aforementioned effects under reactive conditions, biomass particle gasification experiments are conducted in a laminar flat flame drop tube reactor to

build the basis for reactive simulations validation. Particles of two different aspect ratios are gasified, both are tested at two available carrier gas flow rates. Particle velocity, size and volumetric information are obtained based on experiments. Delayed onset of dispersed soot incandescent matter is observed, probably due to heating rate caused by high flow rates of carrier gas and high particle volume fractions. Particle shape is seen to change in a heterogeneous way and influenced by particle heating rate, particle aspect ratio and carrier gas flow rate. Radial migration and rapid deceleration are also recorded. Particle alignment angles tend to be close to 0°.

Furthermore, a heat transfer model and a new set of devolatilization kinetic parameters suitable for fast heating rates, high temperatures and short residence times are further implemented in OpenFOAM. By comparing particle axial velocity, these model combinations are then validated against the drop tube experiments above under reactive conditions. Simulation results also point out that the radial migration and rapid deceleration of particles are very likely to be caused by fast release of volatiles, and particle alignment angles are probably dependent on gas flow velocity gradients. With the validated model combinations, four cases with different shapes, hydrodynamics and heat transfer approaches are configured to execute reactive simulations of conditions similar to entrained flow gasification of pulverized biomass, and their results are thereafter compared. Differences in particle velocity and conversion histories can be clearly observed. The Kishore-Gu model favors particle heat transfer and benefits drying and devolatilization greatly. However, the sphere and simplified non-sphere model predict 61% and 43% longer residence time than the spheroidal ones respectively, which helps slow processes like char conversion. These effects are somewhat contradicting what one would expect, and further investigation with more comprehensive and realistic operating conditions are recommended.

LIST OF SELECTED PAPERS

This thesis is based on the following selected journal papers, referred to in the text by Roman numerals.

1. **Guo, Ning**; Li, Tian; Zhao, Lihao; Løvås, Terese.
   Eulerian-Lagrangian simulation of pulverized biomass jet using spheroidal particle approximation
   Fuel, Volume 239, 1 March 2019, Pages 636-651
2. Llamas, Ángel David García; **Guo, Ning**; Li, Tian; Gebart, Rikard; Løvås, Terese; Umeki, Kentaro.
   Particle morphology, orientation and volume fraction of biomass particles with different aspect ratio in a jet flow during devolatilization
   (Submitted to *Fuel*, currently under review)
3. **Guo, Ning**; Llamas, Ángel David García; Li, Tian; Umeki, Kentaro; Gebart, Rikard; Løvås, Terese.
   Computational fluid dynamic simulations of pulverized biomass conversion using spheroidal approximation
   (Accepted for publication in *Fuel*)

AUTHOR'S CONTRIBUTIONS

The selected papers are co-authored. The contributions of the author to the selected papers are listed as below.

Paper 1. Associate Professor Tian Li proposed the research idea and plan, offered guidance in OpenFOAM training and put efforts in code debugging. The author has performed literature research, implemented the spheroid model into OpenFOAM, and then verified and validated the model. Associate Professor Lihao Zhao also contributed in verifying particle torque. In addition, the author conducted all the non-reactive simulations in comparing three different particle models in a configuration similar to entrained flow gasifier. The findings were jointly evaluated with the co-authors. The manuscript was written by the author and reviewed by all the co-authors.

Paper 2. The author conducted the experiments and analyzed results, jointly with Mr. Ángel David García Llamas. Mr. Ángel David García Llamas conducted literature review, processed all the experimental data and wrote the manuscript. All authors also contributed in reviewing the manuscript.

Paper 3. The author performed literature review, executed simulations, post-processed all the data and wrote the manuscript. The results were jointly analyzed with the co-authors, who also contributed in reviewing the manuscript.

In addition to the selected papers above, additional findings on effects of rapid release of volatiles are presented in Chapter 5.4. For this chapter, the author conducted the experiments and analyzed results, jointly with Mr. Ángel David García Llamas.

Associate Professor Tian Li also helped to analysis the results. The author also conducted all the simulation.

ADDITIONAL PUBLICATIONS AND PRESENTATIONS

Additional paper(s) published during the Ph.D. studies

- Finnerman, Oskar; Razmjoo, Narges; **Guo, Ning**; Strand, Michael; Ström, Henrik. (2017).
  Reactor modelling assessment for urea-SNCR applications.
  International journal of numerical methods for heat & fluid flow, 27(7), 1395-1411.

Additional paper(s) in progress during the Ph.D. studies

- Llamas, Ángel David García; **Guo, Ning**; Li, Tian; Gebart, Rikard; Løvås, Terese; Umeki, Kentaro.
  Jet effect, transitory swelling and fast deceleration of biomass particles during devolatilization.
  (In progress, subject to change)

Conferences and presentations

- **Guo, Ning**; Li, Tian; Løvås, Terese. (2017)
  Eulerian-Lagrangian Simulation of Non-Spherical Biomass Particles in Turbulent Flow. *(Visual presentation)*

Sixteenth International Conference on Numerical Combustion; Orlando, United States. 2017-04-03 – 2017-04-05.

- **Guo, Ning**; Li, Tian; Zhao, Lihao; Løvås, Terese. (2017)
  Eulerian-Lagrangian simulations of spheroidal biomass particles in turbulent flows. *(Visual presentation)*
  Nordic Flame Days 2017; Stockholm, Sweden. 2017-10-10 – 2017-10-11.
- **Guo, Ning**; Li, Tian; Løvås, Terese. (2018)
  Eulerian-Lagrangian simulations of pulverized biomass injection in turbulent flows using spheroidal approximation. *(Visual presentation/published as Paper 1)*
  2nd International Workshop on Oxy-Fuel Combustion; Bochum, Germany. 2018-02-14 – 2018-02-15.
- **Guo, Ning**; Li, Tian; Løvås, Terese. (2018)
  Eulerian-Lagrangian Simulation of thermochemical conversion of pulverized biomass particles using spheroid assumption. *(Poster)*
  37th International Symposium on Combustion; Dublin, Ireland. 2018-07-29 – 2018-08-03.
- **Guo, Ning**; Llamas, Ángel David García; Li, Tian; Umeki, Kentaro; Gebart, Rikard; Løvås, Terese. (2019)
  CFD simulation of pulverized biomass conversion using spheroidal approximation. *(Visual presentation)*
  17th International Conference on Numerical Combustion; Aachen, Germany. 2019-05-06 – 2019-05-08.
- **Guo, Ning**; Llamas, Ángel David García; Li, Tian; Umeki, Kentaro; Gebart, Rikard; Løvås, Terese. (2019)
  Jet - like force due to rapid moisture and volatile release during thermochemical conversion of biomass. *(Visual presentation)*
  Nordic Flame Days 2019; Turku, Finland. 2019-08-28 – 2019-08-29.

ACKNOWLEDGEMENT

From China, to Sweden and eventually to Norway, the quest to pursue a doctorate degree has been demanding and overwhelming. I would like to take this opportunity to thank the people for helping me to achieve this.

Professor Terese Løvås is my main supervisor. I would like to thank her for giving me this valuable opportunity to carry out this project. Furthermore, I also deeply appreciate her providing me a comfortable working environment and giving strategic opinions on the big picture of this project.

Associate Professor Tian Li (李田) acts as my co-supervisor in this Ph.D. project and manages day-to-day operations. With patience and kindness, he has constantly offered me critical scientific inputs and academic guidance. I would like to express my gratitude to him.

Mr. Ángel David García Llamas is the important scientific partner in this project. He introduced the world of experiments to me as a modeler. Furthermore, he has spent endless time discussing research results with me and contributed greatly in Paper 2 and 3, and even more papers in the future. He is acknowledged here for his contributions, both professionally and personally.

Associate Professor Lihao Zhao (赵立豪) offered his insightful expertise in particle hydrodynamics of spheroids. Professor Kentaro Umeki (梅木健太郎) and Professor Rikard Gebart have been very helpful in accommodating me in my research stay in Luleå and providing me scientific guidance in the experimental campaign.

My colleagues in the department have been very helpful and supportive, both professionally and personally. To begin with, I would like to acknowledge Professor Helge I. Andersson, Dr. Kathrin Weber, Dr. Fredrik Grøvdal and Dr. Niranjan Reddy Challabotla for their scientific input in the selected publications. In addition, Karl Oskar, Christoph, Haoshui (于浩水), Jingyuan (张景远), Jonas, David, Matias, Donghoi, Xingji (俞星吉), Bjørn, Ahfaz, Corinna, Michal and others at NTNU have been pleasant colleagues at work. Furthermore, all the support I received from the administration staff is greatly appreciated.

I am grateful to have Tianyi Zheng (郑天轶), Yuting Liu (刘雨婷), Yangwei Guan (关洋威), Mingzhe Yu (俞明辙), Abhilash Ram, Christopher Vannas and Kyle MeCallum in my life and give me support in my hour of need. In the end, I would like to thank my parents for investing in my education and holding the fundamental belief that “If anything is to be impoverished, it is not education.”

TABLE OF CONTENTS

LIST OF FIGURES

LIST OF TABLES

ABBREVIATIONS

A	Pre-exponential constant [s^{-1}]
A_{ca}	Maximum cross-sectional area that is perpendicular to major axis [m^2]
A_s	Particle surface area [m^3]
a, b, c	Particle axial radius [m]
B_i	Modelling coefficient (i =1, 2, 3, 4) [-]
C_D	Drag force coefficient [-]
d_p	Particle diameter [m]
E	Activation energy [$J \cdot kmol^{-1}$]
F_{rocket}	Rocket force [N]
h	Heat transfer coefficient [$W \cdot m^{-2} \cdot K^{-1}$]
m_{devol}	Mass of the remaining volatiles in the particle [kg]
m_{mois}	Mass of moisture released [kg]
m_{vol}	Mass of volatiles released [kg]
Nu	Nusselt number [-]
Pr	Prandtl number [-]
$\dot{Q}$	Heat rate [W]

R	Universal gas constant [$J \cdot K^{-1} \cdot kmol^{-1}$]
Re, Re_p	Reynolds number [-]
S	Efficiency factor [-]
T_s	Surrounding temperature [K]
T_p	Particle temperature [K]
t	Time [s]
x, y, z	Cartesian coordinate [-]
κ_f	Fluid thermal conductivity [$W \cdot m^{-1} \cdot K^{-1}$]
λ	Particle aspect ratio [-]
ρ_g	Gas density [$kg \cdot m^{-3}$]
τ_k	Kolmogorov time scale [s]
τ_p	Particle response time for Stokes flow [s]
Φ	Overall sphericity [-]
$\Phi_{/\!/}$	Lengthwise sphericity [-]
$\Phi_{\perp}$	Crosswise sphericity [-]

1 INTRODUCTION

1.1 From biomass to biofuel

Global warming presents worldwide challenges and requires everyone to contribute to reduce greenhouse gas emissions. As shown in Fig. 1, nearly one quarter of global emissions in 2016 were generated by the transport sector, and road and air transportation make up 86% of them [1]. This is no surprise as the transport sector is dominantly driven by fossil fuels. Various attempts are made to address this problem and liquid biofuel is one of the options on the table. Like any other green energy sources, biofuels can be close to carbon neutral if they are produced in an environmentally friendly manner. In addition, the "drop-in" feature of biofuels makes them an advantageous choice because it can be used without major infrastructure modification. This can be very relevant, for example, in conservative industries such as marine and aviation applications [2].

Biofuels are mainly classified as first and second generation biofuels based on their source of biomass [3]. First generation biofuels are produced from food crops, such as corn and sugar cane [3][4]. The production of first generation biofuels is well developed in the last decades, but it raises concerns in feedstock sustainability [3][4]. In contrast, the second generation refer to non-food based biomass, such as wood, forest residuals, household waste, but further developments of its production technology are in demand [4]. It should also be noted that a third generation of biofuel, defined as biofuels produced from crops (such as algae and fast-growing trees) that

are designated for energy production, is also proposed, however it is out of the scope of this thesis and is not discussed further [5].

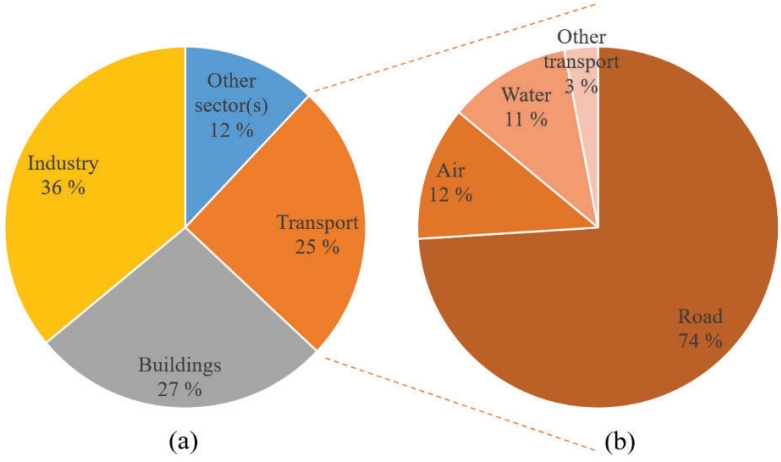

Fig. 1 Global CO_2 emissions in 2016 [1].
(a) by sector; (b) by sub-sector in the transport sector.

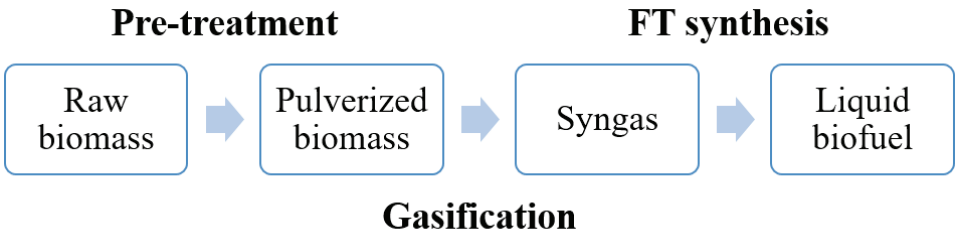

Fig. 2 One possible technological option to convert raw biomass to liquid biofuels.

Second generation biofuels can be produced from woody biomass. Fig. 2 presents a simplified potential technological route to convert raw biomass material to liquid biofuels. First, raw biomass materials are pre-treated and then pulverized to very small biomass particles. Afterwards, pulverized biomass particles are gasified, and syngas is produced. In the end, Fischer-Tropsch synthesis is used to convert produced syngas to liquid biofuels and other valuable chemicals [6]. Therefore, it is of interest to

understand the gasification process of pulverized biomass where the thermochemical conversion of the pulverized biomass takes place.

1.2 Thermochemical conversion of coal and biomass

Similar to coal, biomass thermochemical conversion processes, such as pyrolysis, gasification and combustion, usually consist of three overlapping stages as shown in Fig. 3:

- Drying: biomass particles are heated up and moisture are released from the biomass particles.
- Devolatilization: volatiles (gas and tars) are released and solid dry biomass particles are transformed to char and ash.
- Char conversions and homogenous gas reactions: reactions of surrounding gas mixture and char occur, and produce a non-condensable gas, a condensable gas and solid residuals.

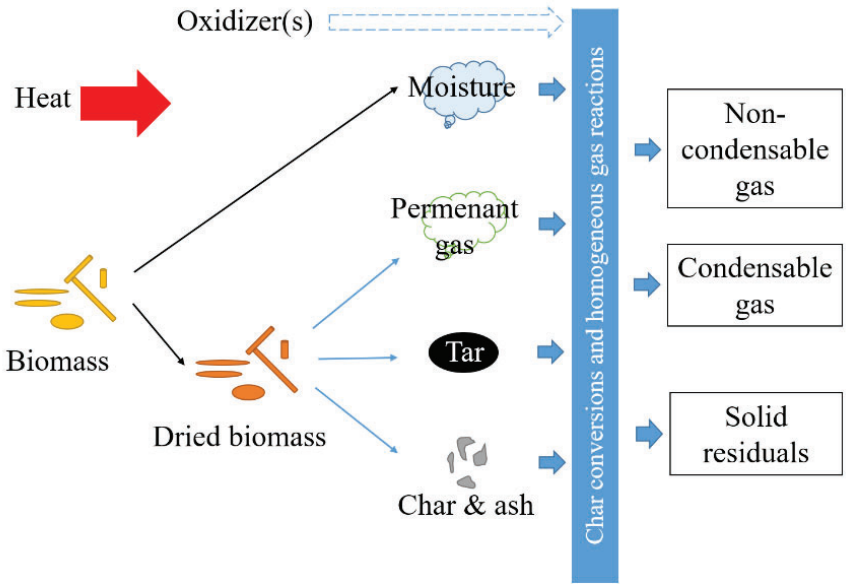

Fig. 3 Thermochemical conversion stages of biomass.

Although pyrolysis, gasification and combustion share great similarities, one should also note that their operating conditions and purposes differ from one to another.

Pyrolysis happens in the absence of oxidizers at elevated temperatures where biomass materials go through thermal degradation and produce condensable vapors (tar), non-condensable gases (CO_2, CO, CH_4, H_2, etc.) and solid residuals (char, ash, etc.) [7]. Depending on the conditions and purposes, pyrolysis can be further classified as slow and fast pyrolysis: slow pyrolysis is characterized by lower temperatures and longer residence times and aims to produce bio-char, while fast pyrolysis occurs at higher temperature under shorter residence time with bio-oil as the main product [8].

When additional oxidizers, usually air or pure oxygen, are supplied with the intention of complete the oxidization of biomass, it is referred to as combustion. The main goal of combustion is energy and heat generation [9].

When only partial oxidization is reached due to reduced amount of oxidizers supplied, the process is called gasification with the aim of producing gaseous fuels (syngas) from solid biomass [10]. Steam, oxygen and air are usually used as oxidization agents [10].

Based on the above, one can use the amount of oxidizers supplied to the system as an indicator to distinguish these three process, given that the temperature is high enough to initiate reactions. Oxidizer-fuel equivalence ratio is often used for this purpose. It is defined as the actual oxidizer-fuel ratio over the oxidizer-fuel ratio under stoichiometric complete combustion conditions. Pyrolysis happens at equivalence ratio of 0 (i.e. absence of oxidizer). For gasification, the equivalence ratio is held less than 1, meaning there is not enough oxidizer for complete oxidization of the fuels. When equivalence ratio is equal to or usually more than 1, it will be classified as combustion, where stoichiometric or excess oxidizer is provided. It does however not mean that only one process occurs at any given time. For example, biomass particles in practice will not be evenly distributed in a gasifier, so there are localized regions where the amount of fuels is limited, but the amount of oxidizer is abundant, as a result, combustion occurs in these region despite the overall equivalence ratio of the

gasifier is less than 1. Similar arguments could be made for other scenarios, hence pyrolysis and combustion zones listed in a gasification process in Table 1 below.

1.3 Gasification technology

As the motivation of the thesis is to understand better the production of syngas from biomass to liquid biofuel, it is gasification technology that is relevant in this context and discussed further. As presented in Table 1, various literatures use four simplified zones to describe the gasification process in terms of kinetic modelling [4]. Drying, pyrolysis, combustion and reduction zones correspond to the three stages in Chapter 1.2, respectively.

Table 1 Four reaction zones in gasification [4].

Zone	Major reactions	ΔH [kJ/mol]	Note
Drying	Moist biomass → dry biomass + H_2O	>0	
Pyrolysis	Dry biomass → char (+ash) + volatiles	>0	
Combustion	$C + O_2 \rightarrow CO_2$	-394	Char combustion
	$C + O_2 \rightarrow CO$	-111	Char partial oxidation
	$H_2 + O_2 \rightarrow H_2O$	-242	Hydrogen combustion
Reduction	$C + CO_2 \rightarrow CO$	172	Boudouard reaction
	$C + H_2O \rightarrow CO + H_2$	131	
	$CO + H_2O \rightarrow CO_2 + H_2$	-41	Water gas shift reaction
	$C + H_2 \rightarrow CH_4$	-75	

Various forms of gasification technology exist with fixed bed gasification, fluidized bed gasification and entrained flow gasification being the most common ones [4].

In a fixed bed (see Fig. 4), or moving bed gasifier, biomass materials are usually gasified via gasifying agents (steam, air, oxygen, etc.) [11]. Depending on the moving direction of the solid biomass feedstock and the gases, updraft or downdraft fixed bed gasifier are commonly available [12]. In an updraft gasifier, the gasifying agents are introduced from the bottom of the gasifier while the biomass fuels are injected from the top, then syngas leaves from the top of the gasifier [13]. In a downdraft gasifier, gasifying agents contact and react with biomass fuels along the downward direction [13]. Fixed bed gasifiers are simple to construct, but are limited to a few MW as it is difficult to maintain regular conversion in a wider bed configuration [10][12].

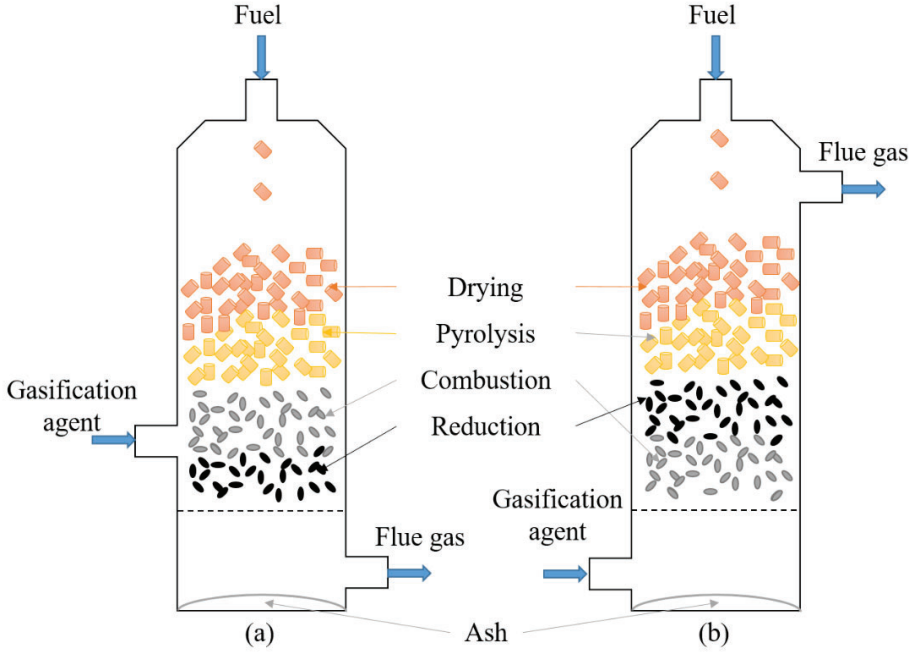

Fig. 4 Fixed bed gasifier.
(a) downdraft; (b) updraft.

In a fluidized bed gasifier (see Fig. 5), inert materials (such as sand) are in addition introduced into the bed of the gasifier and gasifying agents are injected from the bottom of the bed via distribution grids at 1 – 3 $m \cdot s^{-1}$ [4]. The inert materials and fuels behave like fluids with gas bubbles stirring the gasifier continuously, which leads to better mixing and heat transfer between fuels and gasifying agents [12][14]. Consequently, fluidized bed gasifiers are very flexible on fuel and load choices and can operate almost under isothermal conditions, which in turn reduces difficulties in temperature control [14]. However, fluidized bed gasifiers operate at relatively low temperature (800 – 900 °C) and have short gas residence times, which result in tar contamination and thus relatively reduced carbon conversion are inevitable [14].

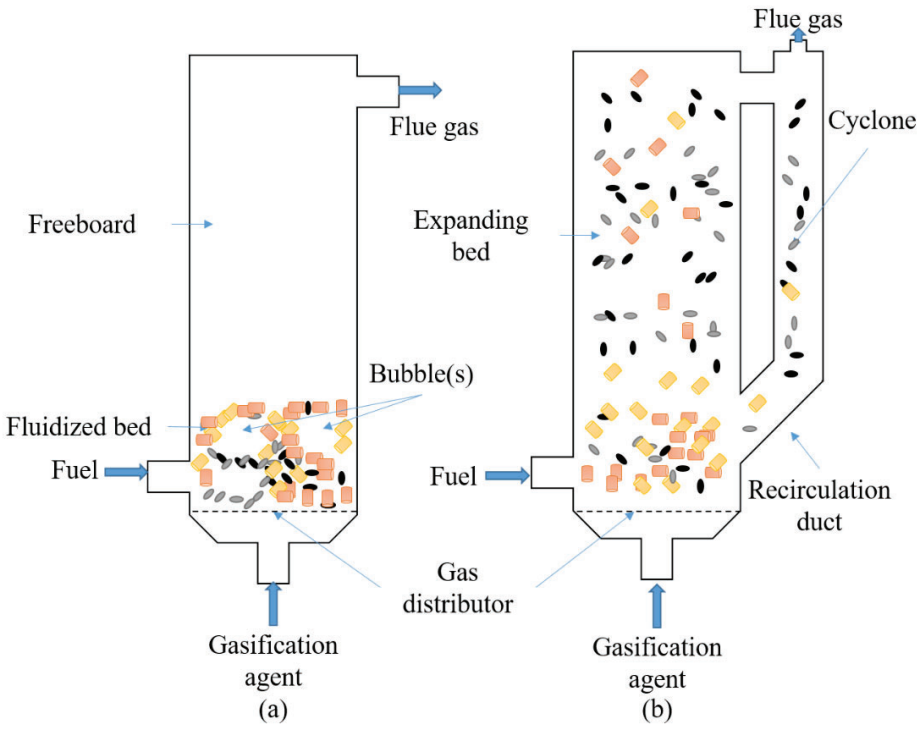

Fig. 5 Fluidized bed gasifier.
(a) bubbling; (b) circulating.

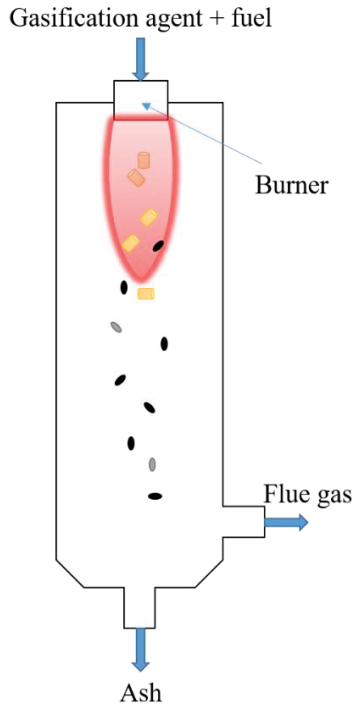

Fig. 6 Entrained flow gasifier.

In an entrained flow gasifier (see Fig. 6), fuels and gasifying agents are typically injected co-currently to the gasifier and operates at high temperatures (1300 – 1500 °C) and often high pressures (25 – 30 bar) [4]. Such operating conditions promote higher carbon conversions and can significantly reduce tar formation [4]. However, soot produced at such high temperatures imposes technical challenges due to the high volatile content of biomass [15]. In addition, the particles have typically very short residence times in these systems [4]. Qin et al. [15] conducted experiments in a reactor of 2 m height and reported the residence time to be approximately 2 – 3 s. Therefore, reducing the size of the biomass materials is often necessary to ensure better heat transfer and mixing and particle median size is usually reduced to a few hundred of microns [15][16]. Pre-treatment methods such as torrefaction are usually applied to improve the fuel homogeneity, and to reduce the energy consumption during the size reduction process [4]. It is worth noting that given the short residence time, it becomes

crucial to accurately model particle hydrodynamics when simulating entrained flow gasification processes. The work presented in this thesis is intended to address this very issue by employing a spheroid model framework to better model particle hydrodynamics.

In summary, biomass particles are required to have smaller sizes in entrained flow gasifiers than the other two types of gasifiers. Syngas from entrained flow gasifiers have better quality (higher production of syngas with less amount of tar) than the other two. Moreover, both entrained flow and fluidized bed gasifiers are more flexible in scaling up than fixed bed gasifiers.

Apart from the aforementioned three typical kinds of gasifiers, there are also other types of gasifiers such as rotary kiln reactor and plasma reactor, and interested readers can refer to the review paper of Molino et al. [4], where a detailed comparison of advantages and disadvantages of different gasifiers is also presented.

1.4 Biomass, a fuel with fibrous structure and irregular shape

Biomass comes from various sources and can be generally classified into four sub-categories: woody biomass, herbaceous biomass, fruit biomass, and blends and mixtures [17]. They are composed of organic polymers, cellulose, hemicellulose and lignin, and minor materials [18]. The mass fraction of cellulose, hemicellulose and lignin in biomass are 40 – 60 %, 15 – 25 % and 15 – 25 %, respectively [18]. Cellulose has a high linearity and contributes to the fibrous nature of biomass [18][19]. Hemicellulose is less linear and lignin is the least, both of them act as binding agents for cellulose in the cell walls [18][19].

Coal and biomass share great conceptual similarities. Both consist of moisture, volatiles, fixed carbon, ash, etc. However, attention should also be paid to their differences. Biomass generally have higher amount of volatiles and moisture and less ash, hence its composition and properties vary more than coal [20]. When compared to pulverized coal particles, pulverized biomass particles usually have larger size, less

density and larger deviation from a spherical shape [21]. These factors greatly affect particle motions and conversion histories [21][22]. In addition, heat and mass transfer within a biomass particle is anisotropic due to its microstructure [18]. Pre-treatment of raw biomass materials are often required to decrease their heterogeneity in size and composition [4].

A very important factor to consider when modelling pulverized biomass particles is their irregular shape. It is common to treat them as spheres in the modelling community [23][24][25], which is easy to implement in simulations given the sphere's one dimensionality in modelling. However, this assumption oversimplifies reality. It has been shown experimentally that biomass such as Norwegian spruce, forest residuals, milled wood, palm kernel expeller, pulverized Miscanthus and beechwood particles are irregularly shaped [26][27][28]. Misrepresenting their shapes could potentially make simulation results less representative of reality, under both non-reactive and reactive conditions.

Under non-reactive conditions, this spherical particle shape assumption can lead to inaccurate modelling results in terms of particle hydrodynamics as particle shape affects particle forces. Wachem et al. [29] conducted a DNS-LES study on particle behavior in horizontal turbulent channel flows with particles of different shapes: a sphere, two ellipsoids with different aspect ratios, a disc and a fiber. When simulation results of particle velocity and concentration were compared, differences were found between simulations with spherical particles and simulations of other shaped particles. Another major flaw in the spherical assumption is that particle orientations and rotations are difficult to model or not modelled at all. Njobuenwu and Fairweather [30] have simulated inertial fibres in turbulent flows and found that the particle aspect ratio and velocity gradient of flow fields could strongly influence particle alignment distribution, and neglecting this could also make particle motions in simulations deviate from reality. All of these works indicate that the choice of shape in modelling pulverized biomass particles impacts their hydrodynamic behaviors, such as trajectories and residence times, and it is likely to have implications under reactive conditions.

When thermochemical reactions are considered, other additional factors can contribute to deviations between experiments and simulations. With different choices in particle shapes, particle surface area to volume ratio varies, which affects particle heat and mass transport process. For single particles, Li and Zhang [31] found analytically that char combustion rate increases as particle aspect ratio increases. Lu et al. [32] also found that particle shape affects particle devolatilization rate in experiments. For multi-particles, Yin et al. [22] conducted CFD simulations of co-firing biomass and coal using two shape assumptions of biomass particles, obvious differences of simulation results could be seen. All the above imply that particle shapes can influence biomass thermochemical conversion process and should be duly accounted for in modelling reacting multi-phase flow of biomass gasification.

1.5 Thesis objectives and scopes

As mentioned previously, it is of importance to accurately model particle shapes, in terms of hydrodynamics as well as mass and heat transfer. Numerous works have tried to address the aforementioned issues and an overview could be found in the review article of Tabet and Gökalp [21]. Even though a lot of efforts are made, the following fronts are rarely covered:

- Experimental data on particle velocimetry and orientation under gasification conditions with high heating rates and high temperatures;
- A quantitative comparison of commonly used approaches in modelling biomass particle under conditions similar to entrained flow gasification process.

The objectives of the thesis are to provide further details to these problems with the following logic:

- Implement, verify and valid a new particle shape model which considers biomass particle shape and directionality in a multi-phase CFD solver.
- Compare commonly used particle models quantitatively under non-reactive conditions similar to entrained flow gasification process.

- Conduct multi-particle drop tube experiments and obtain particle experimental data.
- Compare commonly used particle models quantitatively under reactive conditions similar to entrained flow gasification process.

Given the above, the thesis places emphasis on shape effects on particle hydrodynamics, surface areas and heat transfer. It should be noted that particle thermochemical kinetics and turbulence modelling of surrounding flows are not the focus of this thesis and therefore not examined in detail.

1.6 Thesis organization

This thesis aims to provide a comprehensive overview of the selected papers with more relevant background information. In the meantime, the author would also like to avoid unnecessary repetition on the topics that are already intensively covered in the selected papers. With such consideration, this thesis follows the structure below, so it could describe the essences of the selected paper in a compact and efficient manner while put more efforts on relevant research areas that are *not* included in the selected papers.

Chapter 2 covers a literature review for experiments and simulations of thermochemical conversions of biomass particles. Entrained flow gasification of biomass is emphasized in this chapter.

Chapter 3 presents the modelling theory and methodology. First, a general overview of modelling approaches in simulations of reacting multi-phase flows is given. Then a summary of forces acting on particles is presented. In the end, the heat transfer and devolatilization models for biomass are discussed.

Chapter 4 describes the experimental aspects that this thesis is based on. It consists of experimental configuration and their purposes in this thesis.

Chapter 5 summarizes the work of selected papers and discusses the effects of rapid release of volatiles.

Chapter 6 summarizes the main conclusions and recommends potential future work that can be done.

2 REVIEW OF RELEVANT STUDIES

The primary focus and research efforts of the selected papers are on the hydrodynamic aspects of biomass particles and their influences on the thermochemical conversion histories of particles in an entrained flow gasifier. However, less attention was paid to other aspects, such as fuel pre-treatment, entrained flow gasifier operation, chemical kinetics, etc., despite their importance. Therefore, this chapter aims to compensate such shortcomings by providing readers a review of relevant experiment and simulation studies.

This chapter is organized into two parts. Chapter 2.1 presents widely cited comprehensive literature review papers, whereas Chapter 2.2 selects and summarizes several recently published studies on specific topics.

2.1 Summary of relevant literature review papers

Selected literature review papers are summarized here. It aims to provide a simple guide for readers not familiar with the field in order to quickly get familiarized with fundamental knowledge relevant to the thesis topic.

As mentioned in Chapter 1.2, pyrolysis shares great similarities with gasification, especially in the drying and devolatilization stages. Therefore, the review of Di Blasi [33] on modeling chemical and physical processes of wood and biomass pyrolysis is very relevant. In this review, chemical kinetics, transport and reactor models were discussed in detail. Additionally, Pecha et al. [18] also published a review in 2019 and discussed chemical reactions, heat transfer, mass transfer and phase change of intra-

particle phenomena during lignocellulose pyrolysis. In this review, more in-depth description on biomass fibrous structures and components is provided.

Char conversion is the stage that readers should pay attention regarding the differences between gasification and pyrolysis. Di Blasi [34] later published another review on combustion and gasification rates of lignocellulosic chars. In this review, char yields and reactivity were discussed. With the above, readers are expected to have a basic understanding of gasification, as well as pyrolysis and combustion, in particle level.

The reasonable next step is to scale up from single particle level to the reactor or gasifier level. First, a good understanding of gasification technology in general is needed. Sikarwar et al. [35] reviewed the recent advances in gasification technology and discussed traditional and novel design of gasification technology, feedstock, effects of feedstock properties and operating conditions on system performance, tar formation, power generation approaches, modelling methods and social-environmental impacts. Molino et al. [4] also compared the advantages and disadvantages of different gasifiers in a very detailed way. This gives readers a general concept of various aspects in gasification.

For modelling purposes, Haberle et al. [19] presented a review on thermal degradation modelling of thermally-thick particles. In this review, a framework for modelling a small-scale furnace was proposed, which included certain modelling aspects for accurate simulations, from particle level to reactor level. This framework could be used as a guide when modelling an entrained flow gasifier of biomass.

The selected review papers above represent the necessary background for modelling of reacting multi-phase flow of biomass gasification, from particle level to reactor level, which form the basis that the thesis is built on.

2.2 Recent progress in entrained flow gasification of biomass

This Ph.D. project is a part of a bigger research project, Gasification and FT-Synthesis of Lignocellulosic Feedstocks (GAFT), which covers the following four aspects:

- Feedstock knowledge and pre-treatment of biomass;
- Experimental and modelling studies of entrained flow gasification;
- FT-synthesis;
- Value-chain analysis.

The Ph.D. work was designed to carry out the simulations of gasification processes. There are some aspects of the overall value chain as represented in the GAFT project, that are directly relevant to entrained flow gasification simulations of biomass. However, they are not covered in the papers included in this thesis. For example, in terms of pre-treatment of raw biomass, torrefaction is especially relevant for the entrained flow gasification when compared to other gasification techniques. When it comes to entrained flow gasification, adequate monitoring, measurement and diagnostic methods are needed to conduct experimental studies and build groundwork for simulation investigations. In addition to experimental perspective, better char conversion models, in retrospect, should have been used in the simulations. Regarding the FT-synthesis and value chain analysis, information on gasifier performance is of interest. Following the logic above, some recently published papers on the aforementioned four aspects are respectively summarized and discussed below as a remediation for their absence in the selected papers.

2.2.1 Torrefaction

Raw biomass material usually have high moisture content, low energy density, heterogeneous size and irregular shape distribution [26][36]. It is therefore an advantage to upgrade the raw materials to better quality fuels before feeding them into an entrained flow gasifier. One common method is torrefaction, during which raw biomass materials are heated around 230 – 350 °C for 1 – 60 mins at the absence of oxygen [26][37]. Volatiles are released in the form of torrefaction gas, as a result, oxygen content is decreased and carbon content is increased [26][37]. When compared to raw materials, torrefied biomass materials usually have higher energy density, better grindability, improved fluidization behaviors and more uniformed distributions of properties [38]. Given the importance of torrefaction, several papers

are listed below to present their effects on gasification performance, where both woody and non-woody biomass, experimental and modelling approaches were used.

He et al. [39] used poplar wood to study effects of torrefaction on char gasification reactivity, kinetics and mechanism. Different torrefaction temperatures (200, 250 and 300 °C) and four pyrolysis temperatures (600, 700, 800 and 900 °C) were tested. Thermogravimetric analysis experiments were conducted to access the bio-char reactivity and kinetics. Results shows that torrefaction under low temperature only affected char reactivity slightly, while severe torrefaction could lead to reduced char reactivity.

However, reactivity and kinetics obtained at low temperatures or heating rates are usually difficult to be applied to the conditions in an entrained flow gasifier. Li et al. [40] put raw and torrefied forest residues in a drop tube reactor under high temperature (1473 K) and high heating rate (more than 10^4 $K \cdot s^{-1}$) to study the effects of torrefaction on physical properties and conversion behaviors of char. It was found that the effects of torrefaction on particle morphology is significant. The volume-mean value of particle size after devolatilization is larger for torrefied forest residues when compared to non-torrefied ones, probably due to fragmentation differences during devolatilization. In addition, torrefaction was found to result in char having lower reactivity, lower O/C ratio, lower amount of catalytic alkali metal and more aromatic carbon structure. Li et al. [26] further investigated behavior of raw and torrefied Norwegian spruce, as well as forest residuals, using drop tube reactor experiments and CFD simulations. When compared to raw materials, torrefied biomass was found to have higher char yields. Torrefaction was also found to affect organic composition of char. In addition, a two-competing-rates devolatilization model was proposed and could well predict mass loss and evolution of organic composition of char. Ku et al. [41] also conducted CFD simulations of a high temperature (1400 °C) entrained flow reactor to study the influences of torrefaction. Four kinds of feedstocks, forest residues and spruce in both raw and torrefied states, were employed in the simulations. Different excess air ratios, steam to carbon ratios and particle sizes were simulated and tested. It was found that torrefaction leads to lower H_2 production and carbon

conversion. Therefore, longer residence times for gasification of torrefied biomass may be required, compared to raw biomass.

Besides woody biomass, non-woody biomass has also been studied. For example, Brachi et al. [42] studied effects of torrefaction of tomato peels. Experiments of ultimate analysis were conducted on four feedstocks, raw tomato peels and three different torrefied solids produced under three different torrefaction conditions (200 °C, 240 °C and 285 °C, respectively, all 30 minutes). Based on the data from ultimate analysis, chemical equilibrium models were used to simulate raw and terrified tomato peels respectively in entrained flow gasifiers. Even though torrefaction is advantageous in biomass feeding, grinding, storage, CO and H_2 production, it was found that improvements of product gas quality by torrefaction were only marginal for tomato peels under the studied conditions.

In summary, the above highlights the importance and effects of torrefaction as part of pre-treatment for biomass materials before they are fed into entrained flow gasifiers.

2.2.2 Monitoring, measurements and diagnostics

Adequate techniques for monitoring, measurements and diagnostics are crucial to obtain accurate and reliable experimental data in complex systems. Below are three papers presented that have demonstrated how to obtain experimental information from biomass particle flows, gas flows and soot-related species, respectively, in a configuration relevant to entrained flow gasification.

Wagner et al. [43] presented the design and operation of a research-scaled entrained flow reactor. In their experimental campaign, Norwegian spruce, Scots pine and Miscanthus were fed into the reactor. By employing non-intrusive (particle image velocimetry) and extractive (extraction probes and thermocouples) sampling techniques, it was proven their ability to provide the gas temperatures, particle velocities, residence times and morphologies. This builds a firm basis for further detailed experimental and modelling investigation of the gasification process.

In addition to particle information, details regarding the gaseous species are also needed. Ögren et al. [44] provided an online non-intrusive machine vision-based monitoring system (a monochromatic CCD camera sensor system), aiming to give reasonable estimation of equivalence ratio and syngas composition. The system was first validated using a McKenna flat flame burner and then later tested in a pilot-scale entrained flow gasifier of wood powder. Two simple image processing methods (reduction to statistical moments and pixel binning) were used. It was found that the reduction to statistical moments image processing method is more accurate. Two regress algorithms (Gaussian Process Regression and Artificial Neural Networks) were also examined. Although they were found to be similar given a large dataset, Gaussian Process Regression proved to perform better if only limited data was available. In conclusion, results show that the estimations could be executed based on a simple digital camera for flame monitoring and the system is a promising option to monitor gasifiers.

Besides gas flow and particle experimental data, it is also preferred to have insights into ash-related chemistry to address slag issues in the gasifiers. Qu et al. [45] used tunable diode laser absorption spectroscopy to simultaneous measure gas temperature, water vapor and atomic potassium in gas phase. The measurement method was first tested and validated for propane flame operation, 2D CFD simulation, thermocouples and Fourier transform infrared spectroscopy. It was later employed in a research-scale entrained flow gasifier where absolute concentrations of elemental potassium during biomass combustion was recorded. The system could be a useful tool to investigate ash related chemistry.

Slagging conditions are unwanted in real entrained flow systems as it reduces the efficiency over time. The above covers major methods to obtain important parameters of entrained flow gasification of biomass, in order to improve the operational aspects of such systems.

2.2.3 Char conversion model

When compared to drying and devolatilization, char conversion is slow and often the rate limiting step in the gasification process. This is especially relevant for entrained flow gasifiers where particle residence times are short [4][46]. The discussion that follows presents several researches on char conversion kinetics.

Gao et al. [23] used an intrinsic reaction rate sub-model and developed a comprehensive CFD Eulerian-Lagrangian model based on Ansys Fluent to simulate entrained flow gasification of biomass. In this model, the diffusion and kinetic rates for char reactions were established. Simulations using this model were compared with experiments. The maximum relative errors of lower heating value, gas production, cold gas efficiency and carbon conversion efficiency were found to be around 10 %. In terms of volumetric concentrations of CO, CO_2, H_2, CH_4 and C_2H_4, relative errors were found to be 1 – 18 %. Although the relative errors for CH_4 and C_2H_4 are large, their absolute errors are small. Therefore, the model was found suitable for simulations of entrained flow gasification.

Schulze et al. [47] paid special attention to intra-particle species transport in the char particle, as well as its changing size and density during the char conversion process, and developed an intrinsic-based sub-model for char conversion. The sub-model was validated based on experiments of thermogravimetric analysis. This intrinsic-based model was later used to simulate an endothermic reactor and the results were compared with simulations with a traditional surface-based model to show its importance in carbon conversion predictions.

Gao et al. [48] proposed later another gasification model. They conducted thermogravimetric analysis experiments so the intrinsic rates of birch wood char with CO_2 and O_2 were determined. Based on these obtained data, a model for biomass gasification was developed in the framework of Eulerian-Lagrangian CFD simulations. The model was applied to simulate a lab-scale air-blown entrained flow gasifier of sawdust. By comparing results between simulations and experiments, the relative errors of gas composition, gas heating value, gas production and carbon

conversion efficiency were found to be 1.94 – 19.79 %, 9.65 – 23.33 %, 1.17 – 5.95 % and 9.76 – 16.57 %, respectively. Based on this, the authors recommended this model to study biomass gasification.

The above presents several viable options for comprehensive char conversion models. In the selected papers, only simple char conversion models were applied to save computational cost. However, results indicate that more comprehensive char conversion models might be required to better mimic the realistic experimental conditions.

2.2.4 Performance

Performance studies are usually sensitivity analysis of different operating parameters (such as equivalence ratio, temperature, etc.) and aim to find an optimal operating condition in the studied range. Both experimental and simulation work have been done on this front, as stated below.

Dhanavath et al. [49] used a lab-scaled reactor to conduct entrained flow gasification of torrefied Karanja Press Seed Cake. An experimental matrix of various temperatures (600 – 1100 °C), equivalence ratios (0.1 – 1.0), steam to biomass ratios (0.1 – 1.0) and particle sizes (0.5 – 3.0 mm) was employed to study their effects on syngas composition, lower heating value, cold gas efficiency and carbon conversion. In the studied range, the optimal operational condition was found to be biomass of 0.5 mm at 1100 °C with equivalence ratio of 0.3 and steam to biomass ratio of 0.4. It was also found that as temperature increases, CO and H_2 increase in syngas while CH_4 and CO_2 decrease. The highest lower heating value of cold gas efficiency and carbon conversion were found to be approximately 12 $MJ \cdot Nm^{-3}$, 90% and 98%, respectively.

In the work of Ismail et al. [50], oil palm frond and Koompassia malaccensis were gasified with air in a research-scale entrained flow gasifier under atmosphere pressure at different temperatures (700 – 900 °C) and equivalence ratios (0.2 – 0.4). It was found that syngas production increased with increasing temperature, and optimal

equivalence ratio was 0.3 and 0.35 for oil palm frond and Koompassia malaccensis, respectively.

Weiland et al. [51] conducted experiments in a pilot-scale pressurized oxygen blown entrained flow gasifier with stem wood pellets produced from pine and spruce sawdust. Four operating parameters were varied for evaluation: O_2 stoichiometric ratio (0.244 – 0.497), gasification load (211 – 613 kW), gasification pressure (2 and 7 bar) and fuel size (125 – 180 μm). They found that the relative order of importance for these four operating parameters in a descending order were: O_2 stoichiometric ratio, gasification load, gasification pressure and fuel size. Carbon conversion was found to decrease dramatically if O_2 stoichiometric ratio was less than 0.3. CH_4 production in syngas was found to be highly dependent on temperature and a process temperature of 1400 °C was required if the desired CH_4 concentration in the syngas on a dry and N_2 free basis was less than 1 mol %.

Ku et al. [52] used Eulerian-Lagrangian CFD simulations and studied the effects of gasifying medium, reactor structure and feedstock properties. O_2, steam, CO_2 and a blend of CO_2 and steam were used as gasifying medium. Introduction of O_2 and CO_2 were found to benefit CO production and carbon conversion. In addition, steam-CO_2 gasification was found to perform better than pure steam or CO_2 gasification in terms of syngas production, carbon conversion and lower heating value. In terms of reactor structure, different injection nozzle sizes and positions were tested. It was found that the pyrolysis process could be accelerated by enlarging biomass inlet and combustible gas yields and conversion efficiency could be improved by having the inlet of biomass away from the axis of gasifier. Eight biomass species were selected to study the effects of their composition. A higher fraction of volatiles and fixed carbon and a lower fraction of moistures in the biomass composition were showed to lead to more production of combustible gas.

In summary, feedstock species and properties, operating temperatures and pressures, equivalence ratios, gasification mediums, reactor designs are varied to locate the optimal operating condition. Syngas composition, heating value, cold gas efficiency

and carbon conversions are often used as criteria to judge the performances of gasifiers. The above discussion provides important insights for further construction and operation of entrained flow gasifiers and valuable information for the FT-synthesis and value-chain analysis.

3 MODELLING THEORY AND METHODOLOGY

Chapter 2 reviews the relevant studies, in experiments as well as modelling, made by other researchers, this chapter presents the decision making process of modelling theory and methodology in the selected papers of this thesis and aims to answer the questions of what relevant options there are and why certain methods are chosen in the selected papers instead of others.

3.1 Reacting multi-phase flows

Entrained flow gasification is essentially reacting multi-phase flows. There are three phases that are commonly observed: gas phase, liquid phase and solid phase. Multi-phase flows mean that different phases are mixed together in the flows, for example, rain droplets (liquid phase) in the air (gas phase). When there are reactions involved, it is referred as reacting multi-phase flow. Many real-world phenomenon or processes are reacting multi-phase flows, so modelling of reacting multi-phase flow has a lot of applications.

In the framework of CFD, different approaches exist with the aim to accurately model reacting multi-phase flows, the most common approaches are Eulerian-Eulerian approach and Eulerian-Lagrangian approach: all phases are treated as continuums in the Eulerian-Eulerian approach, but the Eulerian-Lagrangian approach models the flow field as a continuum and particles are treated as discrete phase [53]. Despite its cheaper computational cost, the Eulerian-Eulerian approach cannot provide the discrete character and local information of biomass particles (such as velocity,

position, size, etc.) [53], which is within the scope of the thesis. For this reason, the Eulerian-Lagrangian method is chosen.

There are usually three kinds of coupling used in Eulerian-Lagrangian simulations [54]. The simplest one is one-way coupling where only the dispersed Lagrange phase is influenced by continual Euler phase, but not vice versa [54]. If both phases affect each other, it then becomes a two-way coupling [54]. When the interactions within dispersed phases have to be considered, it is referred as four way coupling [54].

The choice of the coupling method is dependent on the flow conditions of interest. Elgobashi [55] proposed a classification map of the coupling regimes for turbulent particle-laden flows. It uses two parameters, volume fractions of particles (φ) and ratio of particle response time for Stokes flow to Kolmogorov time scale (τ_p/τ_k), in order to determine which coupling method to employ. When Φ is less than 10^{-6} (dilute flows), it is within the regime of one-way coupling, where particles are influenced by turbulence but they are too dilute for their effects on the flow to be neglected [55]. For suspension flows ($10^{-6} < \varphi \leqslant 10^{-3}$), momentum exchange between particles and flow are significant enough to affect turbulence, and then two-way coupling is used [55]. When particle suspension becomes so dense ($10^{-3} < \varphi \leqslant 1$) that particle-particle interaction must be considered, four-way coupling is preferred [55]. It should be noted that the above approach oversimplifies the boundaries between the three coupling regimes. In fact, when τ_p/τ_k is more than 1, four-way coupling could also be chosen even when φ is less than 10^{-3}, and interested readers can refer to the original reference for detailed discussions [55]. Additionally, if φ is more than 1, it becomes a granular flow which is not discussed here [55].

For the simulations carried in this thesis, only one- and two-way coupling are used [56]. The decision is motivated by two factors. First, the flow conditions studied in the thesis are not that of dense suspension flows. Moreover, four-way coupling requires complicated and much more computational expensive particle-particle interaction models, which is considered to be an unnecessary level of detail given the objectives of the thesis.

3.2 Particle shape

The importance and effects of shape selection are previously discussed in Chapter 1.4 and will not be repeated here. But choosing a shape to represent biomass particle in simulations is a difficult task. In addition to the traditional spherical approach, various alternative attempts have been made. Bonefacic et al. [57] and Yin et al. [22] used cylindrical shapes to simulate biomass particles with coal in a co-firing setup, and Ren et al. [58] made corn-shaped assumptions, Ciesielski et al. [59] even went further and proposed a particle model with resolved microstructure. In theory, a simple shape, regardless of sphere, spheroid, cylinder, etc., is not perfect enough to fully represent the geometric characteristic of biomass particles due to their complex fibrous structures. It is even more difficult to do so under reactive conditions, where morphological changes and particle break-up occur. This requires extensive modelling efforts on a much smaller scale. It is computationally expensive for large scale simulations and goes beyond the scope of the thesis, which aims to find a better but still simple shape representation for biomass particles than current spherical shape assumption and then compare their differences in modelling.

Given that, the spheroid shape assumption is chosen in the selected papers. This is based on the work of Panahi et al. [28], who conducted combustion experiments of beechwood and miscanthus, in both raw and torrefied states, and found their shapes tend to be ellipsoidal or spheroidal upon devolatilization. In addition, particle spheroidization were reported for high temperature pyrolysis and char burnout [28][60]. Using a spheroidal shape assumption would make model development and implementation easier. With the shape being chosen, its quantitatively analysis of surface area are presented and discussed below.

In analytic geometry, an ellipsoid is defined as:

$$\frac{x^2}{a^2}+\frac{y^2}{b^2}+\frac{z^2}{c^2}=1, \tag{1}$$

where a, b and c are its three axes. When two of them are equal (for example, $a = b$), it is referred to as spheroids and its aspect ratio is defined as $\lambda = c/a$. If the aspect ratio is larger than one, it is referred to as a prolate spheroid. If the aspect ratio is less than one, it is referred to as an oblate spheroid. When the aspect ratio equals to one, it regresses to a sphere. In the context of this thesis, spheroid is used to refer to as prolate spheroid specifically unless stated otherwise.

One important aspect to consider is the particle surface area, as it is related to heat and mass transfer. Fig. 7 shows the surface area ratio of a spheroid to a sphere of equivalent volume at different aspect ratio of the spheroid. It can be seen that as the particle aspect ratio increase, the surface area ratio also increases with a slower and slower rate. This is expected to have major consequences in the initial drying and devolatilization stages where aspect ratios of biomass particles are large. However, one can also see from the figure that surface area of a spheroid is only around 30 % larger than a sphere of equivalent volume even when its aspect ratio is 4. This could mean that effects on particle thermochemical conversions due to surface area differences could be much less pronounced in the char conversion stage, where particle aspect ratio is lower [28].

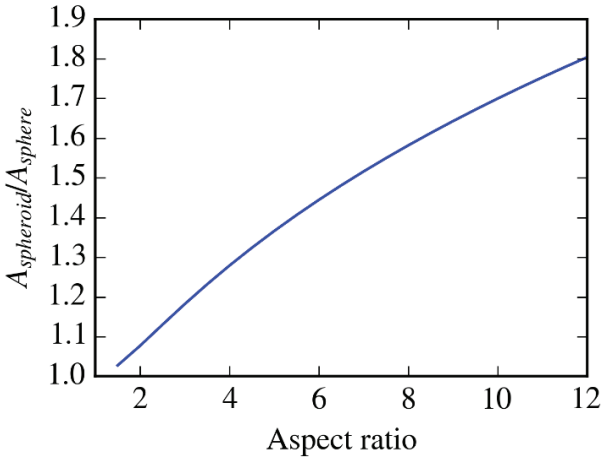

Fig. 7 Particle surface area (A) ratio of spheroid to sphere of equivalent volume at different particle aspect ratio.

3.3 Forces acting on particles

To simulate motions of pulverized biomass particles in a Lagrangian manner, it is important to properly model the forces acting on the particles. However, how to describe these forces remains open for debate. Stokes [61] took the first step and provided an analytical solution for a sphere in a uniform, steady flow at low particle Reynolds number. Then Basse, Boussinesq and Oseen independently worked on this topic and their results are summarized as the famous BBO (Basset–Boussinesq–Oseen) equation, where drag, added-mass and Basset-history forces are considered [62]. The applicable range of the BBO equation is limited to one (or a few) particle(s) in an uniform flow with particle Reynolds number less than 1, which, however, does not match the operating conditions of most applications (entrained flow gasifiers, in this case) [54]. Andersson et al. [54] provided a general frame work with expanded applicable range where the following forces are considered:

- Drag force;
- Pressure force due to pressure gradient;
- Virtual mass force;
- History force;
- Buoyance force;
- Lift force;
- Thermophoretic force;
- Brownian force;
- Force due to turbulence.

In entrained flow gasifiers of pulverized biomass particles, particle to fluid density ratio is high. As a result, one can arguably say that only drag, pressure gradient force and buoyance force are of significance, according to Anderson et al. [54]. However, in many CFD simulations of entrained flow gasifiers, only drag and buoyance forces are included. With the aim to offering comparison to the current common practices, only drag, buoyance forces (i.e. gravity) and sometimes profile lift (only when particle directionality is of interest, see the spheroid model in Chapter 3.3.1) are included in

the selected papers. With that being said, Chapter 3.3.1 and 3.3.2 present the theory on drag force and rocket force, respectively. Buoyance (gravity) force is not discussed here due to its simplicity.

3.3.1 Drag force

There are many models to describe drag forces. For modelling the thermochemical conversion process of pulverized biomass, the following three approaches are commonly used.

The first approach, hereafter referred as the sphere model, assumes all the pulverized biomass particles are spheres of equivalent volume. Its drag coefficient is expressed as [63]:

$$C_D = \begin{cases} 0.424\,\mathrm{Re}_p, \mathrm{Re}_p < 1000 \\ 24\left(1+\frac{1}{6}\mathrm{Re}_p^{\frac{2}{3}}\right), \mathrm{Re}_p \geq 1000 \end{cases}, \quad (2)$$

where C_D is the drag force coefficient and Re_p is the particle Reynolds number. This approach is offered in many CFD platforms and widely used, due to its simplicity [63]. The disadvantage is clear, as it cannot accurately represent particle shapes.

The second approach, hereafter referred as the simplified non-sphere model, introduces a simple overall shape factor to remedy the shape problem raised by the sphere model. The most common expression is based on the work of Haider and Levenspiel [64]:

$$C_D = \frac{24}{\mathrm{Re}_p}\left(1+B_1\cdot\mathrm{Re}_p^{B_2}\right)+\frac{\mathrm{Re}_p\cdot B_3}{\mathrm{Re}_p+B_4}, \quad (3)$$

where B_i (i = 1, 2, 3, 4) is a modeling coefficient calculated based on this particle sphericity. By its nature, the irregular shapes of pulverized biomass particles are considered to certain extent. However, two completely different shaped particles have

the same drag forces under this regime as long as they have the same shape factors. In addition, particle directionality is still overlooked in this model.

The third approach, hereafter referred to as the spheroid model, treats pulverized biomass particles as prolate spheroids, based on the work of Hölzer and Sommerfield [65]:

$$C_D = \frac{8}{\mathrm{Re}_p}\frac{1}{\sqrt{\phi_{\parallel}}} + \frac{16}{\mathrm{Re}_p}\frac{1}{\sqrt{\phi}} + \frac{3}{\sqrt{\mathrm{Re}_p}}\frac{1}{\phi^{\frac{3}{4}}} + 0.4240^{0.4(-\log\phi)^{0.2}}\frac{1}{\phi_{\perp}}, \qquad (4)$$

where ϕ, $\phi_{\parallel}$ and $\phi_{\perp}$ stand for sphericity, lengthwise sphericity and crosswise sphericity, respectively, and are used to characterize the particle's orientation. This was used in connection with particle torque model developed by Jeffery [66], where motions of an ellipsoidal particle in a viscous flow was examined. It should be pointed out that this approach has included the effects of "profile lift" (sideward motions due to particle axis incline relative to the main flow), which Mandø and Rosendahl [67] have implemented and discussed. This model is a simple point-based model with torque being one-way coupled, and is thus a simple first-step approach to study particle shape and rotational effects.

The above three drag force models are within the scope of the selected papers. It should be noted that other approaches of simulating drag forces for non-spherical particles are also available. For example, Zastawny [68] presented drag force formulas for ellipsoids, discs and fibers; Rosendahl [69] used three shape descriptors to model any non-spherical particles. Ullah et al. [70] conducted a review in CFD simulations of non-spherical biomass particles in Eulerian framework where common models for non-spherical particle drag coefficient are examined.

3.3.2 Rocket force

Entrained flow gasifiers operate at high temperate and short residence times, and pulverized biomass particles are subject to very high heating rates, moisture and volatiles are rapidly released via anisotropic microstructures of biomass particles. This

could create a jet-like force acting on particles. This is previously observed by Elfasakhany et al. [71] and repeatedly observed in our experiments. Elfasakhany et al. [71] referred to this force as rocket force and proposed a formula to model this force (minor modifications are made for easier implementation in this thesis):

$$F_{rocket} = S\frac{\left(\frac{d\left(m_{vol}+m_{mois}\right)}{dt}\right)^2}{A_{ca}\rho_g}, \tag{5}$$

where F_{rocket} is the rocket force [N], m_{vol} is the mass of released volatiles [kg], m_{mois} is the mass of released moisture [kg], t is the time [s], ρ_g is the gas density [kg·m^{-3}], A_{ca} is the maximum cross-sectional area that is perpendicular to the particle major axis [m^2], S is the efficiency factor representing the degree of anisotropy of particle and its value is uniformly random distributed between -1 and 1. As shown in Fig. 8, moisture and volatiles can only be released in the direction parallel to the particle's major axis in this model. If S is 1, all moisture and volatiles are released in one direction. If S is -1, it is the opposite direction. For an S value between -1 and 1, it means some are released in one direction while the rest are in the opposite direction.

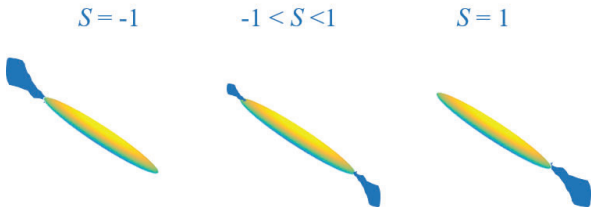

Fig. 8 Illustration on particle moisture and volatile release.
S is the efficiency factor. The spheroids represent biomass particles and their colors, which have no physical meaning, are used to indicate that their orientations are the same. The blue colored clouds are released moisture and volatiles.

This equation builds the basis for modelling such phenomena, but one should also notice it comes with several assumptions and limitations. First, it is, by its definition, directly coupled with the release rate of moisture and volatiles, which means that the

precision of this rocket force model can be greatly and directly influenced by the models for drying and devolatilization. Moreover, this model assumes that moisture and volatiles are only released along the particle longitude direction. Even though this modelling assumption corresponds to the work of Brackmann et al. [72], where they conducted optical measurements of volatile gases from single wood particles under high heating rates and found that volatiles were mainly released along the fiber, this model still cannot present a full picture. Furthermore, the efficiency factor S in the current rocket force model is subject to challenges. The current model assumes that S uniformly varies between -1 and 1, which lacks support from experiments and imposes a potential systematic error in the model.

Despite its shortcomings, this model is still used in the present work to study the phenomenon as a first step, since research on this topic is rarely found. In the selected papers, the rocket force is not considered. However, simulations with this effect included have been done, and the results are reported later in Chapter 5.4 and planned for further journal publications.

3.4 Convective heat transfer

In this chapter, several convective heat transfer models, based on particle shapes, are presented and compared.

Particle convective heat transfer is governed by

$$\dot{Q} = hA_s\left(T_s - T_p\right), \tag{6}$$

where $\dot{Q}$ is the heat that a particle absorbs [W], A_s is the particle surface area [m^3], T_s and T_p are the surrounding and particle temperature [K], respectively, h is the heat transfer coefficient [$W \cdot m^{-2} \cdot K^{-1}$] and is calculated as:

$$h = \frac{\kappa_f \cdot Nu}{d_p}, \tag{7}$$

where κ_f is the fluid thermal conductivity [$W \cdot m^{-1} \cdot K^{-1}$], d_p is the particle diameter [m] and Nu is the particle Nusselt number. Many particle heat transfer models are usually based on modelling the particle Nusselt number and are shortly introduced below.

The most common model is the Ranz-Marshall model [73][74]. It is expressed as:

$$Nu = 2 + 0.6\,\mathrm{Re}^{\frac{1}{2}}\,\mathrm{Pr}^{\frac{1}{3}}, \tag{8}$$

where Re is the particle Reynolds number, and Pr is the particle Prandtl number. Hughmark [75] further expand the range of the Ranz-Marshall model [73][74] and proposed the Nusselt number correlations for rigid spheres. The model is hereafter referred as the Hughmark model and its correlations are listed as below:

$$Nu = \begin{cases} 2 + 0.6\,\mathrm{Re}^{\frac{1}{2}}\,\mathrm{Pr}^{\frac{1}{3}}, 1 < \mathrm{Re} < 450, \mathrm{Pr} < 250 \\ 2 + 0.5\,\mathrm{Re}^{\frac{1}{2}}\,\mathrm{Pr}^{0.42}, 1 < \mathrm{Re} < 17, \mathrm{Pr} > 250 \\ 2 + 0.4\,\mathrm{Re}^{\frac{1}{2}}\,\mathrm{Pr}^{0.42}, 17 < \mathrm{Re} < 450, \mathrm{Pr} > 250 \\ 2 + 0.27\,\mathrm{Re}^{0.62}\,\mathrm{Pr}^{\frac{1}{3}}, 450 < \mathrm{Re} < 10000, \mathrm{Pr} > 250 \end{cases}, \tag{9}$$

It can be seen that the Ranz-Marshall model falls into the regime of the Hughmark model. These two models are usually implemented in common CFD platforms. Besides, other relationships for spheres can be found in the work of Whitaker [76].

These models presented above are all based on the assumption that particles are spherical. Thus, their applicability to non-spherical particles are subject to be challenged. To remedy this, several models are proposed based on different particle shape assumptions and are presented as follows. Whitaker [76] proposed correlations for cylinders and plates based on collected experimental data. Sparrow et al. [77] reviewed and summarized average Nusselt numbers for non-circular and circular cylinders in cross flow. Richter and Nikrityuk [78] developed heat transfer coefficients for non-spherical particles, based on cuboidal and ellipsoidal particles orientated in a stream-wise direction in cross flow at sub-critical Reynolds number

and the Nusselt number in their work is dependent on particle sphericity and crosswise sphericity. Furthermore, they tried to expand the applicable range to particles with arbitrary orientation and derived a model where the Nusselt number is dependent on the particle's angle of attack [79], which can be coupled to particle drag, lift and torque. Besides, Ke et al. [80] also investigated particles of different aspect ratios and incident angles at different Reynolds number from 10 to 200 and improved formulations of average Nusselt number. In addition to conventional fluid systems, attempts are also made by Zhang and co-authors to establish heat transfer coefficients for non-spherical particles in supercritical water [81][82][83].

In this thesis, the work of Kishore and Gu [84] is chosen due to the fact that it is specifically developed for spheroids and easy to be implemented in the OpenFOAM platforms. They conducted numerical investigation and proposed a heat transfer coefficient for spheroidal particles at intermediate Reynolds and Prandtl numbers:

$$Nu = 2\lambda^{0.3} + \mathrm{Pr}^{0.4}\left(0.4\,\mathrm{Re}^{0.5}\,\lambda^{0.83} + 0.06\,\mathrm{Re}^{\frac{2}{3}}\,\lambda^{0.1}\right) \tag{10}$$

where λ is particle aspect ratio, defined as the ratio of particle major axis to minor axis. This model is hereafter referred as the Kishore-Gu model. Gerhardter et al. [85][86] used this model to simulate slag particles dropping through hot air in combusting flows, and the simulation results correspond well with experiment. However, the applicable range of this model is limited to: $1 \leq Re \leq 200$, $0.25 \leq \lambda \leq 2.5$ and $1 \leq Pr \leq 1000$ [84].

The operating conditions of an entrained flow gasifier of pulverized biomass do not necessarily fall into the applicable range of the Kishore-Gu model. Particle Reynolds number is dependent on slip velocity, particle size and the viscosity of the surrounding gas. Particle aspect ratios are dependent on pre-treatment processes of raw materials and can have a very wide range. In the selected papers, they vary from 1.8 to 10. For coal particles, it has been reported that most coal particles have Reynolds number less than 10 even though it could reach to 100, biomass particles are expected to have larger Reynolds numbers due to their larger size [87]. The Prandtl number, on the

other hand, is estimated to have a narrow range. Simonsson et al. [88] conducted experiments in a pilot scale entrained flow gasifier of wood powder or peat powder with a jet or swirl burner at different air-fuel equivalence ratios, ranging from 0.3 to 0.8, and average temperature inside the gasifier were measured to be 950 – 1200 °C based on several thermocouple readings. The Prandtl number for air at 20 – 1600 °C is 0.69 – 0.75. Therefore, it is reasonable to assume that the Prandtl number in the entrained flow gasifier is close to this narrow range as well. Given the above, comparisons between the Ranz-Marshall and Kishore-Gu model are presented below within the aforementioned reasonable ranges for Reynolds number, particle aspect ratio and Prandtl number that are realistic for entrained flow gasification of pulverized biomass particles.

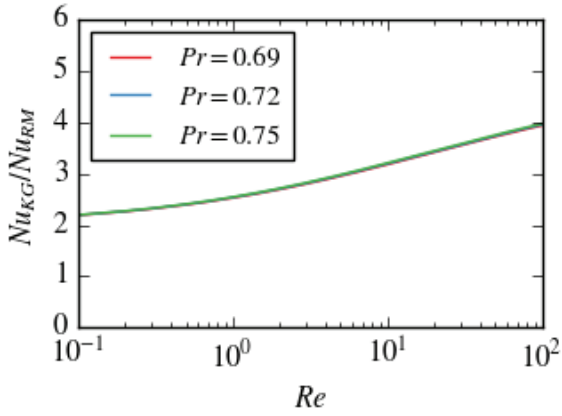

Fig. 9 Nusselt number, *Nu*, ratio predicted by two heat transfer models at different Prandtl number, *Pr*, and Reynolds number, *Re*.
Subscript KG and RM represent the Kishore-Gu and Ranz-Marshall model, respectively. Particle aspect ratio is 10.

Fig. 9 presents the Nusselt number ratio of the Kishore-Gu model to the Ranz-Marshall at different Prandtl numbers and Reynolds numbers when particle aspect ratio is configured to 10. As the Reynolds number increases, the Nusselt number increases as well, which means that the particle has better heat transfer when using

the Kishore-Gu model than the Ranz-Marshall model. By comparing plots at different Prandtl numbers, one can see that there are no significant differences among them. Similar trends are also observed if one changes particle aspect ratio to 0.1, 0.25, 1 or 2.5, although they are not plotted here.

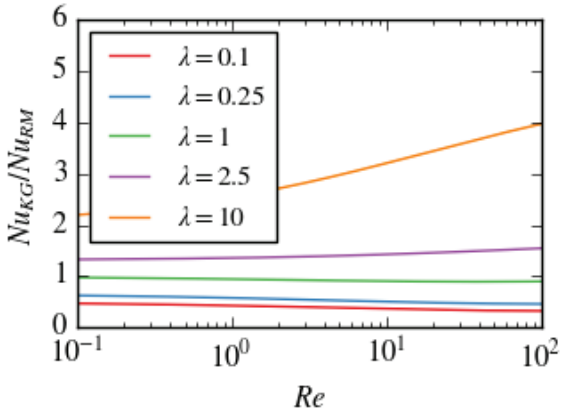

Fig. 10 Nusselt number, *Nu*, ratio predicted by two heat transfer models at different particle aspect ratio, λ, and Reynolds number, *Re*.
Subscript KG and RM represent the Kishore-Gu and Ranz-Marshall model, respectively. Prandtl number is 0.74.

Fig. 10 provides the Nusselt number ratio of the Kishore-Gu model to the Ranz-Marshall model at different particle aspect ratios and Reynolds numbers when Prandtl number is configured to 0.74. This value is chosen based on the Prandtl number for air at 1000 – 1600 °C and 1 bar. It should be representative for all cases with Prandtl number ranging from 0.69 to 0.75, based on the findings from Fig. 9. The general trend one can see from Fig. 10 is that the Nusselt number ratio increases as particle aspect ratio increases. Their dependency on Reynolds number, however, is different. When the particle aspect ratio is 1, the Nusselt number ratio remains closely at 1 regardless of Reynolds number. This indicates that the Kishore-Gu model arguably regresses to the Ranz-Marshall number when particles are spherical. When the particle aspect ratio is more than 1, the Nusselt number ratio, which is always above 1,

increases as the Reynolds number increases. It means that at higher Reynolds number the Kishore-Gu model favors particle heat transfer more than the Ranz-Marshall model, if particles are more elongated. However, this is not the case for particles with aspect ratios less than 1. In this regime, the Nusselt number ratio, which is now always below 1, decreases as the Reynolds number increases. This means for oblate particles, the Ranz-Marshall model yields to higher Nusselt number than the Kishore-Gu model, especially at higher Reynolds number.

To summarize, the Ranz-Marshall model and the Kishore-Gu model are expected to predict different simulation results for particles that deviate from being spherical. In the context of this thesis, the particle aspect ratio is always assumed to be more than 1, and as a result, the Nusselt number predicted by the Kishore-Gu model is expected to be larger than the ones by the Ranz-Marshall model, meaning that the heat transfer is enhanced when employing the Kishore-Gu model with spheroidal particle shape assumptions. Due to the lack of other alternatives of heat transfer models, specifically for spheroids, the Kishore-Gu model is chosen here in this thesis, even though its applicable range is limited.

3.5 Devolatilization

As previously mentioned, biomass contains comparably more volatiles than coal [20]. Therefore, extensive efforts have been made to investigate the devolatilization process of biomass, both in experiments and simulations.

Experimental investigations can generally be divided into two categories. The first one is via TGA (thermal gravimetric analysis). TGA experiments are often conducted in well-controlled environments, where a very small amount of samples are placed in a pan and heated up in a predetermined manner while their mass loss is measured [26]. However, Mehrabian et al. [89] found that kinetic parameters obtained based on conventional TGA experiments were not applicable under fast heating rate conditions. To remedy this, other reactors such as DTRs (drop tube reactor) or EFRs (entrained flow reactor) are also used in the experimental studies of biomass devolatilization

[25][90]. However, the particle residence time, particle temperature and particle mass loss are difficult to be accurately measured in these reactors [26][91].

The above difficulties in experiments makes model development challenging, as they are restricted to experimental conditions they derivate from [92]. Nevertheless, recent progress in devolatilization or pyrolysis models are reviewed and summarized by Di Blasi [33] and Haberle et al. [19]. Based on their surveys, these models can generally be classified into the following categories: single-component schemes, multi-component schemes and other schemes.

Single-component means that biomass as a whole is treated as a homogeneous single reactant. There are two common approaches. The first one is the one-step global approach as below [19]:

$$\text{dry biomass} \rightarrow \text{char} + \text{gases} \,. \tag{11}$$

This is a straight forward and simple model which is easy to implement, but stoichiometric coefficients of each species (tar, CO, etc.) within the gases are unknown and requires pre-definition, by experimental data or other modelling methods [19]. To remedy this, some treat the production of char, tar and permanent gases as three independent competing reactions as follows [19]:

$$\text{dry biomass} \begin{cases} \xrightarrow{\text{Reaction 1}} \text{char} \\ \xrightarrow{\text{Reaction 2}} \text{tar} \\ \xrightarrow{\text{Reaction 3}} \text{permanent gases} \end{cases} . \tag{12}$$

One can see that the constraint among the products of the three competing reactions are that the summed mass of products should be equal to the mass of reactants [19].

Instead of assuming that biomass is a homogeneous single reactant, the multi-component scheme treats biomass as heterogeneous, and should be considered as a combination of many homogeneous components, which reacts in parallel [19]. For example, biomass devolatilization could be modelled as three independent parallel devolatilization processes of lignin, cellulose and hemicellulose as shown below [93]:

$$\text{dry biomass} \rightarrow \begin{cases} \text{lignin} \xrightarrow{\text{Reaction 1}} \text{products} \\ \text{cellulose} \xrightarrow{\text{Reaction 2}} \text{products} \\ \text{hemicellulose} \xrightarrow{\text{Reaction 3}} \text{products} \end{cases} . \quad (13)$$

This approach assumes that these multi-components would decompose exactly the same way in biomass particles as they would decompose in their pure forms separately, but postulates no interaction among these multi-components, which could be problematic as experimental evidences has stated otherwise [94][19].

Besides the above, there are also other alternative schemes, such as Broido–Shafizadeh scheme [95], Ranzi scheme [96], etc. Haberle et al. [19] has summarized and tabulated some less used schemes for interested readers.

In the context of this thesis, the model should be suitable for entrained flow gasification conditions, which means it should be applicable to conditions of high temperature, high heating rates and short residence times. In addition, the focus of the thesis is to assess how particle shapes effects particle hydrodynamics and, in turn, thermochemical conversion histories. It does not aim to examine the complex chemical kinetics of entrained flow gasification process. Therefore, a simple model is the better option. As a result, the modelling parameters employed by Johansen et al. [91] is chosen. Their research provided a new set of kinetic parameters of a one-step global Arrhenius equation under the aforementioned operating conditions (temperature: 1405 – 1667 K; heating rate: in the order of 10^5 K·s; residence time: less than 0.1 s):

$$\frac{dm_{devol}}{dt} = -Ae^{-\frac{E}{RT_p}} m_{devol}, \quad (14)$$

where m_{devol} is the mass of the remaining volatiles in the particle [kg], t is the time [s], A is the pre-exponential constant (18.9×103 s^{-1}), E is the activation energy (2.1305×107 J·$kmol^{-1}$), R is the universal gas constant [J·K^{-1}·$kmol^{-1}$], and T_p is the particle temperature [K].

3.6 Gasification

Gasification is a complicated process and various modelling approaches are available. The kinetic rate model and the thermodynamic equilibrium model are the most frequently applied options.

The thermodynamic equilibrium model predicts the products and their compositions based on the assumption that thermochemical equilibrium in the reactor is achieved, i.e. reactants and products are perfectly mixed for an infinite period of time [97]. It can be further categorized into stoichiometric models and non-stoichiometric models [97]. Given its nature, it is simple to implement and independent of the design of the reactor. However, it is not suitable for operating conditions where its modelling assumptions are unrealistic, such as, when there is imperfect mixing on local or global level, or when the residence times are relatively short in reference to long reaction times.

The kinetic rate model is based on chemical reaction kinetics. It overcomes the aforementioned disadvantages of the thermodynamic equilibrium model, but it is computationally more expensive. In addition, one needs to pay special attention to the applicability ranges of the kinetic data, which are usually derived from experiments performed under certain conditions and its validity outside these conditions is questionable.

Other modelling approaches, such as the Aspen Plus model or the artificial neural network models, are also of interest. Baruah and Baruah [97] and Puig-Arnavat et al. [10] have reviewed, summarized and tabulated various approaches and represent excellent references for further details.

The current work focuses on developing simulation tools for entrained flow gasifiers, which feature short residence times. This implies that a kinetic model with a simplified global reaction mechanism is a good choice and the model used by Ku et al. [98] is therefore selected.

4 EXPERIMENTAL ASPECTS

Experiments in this thesis serves two purposes: one is to provide experimental data for model validation, the other is to provide realistic operating conditions for simulations in order to make predictions that are relevant in real world applications. Therefore, a lab-scale laminar flat flame drop tube reactor and a pilot lab-scale entrained flow gasifier were employed to achieve the two objectives and are described below, respectively.

4.1 Lab-scale laminar flat flame drop tube reactor

Entrained flow gasification is a process where multiple particles react under high heating rate and high operating temperature with short residence time. Experimental data of similar conditions for gas flow can be easily found and many CFD simulations work were validated based on these. However, experimental data for particles, such as velocity, trajectory, orientation, morphological development, under similar conditions are rarely reported, to the best knowledge of the author. Therefore, the lab-scale laminar flat flame drop tube reactor located in Luleå University of Technology (Fig. 11) was used here to conduct such experiments to fulfill the knowledge gap and provide foundations for particle model validation in this thesis. The reactor consists of gas and biomass feeders, a porous flat flame burner, a reactor body and four optically accessible windows. Detailed geometric and operating information of this reactor can be found in Paper 2 and 3 and are not repeated here.

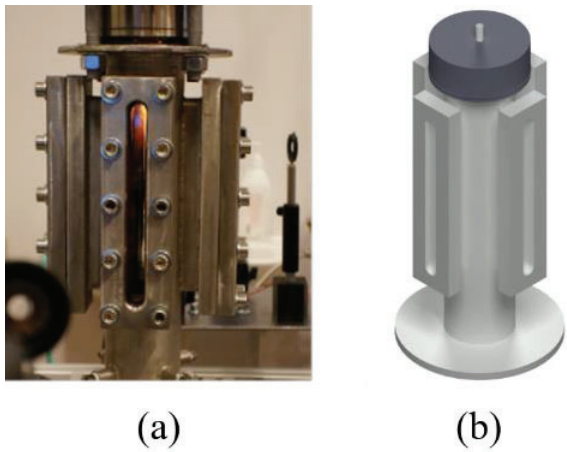

Fig. 11 Lab-scale laminar flat flame drop tube reactor.
(a) real photograph; (b) illustration.
(Re-formatted from Fig. 1 of Paper 3.)

4.1.1 Fuel pre-treatment

Norwegian spruce was used in the experiments to produce pulverized biomass particles. They were obtained using a large-scale hammer mill at the Biomass Technology Center (Biomassateknologicentrum, Umeå, Sweden) and then sieved to 200 – 250 μm size range. Based on their particle aspect ratio, these particles were manually separated into two groups: one equant (low aspect ratio) and the other elongated (high aspect ratio). These particles were later dried in an oven and then stored in a drying cabinet. Before injecting them into the drop tube reactor, their morphological information, such as size and aspect ratio, were measured by Camsizer (Retsch Technology GmbH).

4.1.2 Reactor schematic and experiment procedures

Fig. 12 shows the simulation geometry of the reactor. There are three feeders or inlets (*Inlet A*, *B* and *F*) for gas and biomass injections. The first one (*Inlet A*) supplied N_2 and was turned on first to provide an inert environment. The middle one (*Inlet B*) injected a mixture of CH_4, CO_2 and O_2 into the porous laminar flat flame burner. It

remained at room temperature under non-reactive experiments, or gases flowing through it was ignited under reactive experiments to create a premixed laminar flame. The last one (*Inlet F*) injected particle carrier gas CO_2, with or without particles. There were two kinds of particles involved. The first one was the aforementioned pre-treated biomass particles. The second one was TiO_2, which acted as tracer particles for measuring the gas flow fields. In this inlet, the flow rate of carrier gas could be adjusted. As a result, the amount of particles carried could be changed accordingly.

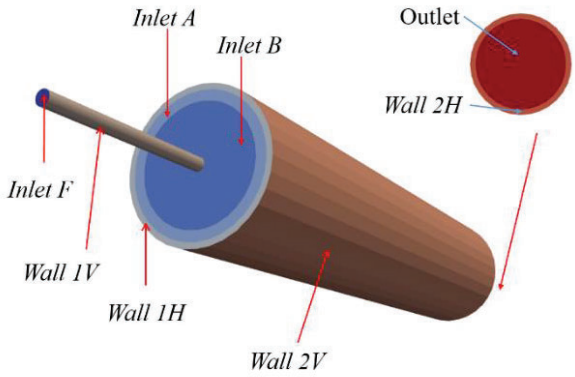

Fig. 12 Simulation geometry of the flat flame drop tube reactor.
(Re-formatted from Fig. 2 of Paper 3.)

After injecting particles and waiting for the system to reach a steady state, a pulsed laser sheet (Dual power 527nm Litron, NdYAG laser) was shone through the optical accessible windows in the reactor walls and high-speed cameras (SpeedSense VEO 410 from Dantec Dynamics) were used to take images from the laser plane.

In this experimental campaign, a series of experiments were conducted by varying the following parameters.

i. Non-reactive or reactive.

In the reactive experiments, the reactor wall was preheated, and a premixed laminar flame was ignited at the flat flame burner. Such

actions were not taken in the non-reactive experiments. The primary reason to conduct non-reactive experiments were to assess systematic errors of the reactor without the influences of reactions, and to provide enough data to better optimize the configurations in non-reactive simulations so that it would be easier to setup reactive simulations.

ii. Flow rate of particle carrier gas CO_2.

As mentioned previously, the flow rate of particle carrier gas could be adjusted. Two groups of experiments were conducted based on this, one with low carrier gas flow (0.14 $l \cdot min^{-1}$) and the other with high carrier gas flow (0.27 $l \cdot min^{-1}$). This was designed to address the effects of carrier gas flow on biomass devolatilization.

iii. With or without biomass particles.

a. If no biomass particles were injected, TiO_2 particles were injected as tracer particles to obtain velocimetry information of the gas flow fields without influences of biomass particles.

b. If biomass particles were injected, two cases were tested: with and without TiO_2. This originally was planned to obtain velocimetry information of the gas flow under the presences of biomass particles. However, it is uncertain how biomass particles, tracer particles and gas flow fields would influence each other, especially under reactive conditions. Therefore, experiments were conducted both with and without tracer particles, as an efficient effort to obtain more data on each condition.

iv. Particle aspect ratio.

As previously mentioned, two groups of particles were used based on particle aspect ratio, one equant and the other elongated. This was designed to study the effects of different aspect ratios on biomass thermochemical conversion histories.

Each set of experiments listed above were conducted three times so its repeatability could be assured. At first glance, it might seem that there were too many experiments executed just to validate the implemented particle models under reactive conditions. However, the experimental campaign was designed to fulfill several objectives and the work presented in this thesis was only one of them.

4.1.3 Post-processing

In the experiments, particles were optically captured by the laser plane and photographed by the two high speed cameras. These images were post-processed by Dantec Studios with an in-house Matlab codes after the experiments. Then particle velocity, size and other properties were obtained based on time, particle position, and morphological information captured by the images. The post-processing details are summarized in Paper 2 and Paper 3, and results are used for model validation.

4.2 Pilot lab-scale entrained flow gasifier

The setup described above is small scaled and particle loading is relatively low. It is arguably an efficient setup for model validation under reactive conditions. With validated models, a reasonable next step is to employ them to make predictions in a larger scaled system with more realistic operating conditions. The pilot lab-scale entrained flow gasifier from Simonsson et al. [88] was selected for this purpose. The gasifier is cylindrically shaped with a flat top and conical end. It is 3.9 m high with an inner diameter of 0.5 m and could be operated with a swirl burner or a jet burner [88]. The fuel was supplied at 20.2 $kg \cdot h^{-1}$ for wood powder or 22.9 $kg \cdot h^{-1}$ for peat powder [88]. With two choices for fuels and two options for burners, gasification experiments were conducted at 5 different air-fuel equivalence ratios, ranging from 0.3, 0.4, 0.5, 0.6 and 0.7 [88].

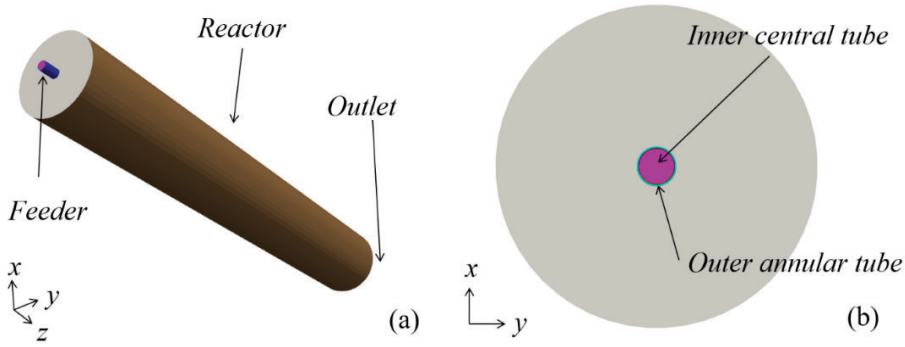

Fig. 13 Simulation geometry based on experiments from Simonsson et al. [88].
(a) 3D illustration; (b) projection in xy-plane.
(Re-formatted from Fig. 8 of Paper 3.)

In the simulations, the gasifier is simplified as shown in Fig. 13. Biomass particles with primary air are injected via the inner central tube. Secondary air is injected via the outer annular tube. The main reason for choosing the above experiments was due to the fact that it could provide a comprehensive overview of realistic operating conditions for entrained flow gasification of pulverized biomass particles, and one of the operating conditions was indeed used in non-reactive simulations in Paper 1 and reactive simulations in Paper 3. However, other aspects of the experiments were of less interest for the current work. Also, the experiments were not conducted by the author. For these reasons, the detailed experimental plan is not summarized here and interested readers are kindly referred to the original reference [88].

5 RESULTS

This chapter presents the results of the Ph.D. work and is organized into four parts: the first three parts summarize the findings that is presented in more detail in the three attached journal publications, whereas the last part discusses the effects of rapid release of volatiles during thermal conversion of biomass, which is currently unpublished work.

5.1 Paper 1: Eulerian-Lagrangian simulation of pulverized biomass jet using spheroidal particle approximation

In this paper, a spheroidal shape assumption was employed to better represent pulverized biomass particles and compared to that of spherical ones in simulations of particle flows. As a result, drag and torque models for spheroids were implemented into OpenFOAM, an open source CFD platform. The drag and torque models were then verified and validated based on experiments and DNS (direct numerical simulation) under non-reactive conditions. With the validated model combinations, non-reactive CFD simulations were conducted in a configuration similar to entrained flow gasification of pulverized biomass particles. In these simulations, three particle shape approaches were used. The first one is the traditional spherical approach, referred to as the sphere model. The second one is the less commonly practiced approach, where an overall shape factor is used to characterize the shape irregularities of biomass particles, referred to as the simplified non-sphere model. The third approach is the current spheroidal approach. Particle velocity, residence time and local concentration predicted by these three different models were quantitatively compared

and examined. Differences in particle axial velocity were observed and the spheroid model was found to predict a more divergent distribution than the other two models. Similar trends could also be found in terms of particle residence time and local concentration.

5.2 Paper 2: Morphology and volume fraction of biomass particles with different aspect ratio in a jet flow during devolatilization

The spheroidal particle model in Paper 1 were only used under non-reactive conditions. It should be further validated under reacting, high temperature and fast heating conditions. For this purpose, this paper conducted a series of experiments in a laminar flow flat flame drop tube reactor to build basis for future model validation. Accompanied by carrier gases of different flow rates, pre-treated particles of Norwegian spruces with different aspect ratios were injected into the reactor where they were gasified in the surrounding gases, then subjected to a laser plane by which images were captured by high speed cameras. After post-processing, particle velocity, size, shape and volume were obtained, which could later be used for model validations. The observed delayed onset of dispersed soot incandescent matter was believed to be caused by high flow rates of carrier gas and high particle volume fractions, which affects heating rate and conversion history of particles. Morphological changes were evidenced to occur in a heterogeneous manner and affected by particle heating rate, particle aspect ratio and carrier gas flow rate. Radial migration and rapid deceleration were also seen and believed to be caused by the fast release of volatiles from the biomass particles, but this hypothesis needs further examination. All the above builds the basis and provides adequate experimental data for reactive simulations conducted in Paper 3, as well as the discussion on rapid release of volatiles in Chapter 5.4.

5.3 Paper 3: Computational fluid dynamic simulations of pulverized biomass conversion using spheroidal approximation

Since simulations in Paper 1 were based on non-reactive conditions, this paper takes the next step to employ simulations of reactive conditions, similar to the experiments reported in Paper 2. In addition to the simulation setup in Paper 1, the work in this paper also adopted a set of parameters for devolatilization and a heat transfer model for spheroids. With the combination of the aforementioned sub-models, CFD simulation were conducted for the experiments of biomass particles injecting in the laminar flat flame drop tube reactor described in Paper 2. By comparing modelling and experimental results, it was found that particle alignment angles tend to be 0° in the experiment, but this trend was not reflected in the simulations, due to differences in velocity gradient in gas flow. In addition, the model combination was arguably validated under high temperature, fast heating and reactive conditions based on results of particle axial velocity. Built on this, further CFD simulations, with different drag and heat transfer models were conducted in a configuration similar to an entrained flow gasifier (see Paper 1 and Chapter 4.2). Particle orientation was repeatedly found to be dependent on velocity gradient of the gas flow under reactive conditions. Simulation results also showed that the combination of the hydrodynamic and the heat transfer model for spheroids favors the heat and mass transfer of particles, which is very relevant for rapid processes like drying and devolatilization. However, particle conversions and syngas productions are also determined by slower char conversions and particle residence times. The sphere and simplified non-sphere models predict 61% and 43% longer residence times than the ones with spheroidal models. As a result, different models predicted different syngas productions right after injection of biomass where drying and devolatilization are expected to be dominant, but such differences were not observed at the outlet of the reactor.

5.4 Effects due to rapid release of volatiles

In the selected papers, the rocket force model (described in Chapter 3.3.2) was not included. This chapter presents the effects of the rocket force model on simulations and compares the results with experimental data. As the chapter title indicates, only the release of volatiles is included, excluding moisture. This is because only dried biomass particles were used in the experiments. It should be noted that the below are unpublished preliminary results and planned for future journal publications.

The employed post-processing method could obtain the exact position of a given particle in each time frame or snap. Based on time and position information, particle velocity and trajectory could be calculated. Fig. 14 presents the particle trajectories in the experiments of the laminar flat flame drop tube reactor, each colored line represents a trajectory of one single particle. One can observe that the majority of the biomass particles fall down vertically with small radial displacements. This is expected as the gas flow direction and gravity are both aligned in vertical direction. The slight radial displacements of most particles in the mainstream are very likely to be caused by the fact that the biomass feeder is not completely perpendicular to the ground, due to thermal expansion and manufacture factors. However, it is obvious that a small number of particles exhibit larger than average radial displacements. It is postulated here that from these particles, a significant amount of volatiles were released in radial direction in a short period of time, making particles move radially according to jet like force.

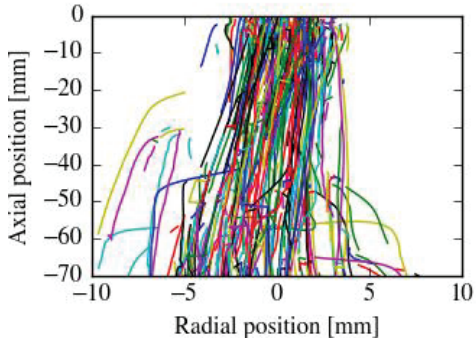

Fig. 14 Particle trajectories in the experiments.
Each colored line represents the trajectory of one single biomass particle in the experiment. It should be noted that different plotting scales are applied in *x*- and *y*-axis to make the particle radial displacement more visually obvious.

The phenomenon is also visualized in Fig. 15, which shows the particle absolute velocity at different axial positions (i.e. distances from burner outlet). Due to effects of gravity and drag force, one can see from Fig. 15(a) that most of particles first accelerate, then deaccelerate or reach a plateau in a gradual manner. However, it is also evident that some particles exhibit a very sudden manner of acceleration, and then deceleration. This indicates that there is a force that suddenly acts on the particle, which then suddenly disappears. It is in line with fact that volatile release from biomass particles is a rapid process under high heating rates.

One can also see a clear categorization based on velocity trend around axial position of -40 mm. It becomes more obvious in Fig. 15(b), where the same data is plotted in a scatter plot. To further investigate the reasons behind this, a filter is needed to separate these two. Here, the following filtering procedures are employed.

- Only particles that travelled to -40 mm or further down are considered. This is because the categorization is clearly observed at axial position between -40 and -70 mm.

- For the above selected particles, they are separated into two bands: the upper band and the lower band. The red solid line in Fig. 15(b) serves as the threshold line for this purpose. It starts at (-40 mm, 0.7 m/s) and ends at (-70 mm, 0.5m/s), which is arbitrary determined based on the visual observation.
    - The upper band. If the absolute velocity of a particle is always above the threshold at axial position between -40 and -70 mm, the particle is classified into the upper band.
    - The lower band. If a particle is not selected into the upper band, it is classified into the lower band.

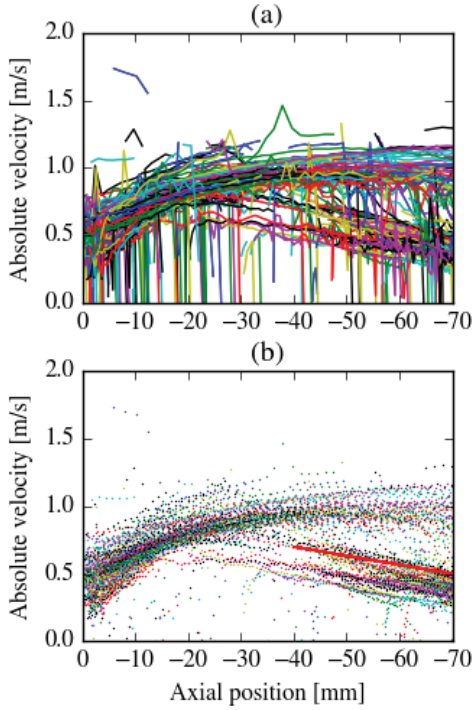

Fig. 15 Particle absolute velocity at different axial position.
(a) is the line plot, each colored line represents the trajectory of one single biomass particle in the experiment. (b) uses the same data but plots them in a scatter plot to make the velocity categorization easier to obverse, the red solid line is the threshold line for later separation.

It is confirmed that the above filtering method is repeatable. Table 2 shows the percentage of particles in the lower band out of all sampled particles in three experimental repetitions. Statistically, around 24.09 % of sampled particles are in the lower band. The differences among the three repetitions are acceptable within the 1.53% margin of error. For this reason, all figures in this chapter are plotted based on data from Experiment Repetition #2 unless stated otherwise, which is closest to the average value in Table 2, to avoid unnecessary repetition.

Table 2 Percentage of particles in the lower band out of all particles within axial positions between -40 and 70 mm.

Experiment repetition	#1	#2	#3	Average
Particles in the lower band	26.81%	23.78%	21.61%	24.09 ± 1.53%

The aforementioned filtering method also prove to be able to separate particles into two bands as intended, based on subplots (b) and (c) from Fig. 16, where the results after using the above filtering method are presented. According to subplots (a), particles in the lower band are more widely distributed in the radial direction than particles in the upper band. This helps to explain why particle velocity is lower in the lower band. The gas flow velocity is expected to be lower in outer radial regions than in the regions that are close to the reactor centerline, making drag forces acting on particles in the outer radial region larger, thus slowing down particle velocities. The observed distribution in particle radial position is likely to be caused by the rocket force. One can see that there are more particles having sudden radial displacements in the lower band than in the upper band, meaning more particles having sudden release of volatiles in the radial directions in the lower band. This is further confirmed by the curves in subplots (b), where sudden peaks of absolute velocity can be clearly seen in the lower band, whereas the particle absolute velocity developments over the reactor axial position are much smoother in the upper band. It should be further stressed that the observed peaks also mean the rocket forces along the axial direction, in addition

to the radial direction, may also play a role since it is absolute velocity plotted here, not only axial or radial velocity.

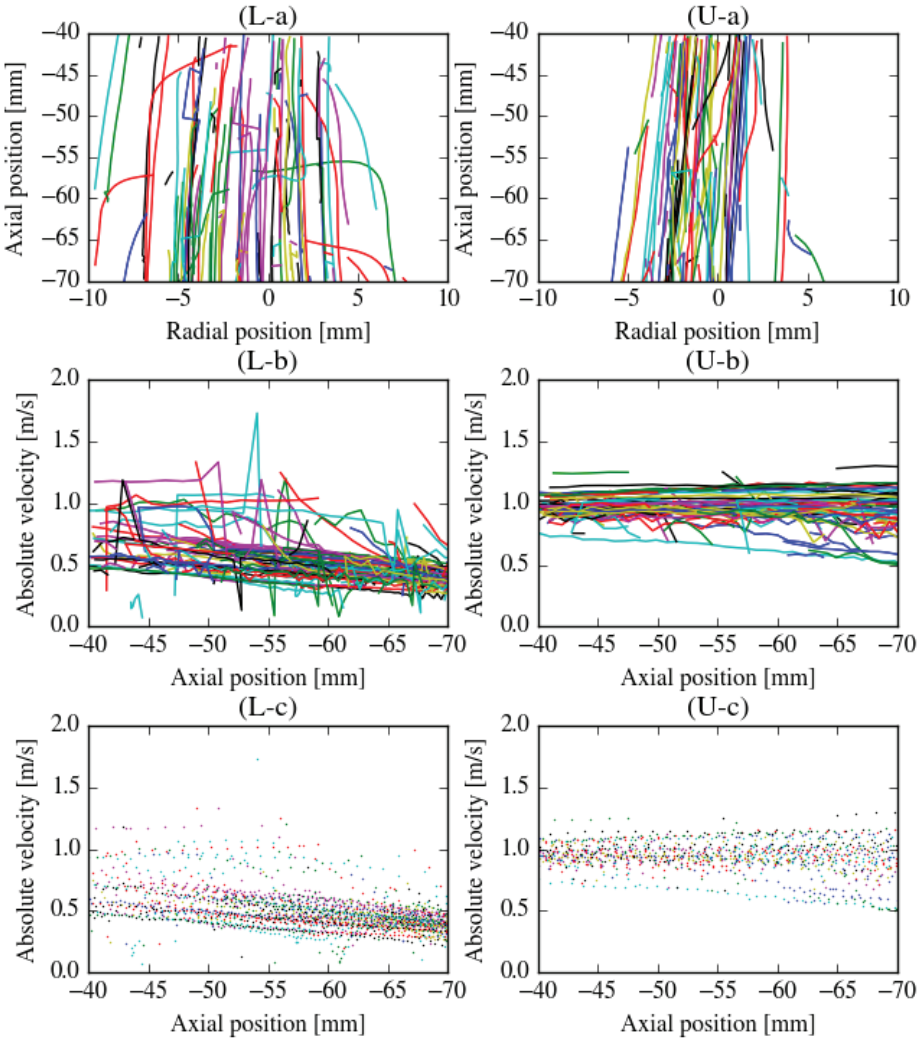

Fig. 16 Particle trajectory and absolute velocity in relation to the reactor axial position after separating the lower and upper band.

(a) is the particle trajectory plot. (b) and (c) are particle absolute velocity over the reactor axial position in line and scatter plot, respectively. “L” and “U” represent the lower and upper band, respectively.

The above discussion shows the importance of the effects of rapid release of volatiles and supports the inclusion of the rocket force in CFD simulations. In order to further investigate the aforementioned phenomenon of velocity segregation, two CFD simulations has been executed. The first one is the original CFD simulation, which is described in Section 3 of Paper 3. It is without the inclusion of the rocket force model (see Chapter 3.3.2). The second CFD simulation has implemented the rocket force model but is otherwise the same. The results of particle axial velocity along reactor radial direction at 50 mm distance from burner outlet is shown in Fig. 17.

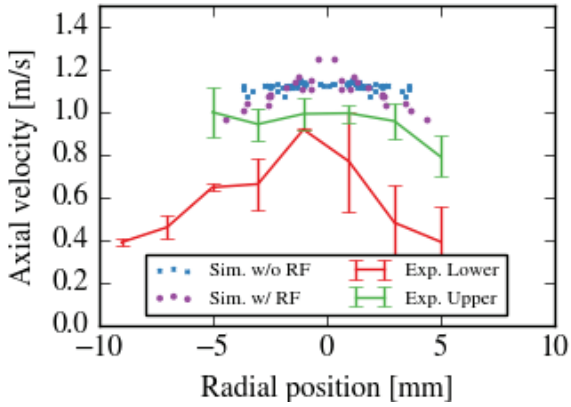

Fig. 17 Particle axial velocity along reactor radial direction at 50 mm distance away from burner outlet.
"Sim." and "Exp." mean simulation and experiment, respectively. "w/o RF" and "w/ RF" mean without and with rocket force model, respectively. "Lower" and "Upper" represent the aforementioned lower and upper band, respectively. Experimental data is based on three repetitions.

When comparing simulations with and without rocket force, one can see that particle axial velocity predicted by the simulation without rocket force results almost in a plateau along the radial direction. This plateau, however, is not reproduced by the simulation with rocket force included. Since the only difference between these two simulations are the inclusion or exclusion of the rocket force, it is reasonable to

assume that the rocket force is the cause for this. Note that the rocket force model assumes that the release rate of volatiles is not the same for all particles, as it is represented by the random factor *S* in Chapter 3.3.2. Therefore, particles are subject to different magnitudes of rocket force and have different velocities even if their other properties are the same. In addition, as previously mentioned, rocket forces can cause particles to have radial displacements towards the regions further away from the reactor centerline, where gas flow velocities are expected to be lower. Hence particles in the outer radial regions have higher drag forces and lower velocities when compared to particles closer to the reactor centerline.

When comparing experimental data from both bands, particles in the lower band, as expected, have lower velocities than the ones in the upper band. Velocities of particles in the upper band exhibits a similar plateau pattern along the radial direction, whereas the ones in the lower band do not. This is in line with the previous observation that there are more particles affected by the rapid release of volatiles in the lower band.

If one compares the simulation results with experimental ones, one should keep in mind that there are systematic errors, largely due to gas flow asymmetry and temperature field discrepancy. The simulation without rocket force matches reasonably well with experimental data in the upper band, where less particles are expected to be affected by rapid release of volatiles. This further validates the simulation models without the rocket force. However, there are larger differences between the simulation with rocket force and the experiment in the lower band, where more particles are believed to be influenced by the rapid release of volatiles. Based on this, it is believed that the current model for rocket force still needs improvement.

In summary, some biomass particles are observed to have sudden motions that significantly deviates from the average mainstream and it is believed to be caused by the rapid release of volatiles from the biomass particles. CFD simulations were conducted and shows that rocket force does indeed affect particle velocities, which in turn could alter particle thermochemical conversion histories. It is also found that a

more precise rocket force model should be developed based on more detailed experimental data and its effects in CFD simulations should be further investigated.

6 CONCLUSIONS AND OUTLOOKS

6.1 Main conclusions and contributions

A spheroid model framework has been implemented into the open source CFD platform OpenFOAM. This new framework aims to compensate for the shortcomings of current common practice in modelling of momentum and heat transfer between non-spherical biomass particles and their surrounding gases, with special focus on conditions relevant for entrained flow gasification. After model verification and validation, CFD simulations of both non-reactive and reactive conditions have been conducted using the spheroid model and their results have been compared to that of other common modelling approaches. By comparing operating parameters such as particle velocity, residence time, and gas species concentration, the differences between these models are quantitatively observed and reported.

Drop tube experiments have been conducted and helps to understand particle hydrodynamics, morphology and evolutions under fast heating and high temperature conditions. The obtained information on particle velocity, size and shape provides quantitative data for model validation. This work also revealed, together with additional CFD data, the effect of rapid release of volatiles on the particle's motion, and it is evident that this should not be ignored in further CFD simulations.

6.2 Outlooks and future recommendations

Further efforts in particle modelling is needed. The work in this thesis assumes constant density and aspect ratios of biomass particles. This, however, deviates from reality. Particle mass losses are combined effects due to changes in density, size and aspect ratio (or morphological characteristics, to be precise), which in turn influences particle hydrodynamic behaviors as well as thermochemical conversion histories. In addition to the factors that attribute particle mass losses, modelling efforts on particle forces also deserve improvements, especially for rocket force. All the above point towards that the effects from the aforementioned factors on the particle level are uncertain and need to be further quantitatively analyzed.

Apart from particle aspects, other simulation efforts could also be made for entrained flow gasification processes of biomass particles. First, the temperature boundary condition could be configured in a more realistic way. It was set as isothermal in Paper 3 and it was believed to the main cause that syngas production at the outlet was almost indifferent to model selections. In addition, more than only one operating condition should be simulated with different air-fuel ratio, gas flow rate, wood species, etc. This would expand the validity and applicability of the current modelling approaches into a wider range of conditions.

Despite that the primary focus of the thesis is simulations, it does not mean further efforts in experiments are not needed. On the contrary, discrepancies displayed in the thesis between simulations and experiments show that further efforts in the experiments are required. In the context of the thesis, it is rare to find experimental data of temporal development of particle position, geometry, orientation and temperature under conditions similar to entrained flow gasification processes, where multiple particles are subject to turbulent flow, high temperatures, fast heating rates and short residence times. They are difficult to be accurately measured and require carefully designed experimental facilities. Due to this, many biomass models are based on experimental data from other and more controlled operating conditions (for example, single or a few particles heated in a TGA or DTR). Studies with these models

are often compared to experimental data of gas flow fields (such as, temperature, species concentration, etc.) and argue that the models are indirectly validated. However, these are not the direct support of model validity and their applicable ranges are often subject to challenge, especially when detailed and localized information of particle-flow fields are of interest. In the opinion of the author, more experimental data are needed to provide particle information and aim to build the basis for model development of biomass particles. Specifically, it is highly advised to have better temperature measurements of gas flows and reactor boundaries under reactive conditions, with and without biomass particles injected. Accurate temperature measurements could help to configure validate CFD simulations of flow fields. On one hand, it could make the particle model validation easier since it could reduce the deviation caused by gas flow fields. On the other hand, if CFD simulations are used for prediction purposes, the differences among the four modelling approaches in Paper 3 are likely to be more pronounced. Finally, particle temperature information under reactive conditions are of great interest. Although they are difficult to be accurately measured, they provide valuable insights for particle model development, validation and application for prediction.

REFERENCES

[1] IEA. CO2 Emissions from Fuel Combustion 2018. Paris: OECD; 2018. https://doi.org/10.1787/co2_fuel-2018-en.

[2] Köhler J, Walz R, Marscheder-Weidemann F, Thedieck B. Lead markets in 2nd generation biofuels for aviation: A comparison of Germany, Brazil and the USA. Environ Innov Soc Transitions 2014;10:59–76. https://doi.org/10.1016/j.eist.2013.10.003.

[3] Taylor G. Biofuels and the biorefinery concept. Energy Policy 2008;36:4406–9. https://doi.org/10.1016/J.ENPOL.2008.09.069.

[4] Molino A, Chianese S, Musmarra D. Biomass gasification technology: The state of the art overview. J Energy Chem 2016;25:10–25. https://doi.org/10.1016/j.jechem.2015.11.005.

[5] Russo D, Dassisti M, Lawlor V, Olabi AG. State of the art of biofuels from pure plant oil. Renew Sustain Energy Rev 2012;16:4056–70. https://doi.org/10.1016/j.rser.2012.02.024.

[6] Afzal S, Blank J, Hussain R, Elbashir NO. Modeling Fischer-Tropsch Product Distribution of a Cobalt-based Catalyst in Different Reaction Media. Proc. 4th Int. Gas Process. Symp., Elsevier; 2015, p. 81–8. https://doi.org/10.1016/b978-0-444-63461-0.50008-0.

[7] Weber K, Quicker P. Properties of biochar. Fuel 2018;217:240–61. https://doi.org/10.1016/j.fuel.2017.12.054.

[8] Roy P, Dias G. Prospects for pyrolysis technologies in the bioenergy sector: A review. Renew Sustain Energy Rev 2017;77:59–69. https://doi.org/10.1016/j.rser.2017.03.136.

[9] Akhtar A, Krepl V, Ivanova T. A Combined Overview of Combustion, Pyrolysis, and Gasification of Biomass. Energy and Fuels 2018;32:7294–318. https://doi.org/10.1021/acs.energyfuels.8b01678.

[10] Puig-Arnavat M, Bruno JC, Coronas A. Review and analysis of biomass gasification models. Renew Sustain Energy Rev 2010;14:2841–51. https://doi.org/10.1016/j.rser.2010.07.030.

[11] Kirkels AF, Verbong GPJ. Biomass gasification: Still promising? A 30-year global overview. Renew Sustain Energy Rev 2011;15:471–81. https://doi.org/10.1016/j.rser.2010.09.046.

[12] Gómez-Barea A, Leckner B. Modeling of biomass gasification in fluidized bed. Prog Energy Combust Sci 2010;36:444–509. https://doi.org/10.1016/j.pecs.2009.12.002.

[13] Buragohain B, Mahanta P, Moholkar VS. Biomass gasification for decentralized power generation: The Indian perspective. Renew Sustain Energy Rev 2010;14:73–92. https://doi.org/10.1016/j.rser.2009.07.034.

[14] Sansaniwal SK, Pal K, Rosen MA, Tyagi SK. Recent advances in the development of biomass gasification technology: A comprehensive review. Renew Sustain Energy Rev 2017;72:363–84. https://doi.org/10.1016/j.rser.2017.01.038.

[15] Qin K, Lin W, Jensen PA, Jensen AD. High-temperature entrained flow gasification of biomass. Fuel 2012;93:589–600. https://doi.org/10.1016/j.fuel.2011.10.063.

[16] Weiland F, Hedman H, Marklund M, Wiinikka H, Öhrman O, Gebart R. Pressurized oxygen blown entrained-flow gasification of wood powder. Energy and Fuels 2013;27:932–41. https://doi.org/10.1021/ef301803s.

[17] Alakangas E. European Standards for Fuel Specification and Classes of Solid Biofuels. In: Grammelis P, editor. Solid Biofuels Energy A Low. Greenh. Gas Altern., London: Springer London; 2011, p. 21–41. https://doi.org/10.1007/978-1-84996-393-0_2.

[18] Pecha MB, Arbelaez JIM, Garcia-Perez M, Chejne F, Ciesielski PN. Progress in understanding the four dominant intra-particle phenomena of lignocellulose pyrolysis: chemical reactions, heat transfer, mass transfer, and phase change. Green Chem 2019;21:2868–98. https://doi.org/10.1039/C9GC00585D.

[19] Haberle I, Skreiberg Ø, Łazar J, Haugen NEL. Numerical models for thermochemical degradation of thermally thick woody biomass, and their application in domestic wood heating appliances and grate furnaces. Prog Energy Combust Sci 2017;63:204–52. https://doi.org/10.1016/j.pecs.2017.07.004.

[20] Vassilev S V., Vassileva CG, Vassilev VS. Advantages and disadvantages of composition and properties of biomass in comparison with coal: An overview. Fuel 2015;158:330–50. https://doi.org/10.1016/J.FUEL.2015.05.050.

[21] Tabet F, Gökalp I. Review on CFD based models for co-firing coal and biomass. Renew Sustain Energy Rev 2015;51:1101–14. https://doi.org/10.1016/J.RSER.2015.07.045.

[22] Yin C, Rosendahl L, K. Kær S, J. Condra T. Use of numerical modeling in design for co-firing biomass in wall-fired burners. Chem Eng Sci 2004;59:3281–92. https://doi.org/10.1016/J.CES.2004.04.036.

[23] Gao X, Zhang Y, Li B, Yu X. Model development for biomass gasification in an entrained flow gasifier using intrinsic reaction rate submodel. Energy Convers Manag 2016;108:120–31. https://doi.org/10.1016/j.enconman.2015.10.070.

[24] Ku X, Jin H, Lin J. Comparison of gasification performances between raw and torrefied biomasses in an air-blown fluidized-bed gasifier. Chem Eng Sci 2017;168:235–49. https://doi.org/10.1016/j.ces.2017.04.050.

[25] Simone M, Biagini E, Galletti C, Tognotti L. Evaluation of global biomass devolatilization kinetics in a drop tube reactor with CFD aided experiments. Fuel 2009;88:1818–27. https://doi.org/10.1016/j.fuel.2009.04.032.

[26] Li T, Wang L, Ku X, Güell BM, Løvås T, Shaddix CR. Experimental and modeling study of the effect of torrefaction on the rapid devolatilization of biomass. Energy and Fuels 2015;29:4328–38. https://doi.org/10.1021/acs.energyfuels.5b00348.

[27] Gubba SR, Ma L, Pourkashanian M, Williams A. Influence of particle shape and internal thermal gradients of biomass particles on pulverised coal/biomass co-fired flames. Fuel Process Technol 2011;92:2185–95. https://doi.org/10.1016/j.fuproc.2011.07.003.

[28] Panahi A, Levendis YA, Vorobiev N, Schiemann M. Direct observations on the combustion characteristics of Miscanthus and Beechwood biomass including fusion and spherodization. Fuel Process Technol 2017;166:41–9. https://doi.org/10.1016/j.fuproc.2017.05.029.

[29] van Wachem B, Zastawny M, Zhao F, Mallouppas G. Modelling of gas-solid turbulent channel flow with non-spherical particles with large Stokes numbers. Int J Multiph Flow 2015;68:80–92. https://doi.org/10.1016/j.ijmultiphaseflow.2014.10.006.

[30] Njobuenwu DO, Fairweather M. Simulation of inertial fibre orientation in turbulent flow. Phys Fluids 2016;28:063307. https://doi.org/10.1063/1.4954214.

[31] Li J, Zhang J. Analytical study on char combustion of spheroidal particles under forced convection. Powder Technol 2017;313:210–7. https://doi.org/10.1016/j.powtec.2017.02.054.

[32] Lu H, Ip E, Scott J, Foster P, Vickers M, Baxter LL. Effects of particle shape and size on devolatilization of biomass particle. Fuel 2010;89:1156–68. https://doi.org/10.1016/J.FUEL.2008.10.023.

[33] Di Blasi C. Modeling chemical and physical processes of wood and biomass pyrolysis. Prog Energy Combust Sci 2008;34:47–90. https://doi.org/10.1016/j.pecs.2006.12.001.

[34] Di Blasi C. Combustion and gasification rates of lignocellulosic chars. Prog Energy Combust Sci 2009;35:121–40. https://doi.org/10.1016/j.pecs.2008.08.001.

[35] Sikarwar VS, Zhao M, Clough P, Yao J, Zhong X, Memon MZ, et al. An overview of advances in biomass gasification. Energy Environ Sci 2016;9:2939–77. https://doi.org/10.1039/C6EE00935B.

[36] Chen WH, Chen CJ, Hung CI, Shen CH, Hsu HW. A comparison of gasification phenomena among raw biomass, torrefied biomass and coal in an entrained-flow reactor. Appl Energy 2013;112:421–30. https://doi.org/10.1016/j.apenergy.2013.01.034.

[37] Weiland F, Nordwaeger M, Olofsson I, Wiinikka H, Nordin A. Entrained flow gasification of torrefied wood residues. Fuel Process Technol 2014;125:51–8. https://doi.org/10.1016/j.fuproc.2014.03.026.

[38] Li J, Brzdekiewicz A, Yang W, Blasiak W. Co-firing based on biomass torrefaction in a pulverized coal boiler with aim of 100% fuel switching.

Appl Energy 2012;99:344–54.
https://doi.org/10.1016/j.apenergy.2012.05.046.

[39] He Q, Guo Q, Ding L, Wei J, Yu G. CO2 gasification of char from raw and torrefied biomass: Reactivity, kinetics and mechanism analysis. Bioresour Technol 2019;293:122087. https://doi.org/10.1016/j.biortech.2019.122087.

[40] Li T, Geier M, Wang L, Ku X, Güell BM, Løvås T, et al. Effect of Torrefaction on Physical Properties and Conversion Behavior of High Heating Rate Char of Forest Residue. Energy & Fuels 2015;29:177–84. https://doi.org/10.1021/ef5016044.

[41] Ku X, Lin J, Yuan F. Influence of Torrefaction on Biomass Gasification Performance in a High-Temperature Entrained-Flow Reactor. Energy and Fuels 2016;30:4053–64. https://doi.org/10.1021/acs.energyfuels.6b00163.

[42] Brachi P, Chirone R, Miccio F, Miccio M, Ruoppolo G. Entrained-flow gasification of torrefied tomato peels: Combining torrefaction experiments with chemical equilibrium modeling for gasification. Fuel 2018;220:744–53. https://doi.org/10.1016/j.fuel.2018.02.027.

[43] Wagner DR, Holmgren P, Skoglund N, Broström M. Design and validation of an advanced entrained flow reactor system for studies of rapid solid biomass fuel particle conversion and ash formation reactions. Rev Sci Instrum 2018;89:065101. https://doi.org/10.1063/1.5030603.

[44] Ögren Y, Tóth P, Garami A, Sepman A, Wiinikka H. Development of a vision-based soft sensor for estimating equivalence ratio and major species concentration in entrained flow biomass gasification reactors. Appl Energy 2018;226:450–60. https://doi.org/10.1016/j.apenergy.2018.06.007.

[45] Qu Z, Holmgren P, Skoglund N, Wagner DR, Broström M, Schmidt FM. Distribution of temperature, H2O and atomic potassium during entrained flow biomass combustion – Coupling in situ TDLAS with modeling

approaches and ash chemistry. Combust Flame 2018;188:488–97. https://doi.org/10.1016/j.combustflame.2017.10.013.

[46] Qin K, Lin W, Fæster S, Jensen PA, Wu H, Jensen AD. Characterization of residual particulates from biomass entrained flow gasification. Energy and Fuels 2013;27:262–70. https://doi.org/10.1021/ef301432q.

[47] Schulze S, Richter A, Vascellari M, Gupta A, Meyer B, Nikrityuk PA. Novel intrinsic-based submodel for char particle gasification in entrained-flow gasifiers: Model development, validation and illustration. Appl Energy 2016;164:805–14. https://doi.org/10.1016/j.apenergy.2015.12.018.

[48] Gao X, Zhang Y, Bao F, Li B, Zhao Y, Ke C, et al. CFD modeling of sawdust gasification in a lab-scale entrained flow reactor based on char intrinsic kinetics. Part 1: Model development. Chem Eng Process - Process Intensif 2018;125:280–9. https://doi.org/10.1016/j.cep.2018.02.017.

[49] Dhanavath KN, Shah K, Islam MS, Ronte A, Parthasarathy R, Bhargava SK, et al. Experimental investigations on entrained flow gasification of Torrefied Karanja Press Seed Cake. J Environ Chem Eng 2018;6:1242–9. https://doi.org/10.1016/j.jece.2017.12.061.

[50] Ismail WMSW, Mohd Thaim T, Abdul Rasid R. Biomass gasification of oil palm fronds (OPF) and Koompassia malaccensis (Kempas) in an entrained flow gasifier: A performance study. Biomass and Bioenergy 2019;124:83–7. https://doi.org/10.1016/j.biombioe.2019.03.012.

[51] Weiland F, Wiinikka H, Hedman H, Wennebro J, Pettersson E, Gebart R. Influence of process parameters on the performance of an oxygen blown entrained flow biomass gasifier. Fuel 2015;153:510–9. https://doi.org/10.1016/j.fuel.2015.03.041.

[52] Ku X, Wang J, Jin H, Lin J. Effects of operating conditions and reactor structure on biomass entrained-flow gasification. Renew Energy 2019;139:781–95. https://doi.org/10.1016/j.renene.2019.02.113.

[53] Ku X, Li T, Løvås T. CFD-DEM simulation of biomass gasification with steam in a fluidized bed reactor. Chem Eng Sci 2015;122:270–83. https://doi.org/10.1016/j.ces.2014.08.045.

[54] Andersson B, Andersson R, Håkansson L, Mortensen M, Sudiyo R, Van Wachem B. Computational fluid dynamics for engineers. 2011. https://doi.org/10.1017/CBO9781139093590.

[55] Elgobashi S. An Updated Classification Map of Particle-Laden Turbulent Flows. In: Balachandar S, Prosperetti A, editors. IUTAM Symp. Comput. Approaches to Multiph. Flow, Dordrecht: Springer Netherlands; 2006, p. 3–10. https://doi.org/10.1007/1-4020-4977-3_1.

[56] Guo N, Li T, Zhao L, Løvås T. Eulerian-Lagrangian simulation of pulverized biomass jet using spheroidal particle approximation. Fuel 2019;239:636–51. https://doi.org/10.1016/j.fuel.2018.10.137.

[57] Bonefacic I, Frankovic B, Kazagic A. Cylindrical particle modelling in pulverized coal and biomass co-firing process. Appl Therm Eng 2015;78:74–81. https://doi.org/10.1016/j.applthermaleng.2014.12.047.

[58] Ren B, Zhong W, Chen Y, Chen X, Jin B, Yuan Z, et al. CFD-DEM simulation of spouting of corn-shaped particles. Particuology 2012;10:562–72. https://doi.org/10.1016/j.partic.2012.03.011.

[59] Ciesielski PN, Crowley MF, Nimlos MR, Sanders AW, Wiggins GM, Robichaud D, et al. Biomass particle models with realistic morphology and resolved microstructure for simulations of intraparticle transport phenomena. Energy and Fuels 2015;29:242–54. https://doi.org/10.1021/ef502204v.

[60] Vorobiev N, Becker A, Kruggel-Emden H, Panahi A, Levendis YA, Schiemann M. Particle shape and Stefan flow effects on the burning rate of torrefied biomass. Fuel 2017;210:107–20. https://doi.org/10.1016/j.fuel.2017.08.037.

[61] Stokes GG. On the Effect of the Internal Friction of Fluids on the Motion of Pendulums. Math. Phys. Pap., Cambridge: Cambridge University Press; 2009, p. 1–10. https://doi.org/10.1017/CBO9780511702266.002.

[62] Parmar M, Haselbacher A, Balachandar S. Equation of motion for a sphere in non-uniform compressible flows. J Fluid Mech 2012;699:352–75. https://doi.org/10.1017/jfm.2012.109.

[63] OpenFOAM v5.0 C++ Source Code Guide n.d. https://cpp.openfoam.org/v5/SphereDragForce_8C_source.html (accessed September 25, 2017).

[64] Haider A, Levenspiel O. Drag coefficient and terminal velocity of spherical and nonspherical particles. Powder Technol 1989;58:63–70. https://doi.org/10.1016/0032-5910(89)80008-7.

[65] Hölzer A, Sommerfeld M. New simple correlation formula for the drag coefficient of non-spherical particles. Powder Technol 2008;184:361–5. https://doi.org/10.1016/j.powtec.2007.08.021.

[66] Jeffery GB. The Motion of Ellipsoidal Particles Immersed in a Viscous Fluid. Proc R Soc A Math Phys Eng Sci 1922;102:161–79. https://doi.org/10.1098/rspa.1922.0078.

[67] Mandø M, Rosendahl L. On the motion of non-spherical particles at high Reynolds number. Powder Technol 2010;202:1–13. https://doi.org/10.1016/j.powtec.2010.05.001.

[68] Zastawny M, Mallouppas G, Zhao F, van Wachem B. Derivation of drag and lift force and torque coefficients for non-spherical particles in flows. Int J Multiph Flow 2012;39:227–39. https://doi.org/10.1016/j.ijmultiphaseflow.2011.09.004.

[69] Rosendahl L. Using a multi-parameter particle shape description to predict the motion of non-spherical particle shapes in swirling flow. Appl Math Model 2000;24:11–25. https://doi.org/10.1016/S0307-904X(99)00023-2.

[70] Ullah A, Hong K, Gao Y, Gungor A, Zaman M. An overview of Eulerian CFD modeling and simulation of non-spherical biomass particles. Renew Energy 2019;141:1054–66. https://doi.org/10.1016/j.renene.2019.04.074.

[71] Elfasakhany A, Tao L, Espenas B, Larfeldt J, Bai XS. Pulverised wood combustion in a vertical furnace: Experimental and computational analyses. Appl Energy 2013;112:454–64. https://doi.org/10.1016/j.apenergy.2013.04.051.

[72] Brackmann C, Aldén M, Bengtsson PE, Davidsson KO, Pettersson JBC. Optical and mass spectrometric study of the pyrolysis gas of wood particles. Appl Spectrosc 2003;57:216–22. https://doi.org/10.1366/000370203321535141.

[73] Ranz WE, Marshall Jr. WR. Evaporation from drops - Part I. Chem Eng Prog 1952.

[74] Ranz WE, Marshall Jr. WR. Evaporation from drops - Part II. Chem Eng Prog 1952.

[75] Hughmark GA. Mass and heat transfer from rigid spheres. AIChE J 1967;13:1219–21. https://doi.org/10.1002/aic.690130638.

[76] Whitaker S. Forced convection heat transfer correlations for flow in pipes, past flat plates, single cylinders, single spheres, and for flow in packed beds and tube bundles. AIChE J 1972;18:361–71. https://doi.org/10.1002/aic.690180219.

[77] Sparrow EM, Abraham JP, Tong JCK. Archival correlations for average heat transfer coefficients for non-circular and circular cylinders and for spheres in

cross-flow. Int J Heat Mass Transf 2004;47:5285–96. https://doi.org/10.1016/j.ijheatmasstransfer.2004.06.024.

[78] Richter A, Nikrityuk PA. Drag forces and heat transfer coefficients for spherical, cuboidal and ellipsoidal particles in cross flow at sub-critical Reynolds numbers. Int J Heat Mass Transf 2012;55:1343–54. https://doi.org/10.1016/j.ijheatmasstransfer.2011.09.005.

[79] Richter A, Nikrityuk PA. New correlations for heat and fluid flow past ellipsoidal and cubic particles at different angles of attack. Powder Technol 2013;249:463–74. https://doi.org/10.1016/j.powtec.2013.08.044.

[80] Ke C, Shu S, Zhang H, Yuan H, Yang D. On the drag coefficient and averaged Nusselt number of an ellipsoidal particle in a fluid. Powder Technol 2018;325:134–44. https://doi.org/10.1016/J.POWTEC.2017.10.049.

[81] Zhang H, Xiong B, An X, Ke C, Wei G. Prediction on drag force and heat transfer of spheroids in supercritical water: A PR-DNS study. Powder Technol 2019;342:99–107. https://doi.org/10.1016/j.powtec.2018.09.051.

[82] Zhang H, Xiong B, An X, Ke C, Wei G. Numerical investigation on the effect of the incident angle on momentum and heat transfer of spheroids in supercritical water. Comput Fluids 2019;179:533–42. https://doi.org/10.1016/j.compfluid.2018.11.026.

[83] Zhang H, Xiong B, An X, Ke C, Chen J. Numerical prediction on the drag force and heat transfer of non-spherical particles in supercritical water. Powder Technol 2019. https://doi.org/10.1016/j.powtec.2019.07.032.

[84] Kishore N, Gu S. Effect of Blockage on Heat Transfer Phenomena of Spheroid Particles at Moderate Reynolds and Prandtl Numbers. Chem Eng Technol 2011;34:1551–8. https://doi.org/10.1002/ceat.201100007.

[85] Gerhardter H, Prieler R, Schluckner C, Knoll M, Hochenauer C, Mühlböck M, et al. Modelling convective heat transfer to non-spherical particles.

Powder Technol 2019;343:245–54.
https://doi.org/10.1016/J.POWTEC.2018.11.031.

[86] Gerhardter H, Knoll M, Prieler R, Landfahrer M, Mühlböck M, Tomazic P, et al. Determining the heating characteristics of non-spherical particles in combusting flows. Appl Therm Eng 2019;151:124–33.
https://doi.org/10.1016/j.applthermaleng.2019.02.006.

[87] Kriebitzsch S, Richter A. LES simulation of char particle gasification at Reynolds numbers up to 1000. Combust Flame 2020;211:185–94.
https://doi.org/10.1016/J.COMBUSTFLAME.2019.08.028.

[88] Simonsson J, Bladh H, Gullberg M, Pettersson E, Sepman A, Ögren Y, et al. Soot Concentrations in an Atmospheric Entrained Flow Gasifier with Variations in Fuel and Burner Configuration Studied Using Diode-Laser Extinction Measurements. Energy & Fuels 2016;30:2174–86.
https://doi.org/10.1021/acs.energyfuels.5b02561.

[89] Mehrabian R, Scharler R, Obernberger I. Effects of pyrolysis conditions on the heating rate in biomass particles and applicability of TGA kinetic parameters in particle thermal conversion modelling. Fuel 2012;93:567–75.
https://doi.org/10.1016/j.fuel.2011.09.054.

[90] Jiménez S, Remacha P, Ballesteros JC, Giménez A, Ballester J. Kinetics of devolatilization and oxidation of a pulverized biomass in an entrained flow reactor under realistic combustion conditions. Combust Flame 2008;152:588–603.
https://doi.org/10.1016/J.COMBUSTFLAME.2007.10.001.

[91] Johansen JM, Gadsbøll R, Thomsen J, Jensen PA, Glarborg P, Ek P, et al. Devolatilization kinetics of woody biomass at short residence times and high heating rates and peak temperatures. Appl Energy 2016;162:245–56.
https://doi.org/10.1016/j.apenergy.2015.09.091.

[92] Weber K, Li T, Løvås T, Perlman C, Seidel L, Mauss F. Stochastic reactor modeling of biomass pyrolysis and gasification. J Anal Appl Pyrolysis 2017;124:592–601. https://doi.org/10.1016/j.jaap.2017.01.003.

[93] Papari S, Hawboldt K. A review on the pyrolysis of woody biomass to bio-oil: Focus on kinetic models. Renew Sustain Energy Rev 2015;52:1580–95. https://doi.org/10.1016/j.rser.2015.07.191.

[94] Hosoya T, Kawamoto H, Saka S. Cellulose-hemicellulose and cellulose-lignin interactions in wood pyrolysis at gasification temperature. J Anal Appl Pyrolysis 2007;80:118–25. https://doi.org/10.1016/j.jaap.2007.01.006.

[95] Shafizadeh F. Introduction to pyrolysis of biomass. J Anal Appl Pyrolysis 1982;3:283–305. https://doi.org/10.1016/0165-2370(82)80017-X.

[96] Ranzi E, Cuoci A, Faravelli T, Frassoldati A, Migliavacca G, Pierucci S, et al. Chemical kinetics of biomass pyrolysis. Energy and Fuels 2008;22:4292–300. https://doi.org/10.1021/ef800551t.

[97] Baruah D, Baruah DC. Modeling of biomass gasification: A review. Renew Sustain Energy Rev 2014;39:806–15. https://doi.org/10.1016/j.rser.2014.07.129.

[98] Ku X, Li T, Løvås T. Eulerian–Lagrangian Simulation of Biomass Gasification Behavior in a High-Temperature Entrained-Flow Reactor. Energy & Fuels 2014;28:5184–96. https://doi.org/10.1021/ef5010557.

SELECTED PAPERS

Paper 1

Eulerian-Lagrangian simulation of pulverized biomass jet using spheroidal particle approximation

Guo, Ning; Li, Tian; Zhao, Lihao; Løvås, Terese.

Fuel, Volume 239, 1 March 2019, Pages 636-651

https://doi.org/10.1016/j.fuel.2018.10.13

Fuel 239 (2019) 636–651

Contents lists available at ScienceDirect

Fuel

journal homepage: www.elsevier.com/locate/fuel

Full Length Article

Eulerian-Lagrangian simulation of pulverized biomass jet using spheroidal particle approximation

Ning Guo[a], Tian Li[a,*], Lihao Zhao[b,a], Terese Løvås[a]

[a] Department of Energy and Process Engineering, Faculty of Engineering, NTNU – Norwegian University of Science and Technology, Trondheim, Norway
[b] Department of Engineering Mechanics, Tsinghua University, Beijing, China

ARTICLE INFO

Keywords:
Spheroidal particle
Pulverized biomass
CFD
Entrained flow gasifier
OpenFOAM

ABSTRACT

Pulverized biomass has great potential to replace coal in many industrial systems such as suspension-firing furnaces and entrained-flow gasifiers. The shape of pulverized biomass deviates significantly from the quasi-spherical coal particle, however, it is common to simulate pulverized biomass particles as spheres as most biomass models are developed based on coal models. With the aim of obtaining a more realistic simulation of pulverized biomass, this work extends the treatment of pulverized biomass to spheroids. A spheroid model that accounts for spheroidal particle drag force and torque was implemented into an Eulerian-Lagrange computational fluid dynamic solver. Comprehensive verifications and validations were performed by comparing with experiments and direct numerical simulations. Furthermore, non-reactive simulations of a lab-scale entrained flow gasifier were carried out using a conventional spherical particle model, a simplified non-sphere model, and the implemented detailed spheroidal particle model. By studying the simulation results of particle and fluid velocities in axial, radial and tangential directions, differences were observed when comparing the sphere model, the simplified non-sphere model, and the spheroid model. The spheroid model shows that particle orientation, which is ignored in the sphere model and the simplified non-sphere model, plays a role in the behavior of the particle dynamics. It was also found that, under such conditions, the spheroid model, compared to the sphere model, yields a more dispersed distribution regarding the particle residence time and local concentration. These non-reactive simulation results imply that shortcomings may exist in the common practice of simulating conversion of pulverized biomass in which the sphere model or the simplified non-sphere model is applied.

1. Introduction

In order to address the increasing concerns related to the use of fossil fuels for both heat and power as well as fuel production [1], it is of interest to investigate the sustainable use of alternative fuels to replace traditional fossil fuels. One viable option is to utilize biomass. For example, liquid biofuels can be produced via entrained flow gasification. In this process, pulverized biomass is gasified in an entrained flow gasifier and the produced bio-syngas is further converted into liquid hydrocarbons by Fischer-Tropsch synthesis [2].

Due to the fibrous nature of bio-based feedstock, pulverized biomass particles come in various shapes. For example, scanning electron microscope images of Norwegian spruce and forest residuals show that particles are mainly large needle-like oblongs [3]. Gubba et al. [4] presented electron microscopy images of milled wood and palm kernel expeller and showed particle shapes varying from cylinders, spheres, slabs and other irregular shapes. Panahi et al. [5] published optical microscope photographs of pulverized Miscanthus and Beechwood particles and showed that most of them are cylinder-like in shape. Despite the shape of pulverized biomass particles being non-spherical, the majority of research up until recently use spheres to represent pulverized biomass particles in computational fluid dynamic (CFD) simulations [6–8]. This simplification may lead to several problems related to the predictability of such models for larger applications. To begin with, given the same flow field, spherical and non-spherical particles have different hydrodynamic behavior due to the difference in hydrodynamic drag and torque. Drag forces are dependent on particle cross-sectional areas projected to flow directions. Values of the particle cross-sectional projected area vary in the case of non-spheres as they will rotate, but cross-sectional projected areas remain constant for spheres. Furthermore, particle torques, which are often ignored in simulations of spheres due to central symmetry, have to be included in simulations when particles are non-spherical to account for particle rotations. In addition to hydrodynamic considerations, the particle heat

* Corresponding author.
E-mail address: tian.li@ntnu.no (T. Li).

https://doi.org/10.1016/j.fuel.2018.10.137
Received 1 June 2018; Received in revised form 13 August 2018; Accepted 29 October 2018

Nomenclature

Notation	Description
$\boldsymbol{A}$	transformation matrix
a	spheroid minor axis [m]
B_1, B_2, B_3, B_4	model coefficients based on particle sphericity
C_D	drag force coefficient
c	spheroid major axis [m]
D	central tube diameter [m]
D_{jet}	jet diameter in drag model verification [m]
D_p	particle diameter [m]
d_{ij}	deformation rate [s^{-1}]
e_0, e_1, e_2, e_3	Euler parameters
F_D	particle drag force [N]
I	particle moment of inertia [kg·m^2]
i, j, k	tensor notation indices
m_p	particle mass [kg]
N	particle torque [N·m]
Re_p	particle Reynolds number
r	radial coordinate [m]
t	time [s]
U_c	centerline velocity [m/s]
U_e	jet exit velocity [m/s]
U_f	fluid velocity [m/s]
U_p	particle velocity [m/s]
U_r	radial velocity [m/s]
U_z	axial velocity [m/s]
U_τ	tangential velocity [m/s]
w_{ij}	spin tensor [s^{-1}]
$\boldsymbol{x}$	inertial frame
$\boldsymbol{x}$' or '	particle frame
$\boldsymbol{x}$" or "	co-moving frame
x, y, z	coordinates in x-, y-, z-direction, respectively [m]
α_0, β_0, γ_0	dimensionless parameters
λ	particle aspect ratio
μ_f	fluid dynamic viscosity [N·s/m^2]
ν_f	fluid kinematic viscosity [m^2/s]
ρ_f	fluid density [kg/m^3]
ϕ	sphericity
$\phi_{\parallel}$	lengthwise sphericity
$\phi_{\perp}$	crosswise sphericity
ω	angular velocity [rad/s]

and mass transfer of non-spheres are likely to be different from spheres. These are all factors that have influence on particle trajectories, residence times, heat transfer, and temporal developments of particle conversion. Without considering these aforementioned effects, simulations employing the spherical particle assumption would fail to capture details of the thermal conversion of pulverized biomass observed in experiments.

To remedy these issues, efforts have been made to investigate the behavior of non-spherical particles in flow systems. From particle hydrodynamics perspective, Zhang et al. [9] carried out numerical investigations of particle dispersion in detail and found that particle shapes affects the dispersity. Wachem et al. [10] simulated spherical, ellipsoidal, disc and fiber shaped particles in turbulent channel flow with large Stokes numbers and a mass loading factor of unity. Their study shows that non-spherical particles are most stable when their longest axes are perpendicular to the flow, which makes them having higher average velocities than spherical particles with equivalent volume. These works all contributed to the understanding of the differences of dynamics between spherical and non-spherical particles. One important force affecting the dynamics of a non-spherical particle is the drag force. Numerical studies on modelling drag forces of non-spherical particles can be generally classified into two categories. The first approach is to use simple shape factors (such as particle sphericity) to account for the irregular shapes of non-spherical particles and then to modify the drag coefficients based on the said shape factors. However, such method does not consider the effects of particle orientations. A typical example of this approach is the simplified non-sphere model developed by Haider and Levenspiel [11], which has been implemented into many mainstream CFD solvers including Ansys Fluent and OpenFOAM. This is one of the most commonly used model that takes account the shape of a particle and has been used in a handful CFD studies of biomass conversion [12,13]. Another approach of modelling the drag forces of non-spherical particle is to include the effects of particle orientations. This could be done either by introducing an inclination angle (angle between particle major axis and flow direction) as in the work of Rosendahl [14] or making particle sphericity or drag coefficient dependent on particle orientations as in the work of Hölzer and Sommerfield [15]. In addition, attention has been paid to heat and mass transfer processes of non-spherical particles. Schiemann et al. [16] studied effects of particle shape on char burning kinetics using imaging pyrometry, and it was concluded that particle shapes should be taken into account, otherwise it could lead to miss-interpretation of char burning rate. Vorobiev et al. [17] further included the influence of Stefan flow to study burning rates of torrefied biomass. A comprehensive model for char burnout kinetic that considers Stefan flow effects was presented in their paper. They reported that effects of Stefan flow are more pronounced in small particles with large aspect ratios. Grow [18] investigated heat and mass transfer for an ellipsoidal particle and showed that, in the case of diffusion controlled combustion, the average combustion rate of ellipsoidal particles are only slightly higher than spherical particle of the same surface area. This is confirmed by Li and Zhang [19] who conducted a theoretical study on spheroidal char particles under forced convection conditions and it was found that, in both diffusion controlled and diffusion-kinetic controlled cases, combustion rates increase with particle aspect ratios.

Although there is significant progress in research on simulating particles of non-spherical shape, studies concerning particle-laden jets using detailed description of spheroidal particle models in a reactor for thermochemical conversion of biomass are rare. To better simulate entrained flow gasification of pulverized biomass, a cold flow study with a more realistic approximation of the particle shape is hereby presented as a first step in this work. A spheroid model is implemented into an Eulerian-Lagrangian CFD solver using the open source CFD platform, OpenFOAM [20]. In this spheroid model, pulverized biomass particles are treated as needle-like spheroids. The drag force and torque acting on the particle are all taken into account. Since the proposed CFD solver includes particle torque calculations, the effects of particle orientations can be studied. This makes the proposed spheroid model different than other CFD studies works where biomass particles are simulated as non-spheres but particle orientations are not considered [12,13]. Furthermore, although the general trend of particle motions by assuming pulverized biomass particles as spheroids instead of spheres is easy to predict by qualitative analysis, quantitative information of differences between these approaches are rarely found in open literatures. The current research meets this need by presenting a comprehensive comparison of particle dynamics calculated from different models.

The logical development of this work and the structure of this paper are as follows. The theoretical foundation is explained in Section 2. In Section 3, the verifications and validations of the implemented spheroid model are discussed in two parts: torque and drag. With the validated model, cold flow simulations of a simplified entrained flow gasification reactor are executed in Section 4, where particle and fluid velocities in axial, radial and tangential directions are analyzed and results are

compared among those of the sphere model, the simplified non-sphere model, and the spheroid model. Particle residence times and concentrations are also studied. Finally, Section 5 summarizes the conclusions.

2. Mathematical modelling

Eulerian-Eulerian and Eulerian-Lagrangian models are often employed when simulating dispersed two-phase flows [21]. Eulerian-Eulerian models treat all phases, including particles or particle bundles, as continuous phases and their momentum and continuity equations are solved for each phase [21]. This approach greatly saves computational cost but cannot provide information of any specific particle or particle bundle [21]. Different from Eulerian-Eulerian models, Eulerian-Lagrangian models treat only the fluid phase as continuous phase but the particle is treated as discrete phase [22]. As a result, an Eulerian-Lagrangian approach is chosen in this study in order to investigate particle behavior on both collective and individual levels. When Eulerian-Lagrangian models are applied, one important aspect that should be considered is the coupling between the continuous phase and the dispersed phase, namely one-way, two-way or four-way coupling; one-way coupling only accounts for the influence of the fluid on the particles, but neglects the particles influence on the fluid and intra-particle interactions; two-way coupling considers the interactions between the fluid and the particles, but neglects the intra-particle interactions; four-way coupling includes interactions between the particles and the fluid, as well as intra-particle interactions [23]. The method of coupling in the present work is explained in Section 2.4. Below outlines the theory of particle models accounting for the drag force and torque used in this work. It should be noted that only drag and buoyant (including gravity) forces that act on the particles are considered in this work. Other forces such as virtual mass force are neglected as they are not important under conditions of interest where particles are relatively small and particle to fluid density is large [23].

2.1. The sphere model

Various drag models are available in open literature, for example the distorted sphere drag model by Liu et al. [24]. Here, the following sphere drag model (originally implemented in OpenFOAM [20] 4.x "SphereDragForce.C", based on [23] with modifications) is used as an example to represent the common practice that pulverized biomass particles are simulated as spheres in CFD.

In this particle drag model, the drag force is defined as,

$$F_D = \frac{\frac{3}{4} m_p \mu_f C_D (U_f - U_p)}{\rho_f D_p^2} \tag{1}$$

$$C_D = \begin{cases} 0.424 Re_p, Re_p < 1000 \\ 24\left(1 + \frac{1}{6} Re_p^{\frac{2}{3}}\right), Re_p \geq 1000 \end{cases} \tag{2}$$

$$Re_p = \frac{|u_f - u_p|\, D_p}{\nu_f} \tag{3}$$

where F_D is particle drag force [N], m_p is particle mass [kg], μ_f is fluid dynamic viscosity [N·s/m^2], C_D is drag force coefficient, U_f is fluid velocity [m/s], U_p is particle velocity [m/s], ρ_f is fluid density [kg/ m^3], D_p is particle diameter [m], Re_p is particle Reynolds number and ν_f is fluid kinematic viscosity [m^2/s]. Note that the torque acting on the spherical particle is not calculated, so the rotation of particle is not considered.

2.2. The simplified non-sphere model

As previously stated, one of the most commonly used model that takes account the shape of a particle is the simplified non-sphere model developed by Haider and Levenspiel [11]. This simplified non-sphere model introduces a so-called shape factor (particle sphericity) to differentiate particle shapes, which is defined as the ratio of surface area of a sphere of equivalent volume to surface area of the non-spherical particle. Four model coefficients B_1, B_2, B_3 and B_4 are calculated based on this particle sphericity. The drag force coefficient then is formulated as:

$$C_D = \frac{24}{Re_p}(1 + B_1 \bullet Re^{B_2}) + \frac{Re_p \bullet B_3}{Re_p + B_4} \tag{4}$$

Although this model accounts for particle shapes, it still does not consider the orientations of the particle.

2.3. Spheroid model

In analytical geometry, a spheroid at origin point aligned along the coordinates can be described by

$$\frac{x^2}{a^2} + \frac{y^2}{a^2} + \frac{z^2}{c^2} = 1 \tag{5}$$

The aspect ratio is defined as $\lambda = \frac{c}{a}$ and a and c are the particle axial lengths [m]. A spheroid is referred to as a prolate ellipsoid when its aspect ratio is larger than one and an oblate ellipsoid when its aspect ratio is less than one. When its aspect ratio equals to one, it regresses to a sphere. In this work, the term spheroid is used to referred to a prolate ellipsoid specifically. This correlates to the fact that pulverized biomass particles are usually needle-like and have large aspect ratios [3].

When particles are non-spherical, it is of importance to include the particle rotation effects. Therefore, using an appropriate method to describe rotation in three-dimensional space is necessary. Three different Cartesian coordination frames in combination with an Euler rotation theorem are routinely used in previous studies for ellipsoid particles [25–27]. The three Cartesian frames are given as follows; $\boldsymbol{x} = (x_1, x_2, x_3)$ is the inertial frame, $\boldsymbol{x}^{'} = (x_1^{'}, x_2^{'}, x_3^{'})$ is the particle frame with its origin at the particle center and its principal axes being the spheroid particle's principle axes. In addition, the co-moving frame, $\boldsymbol{x}^{''} = (x_1^{''}, x_2^{''}, x_3^{''})$, represents the frame whose origin is at the particle center but its axes are parallel to its corresponding axes of the inertial frame.

According to Euler's rotation theorem, any rotation in a three-dimensional space can be defined by three angles, referred as Euler's angles. One set of three Euler's angles corresponds to one set of four Euler parameters, (e_0, e_1, e_2, e_3), and vice versa [28]. The transformation matrix, $\boldsymbol{A}$, that can convert between co-moving frame and particle frame is [29] given by:

$$\boldsymbol{x}^{'} = \boldsymbol{A}\boldsymbol{x}^{''} \tag{6}$$

2.3.1. Drag force of spheroid

In this work, the drag model developed by Hölzer and Sommerfield [15] for spheroid particles is employed. Formulas for drag force and drag force coefficient are given as follows:

$$F_D = \frac{1}{2} C_D \rho_f A_c (U_f - U_p)|U_f - U_p| \tag{7}$$

$$C_D = \frac{8}{Re_p}\frac{1}{\sqrt{\phi_{\parallel}}} + \frac{16}{Re_p}\frac{1}{\sqrt{\phi}} + \frac{3}{\sqrt{Re_p}}\frac{1}{\phi^{\frac{3}{4}}} + 0.4240^{0.4(-\log\phi)^{0.2}}\frac{1}{\phi_{\perp}} \tag{8}$$

where A_C is particle cross-sectional area that is projected to the flow direction [m^2]. In addition, ϕ, $\phi_{\parallel}$ and $\phi_{\perp}$ represent sphericity, lengthwise sphericity and crosswise sphericity, respectively. They account for different particle shapes and orientations. Their detailed definitions can be found in the original reference [15]. The model is implemented in a way that includes sideward motion due to particle major axis being inclined to flow direction (also known as "profile lift" in Mandø and

Rosendahl [30]). Particle drag forces are calculated separately in the *x*-, *y*- and *z*-direction in particle frame then are assembled together as vectors in inertia frame, by that particle drag coefficients are calculated separately in the *x*-, *y*- and *z*-direction in particle frame according to Eq. (8). As a result, the directions of assembled drag force vectors in inertia frame could be different from particle-to-fluid slip velocities. It should be noted that Hölzer and Sommerfield [15] states that this formula considers particle orientations over the entire range of Reynolds numbers up to the critical Reynolds number, whose precise definition is not given in their paper. The model has therefore some shortcomings at certain high Reynolds conditions, which however will not be relevant in the present study.

2.3.2. Torque of spheroid

Particle rotations are governed by [26]:

$$I_{ij}^{'}\frac{d\omega_j^{'}}{dt} - \varepsilon_{ijk}\omega_j^{'}I_{kl}^{'}\omega_l^{'} = N_i^{'} \tag{9}$$

where I is particle moment of inertia [kg·m^2], ω is particle angular velocity [rad/s], t is time [s], N is particle torque [N·m], superscript $^{'}$ refers to the aforementioned frame $\boldsymbol{x}^{'}$, ε is the Levi-Civita symbol and subscript i, j, k refer to tensor notation indices.

There are different ways to model particle torques. For example, two types of torques were considered in the work of Mandø and Rosendahl [30]. The first one is due to resistance and the second one is to offset the pressure center in relation to the geometry center of the particle. Both types of torques are coupled with particle forces in their work. In the present work, an alternative approach is used where particle torques are decoupled from particle forces and it is assumed that the particle geometry center is the pressure center. As a result, torque formulas that can predict particle rotation to a satisfactory extent but coupling with particle forces are required.

In this research, particle torques are calculated using formulas developed by Jeffery [31], which are decoupled from particle forces for an ellipsoid in creeping flow (i.e. $Re_p < 1$) [32]:

$$N_x^{'} = \frac{16\pi\mu a^3\lambda}{3(\beta_0 + \lambda^2\gamma_0)}[(1-\lambda^2)d_{zy}^{'} + (1+\lambda^2)(w_{zy}^{'} - \omega_x^{'})] \tag{10}$$

$$N_y^{'} = \frac{16\pi\mu a^3\lambda}{3(\alpha_0 + \lambda^2\gamma_0)}[(\lambda^2-1)d_{xz}^{'} + (1+\lambda^2)(w_{xz}^{'} - \omega_y^{'})] \tag{11}$$

$$N_z^{'} = \frac{32\pi\mu a^3\lambda}{3(\alpha_0 + \lambda^2\beta_0)}(w_{yx}^{'} - \omega_z^{'}) \tag{12}$$

where strain rate [s^{-1}] is

$$d_{ij}^{'} = \frac{1}{2}\left(\frac{\partial U_i^{'}}{\partial x_j^{'}} + \frac{\partial U_j^{'}}{\partial x_i^{'}}\right) \tag{13}$$

fluid rotation tensor [s^{-1}] is

$$w_{ij}^{'} = \frac{1}{2}\left(\frac{\partial U_i^{'}}{\partial x_j^{'}} - \frac{\partial U_j^{'}}{\partial x_i^{'}}\right) \tag{14}$$

and α_o, β_o and γ_o are dimensionless parameters given by Gallily and Cohen [33]:

$$\alpha_0 = \beta_0 = \frac{2\lambda^2(\lambda^2-1)^{\frac{1}{2}} + \lambda\ln\left[\frac{\lambda-(\lambda^2-1)^{\frac{1}{2}}}{\lambda+(\lambda^2-1)^{\frac{1}{2}}}\right]}{2(\lambda^2-1)^{\frac{3}{2}}} \tag{15}$$

$$\gamma_0 = \frac{2(\lambda^2-1)^{\frac{1}{2}} + \lambda\ln\left[\frac{\lambda-(\lambda^2-1)^{\frac{1}{2}}}{\lambda+(\lambda^2-1)^{\frac{1}{2}}}\right]}{(\lambda^2-1)^{\frac{3}{2}}} \tag{16}$$

The temporal evolution of the Euler's parameters can be calculated as follows [25]:

$$\frac{de_0}{dt} = \frac{1}{2}(-e_1\omega_x^{'} - e_2\omega_y^{'} - e_3\omega_z^{'}) \tag{17}$$

$$\frac{de_1}{dt} = \frac{1}{2}(e_0\omega_x^{'} - e_3\omega_y^{'} + e_2\omega_z^{'}) \tag{18}$$

$$\frac{de_2}{dt} = \frac{1}{2}(e_3\omega_x^{'} + e_0\omega_y^{'} - e_1\omega_z^{'}) \tag{19}$$

$$\frac{de_3}{dt} = \frac{1}{2}(-e_2\omega_x^{'} + e_1\omega_y^{'} + e_0\omega_z^{'}) \tag{20}$$

2.4. Computational methodology

The solver is developed using OpenFOAM 4.1, an open-sourced CFD platform, hereby referred to as the NELLI solver [22]. The Euler numerical scheme (transient, first order implicit and bounded) is used for time derivative terms. The standard finite volume discretization of Gaussian integration with linear interpolation (with minor modifications) is used for gradient terms, divergence terms and Laplacian terms. Linear interpolation is applied for the interpolation schemes. Surface normal gradient schemes are solved by corrected central differencing schemes. The standard *k-epsilon* model is employed to simulate the flow fields. Coupling between particles and the fluid are achieved through source terms as described in previous work [22]. Particle drag forces are two-way coupled unless otherwise stated, particle torques are only one-way coupled. Particles are initialized and injected into the flow field. The spheroid model is programmed as follows and illustrated in Fig. 1:

- Fluid velocities at particle locations are interpolated from values of cell centers that are calculated by the Eulerian flow solver.
- Particle Euler's parameters and transformation matrix are calculated based on particle angular velocities and orientations (i.e. four Euler parameters).
- Particle drag forces are calculated based on fluid and particle velocities and transformation matrix. As a result, particle velocities are updated.
- Particle torques are calculated based on fluid velocity gradients and transformation matrix. Particle orientations are updated accordingly.

3. Model verifications and validations

The verifications and validations of the spheroid model are divided into two parts (torque and drag) to ensure the correct implantation and the validity of the spheroid model.

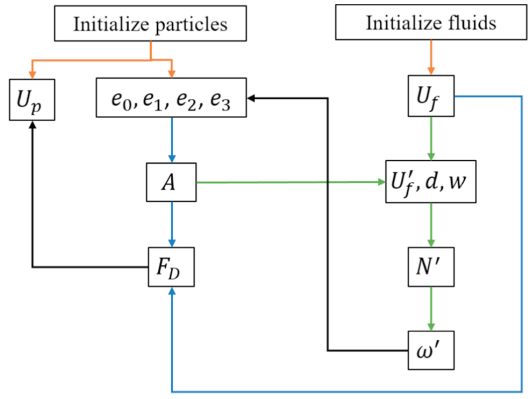

Fig. 1. Algorithm illustration of the spheroid model.

Table 1
Particle and fluid properties for model verification of torque.

	Unit	Value
Particle aspect ratio	–	10
Particle radius of minor axis	m	0.001
Particle Stokes number (defined in [42])	–	10
Density ratio of particle to fluid	–	1000
Kinematic viscosity of fluid	m^2/s	0.1

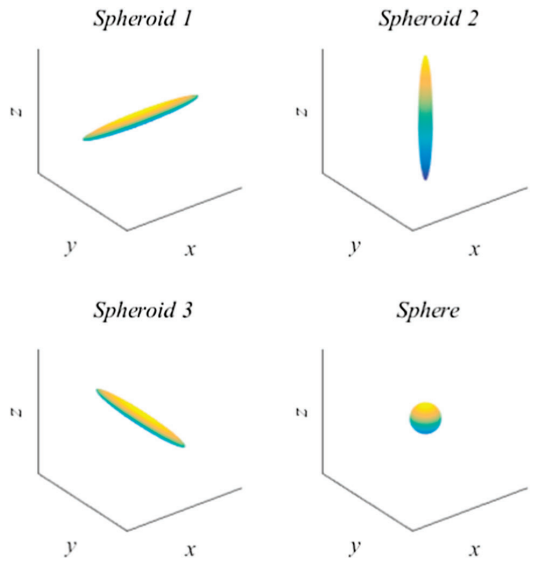

Fig. 2. Initial orientations of the particle in inertial frame.

3.1. Torque

Investigation of the torque implementation of the spheroid model is conducted by comparing with simulation results obtained from DNS by Zhao et al. [34]. In both simulations, a single spheroidal particle is placed in a simple shear flow in the *xz*-plane where the velocity gradient $\frac{du_x}{dz}$ is set to be $1\ s^{-1}$. The position of the particle is fixed, but the particle can rotate freely. This configuration is deliberately chosen to avoid additional effects of particle drag force. Other properties of the particle and the flow field are listed in Table 1. Kinematic viscosity of the fluid is arbitrary set to $0.1\ m^2/s$ for comparison.

As the spheroidal particle is not centrally symmetrical, initial orientation of the spheroidal particle can play a role in particle orientation evolutions. Therefore, three different particles that are configured with three different initial orientations are simulated. Their corresponding orientations in the inertial frame are illustrated in Fig. 2. As shown in Fig. 2, the major axes of *Spheroid 1*, *2* and *3* are parallel to the *x*-, *z*-, and *y*-direction of the inertial frame, respectively. It should be noted that the color in Fig. 2 is to make the three-dimensional particles visually friendly in a two-dimensional print.

Torque acting on the particle is dependent on fluid strain rate and rotation tensor, which are functions of velocity gradients. Because particle angular velocities are directly coupled to particle torque, the torque of the spheroid model can be verified by investigating the particle angular velocity for different orientations. The temporal evolutions of particle angular velocities in particle frame of *Spheroid 1* and *2* are presented in Fig. 3(a) and (b), respectively. In Fig. 3, the legend "DNS" represents that simulations are solved by direct numerical simulations (DNS) [34], whereas, the legend "NELLI" refers to that simulations are solved by the spheroid model with the aforementioned in-house solver NELLI [22]. In addition, *x*, *y* and *z* represent the component of the angular velocities in *x*-, *y*- and *z*-direction of particle frame, respectively. In the case of Fig. 3(a), the major axis of *Spheroid 1* is parallel to the *xz*-plane where velocity gradient exists, this makes the major axis of spheroidal particle easy to rotate around the *y*-direction. In addition, since $\frac{du_x}{dz}$ is the only existing velocity gradient, as the spheroidal particle rotates, particle torque reaches its highest value when the spheroidal particle's major axis is parallel to *z*-direction and lowest when the spheroidal particle's major axis is parallel to *x*-direction. Therefore, it can be expected that particle angular velocities in *x*- and *z*-direction in the particle frame are close to zero, but periodic fluctuations of particle angular velocities of *y*-direction in particle frame exist. Similar trends can be seen in the case of *Spheroid 2* (Fig. 3(b)) but showing periodic fluctuations in *x*-direction. In the case of *Spheroid 3*, the major axis of spheroidal particle is perpendicular to the *xz*-plane, this makes the particle easy to rotate around the particle major axis at constant speed. As a result, particle angular velocities of *x*-, *y*- and *z*-direction in particle frame remain constant around 0, 0, and 0.5 rad/s, respectively. In all cases, excellent agreement is achieved between results solved by DNS and the solver developed with the spheroid model thereby verifying the correct implementation of the particle torque.

The torque formulas used above are originally developed for an ellipsoid in creeping flows (i.e. $Re_p < 1$) [32], however the validity of the model in turbulent flow has been proven by Ravik et al. [35]. In their study, DNS simulations were conducted to assess the elongated particle torque under turbulent conditions. Only an approximately four percent root mean square (rms) error associated with Jeffery torques was found under the condition where Stokes number is 1 and ratio of particle length to Kolmogorov scale is 1. They also showed that the error decreases as particle inertia increase, but the error increases exponentially as the ratio of particle length to Kolmogorov scale increases to 8. The error exhibits a plateau trend for particles with even longer length. Therefore, we would assume that it is acceptable to apply these torque formulas into CFD simulations of entrained flow gasification process of pulverized biomass where the flow is turbulent.

3.2. Drag

To verify the implementation of particle drag and fluid-particle two-way coupling, test cases are configured based on the experimental work of Lau et al. [36], in which spherical particles (with less than 5% standard deviation) are injected via a jet flow into a wind tunnel. As shown in Fig. 4, a semi-two-dimensional cyclic symmetric 1 m × 0.3 m domain (one layer of cell in *y*-direction) is used to closely mimic the experiment. The circumferential angle is 2° and the nozzle radius is 6.35 mm. The flow and particle properties are listed in Table 2.

The particle loading factor in the experiments is 0.4. It is in the range where interactions among particles can be ignored but interactions between particles and the fluid must be considered. In other words, it is within the regime where two-way coupling should be included in the simulations [36,37]. The particles in the experiments deviate less than 5% from spherical particles and hence the particles in the simulations are configured as spheroids with aspect ratio of 1.001. Thus particles in both experiments and simulations can be considered spherical, which in turn makes it reasonable to assume particle orientation effects are less pronounced due to the central symmetric characteristics of spheres.

Four simulation cases are carried out. Two of them are solved by employing the sphere model (as described in Section 2.1), whereas the other two are solved by employing the spheroid model (as described in Section 2.2). Normalized centerline velocity profiles (U_c/U_c, U_c is the centerline velocity and U_c is the centerline velocity at the $x/d = 0$) of the particles can be seen in Fig. 5, where simulations using one-way coupling method (a) and two-way coupling method (b) are shown.

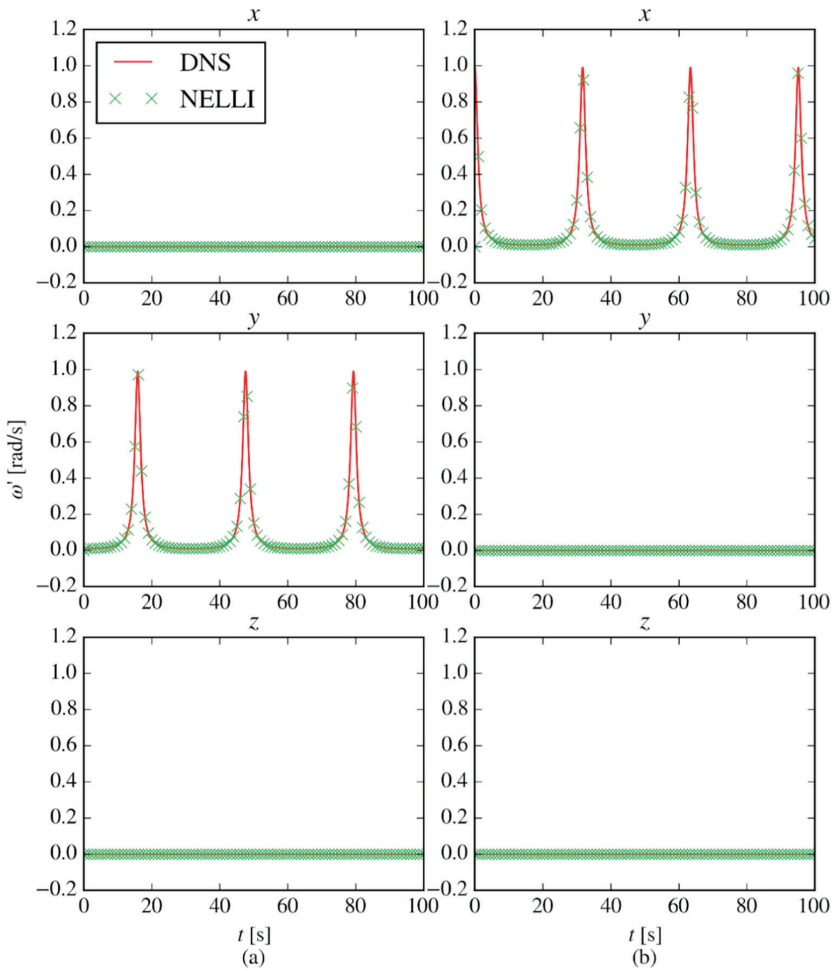

Fig. 3. Angular velocity profile of (a) *Spheroid 1* and (b) *Spheroid 2*. "DNS" and "NELLI" represent simulations are solved by the DNS [34] and the spheroid model with the aforementioned in-house solver NELLI [22], respectively; *x*, *y* and *z* represent the component of the angular velocities in *x*-, *y*- and *z*-direction of particle frame, respectively.

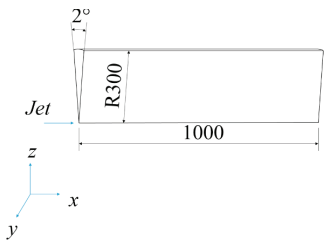

Fig. 4. Simulation domain of the particle-laden jet (unit: mm). The length of the domain is 1000 mm and the radius is 300 mm. Nozzle radius is 6.35 mm.

Additionally, experimental data from Lau et al. [36] is present as well. Due to rapid mixing as the flow develops, particle centerline velocity decreases as x/D_{jet} increases. It can be seen that there are good agreements between the sphere model and the spheroid model in both one-way and two-way coupled cases. This implies that the spheroid model can regress well to the sphere model. However, when comparing simulation results with experimental data, discrepancies are found in the one-way coupled cases while there are better matches in the two-way coupled cases. Normalized particle centerline velocities decay faster in the one-way coupled cases than the two-way couple cases and experiments. Particles have larger inertia than the fluid, hence the particle velocities decay slower than the fluid causing particle velocities to be higher than the fluid velocity in the beginning. In one-way coupled cases, the fluid is not accelerated by the particle. As a result, differences in velocity between the particle and the fluid in one-way coupled cases are larger than for the two-way coupled cases. This leads to larger drag forces acting on particles in the one-way coupled cases, thus causing faster normalized particle centerline velocity decays compared to the two-way coupled cases and the experiments. It can also be observed that there are no major differences when comparing experimental data and two-way coupled simulation results from the sphere model and the spheroid model, thus verifying the implemented particle drag model for spheroids.

The simulation results above also indicate the drag formula is applicable to spherical particles. To further test the validity of the drag formula, simulations are carried out to compare the drag force

Table 2
Particle and fluid properties for model verification of drag.

	Unit	Experiments by Lau et al. [36]	Simulation
Particle diameter	μm	20 (with standard deviation less than 5%)	$a = 20$, $c = 1.001a$
Particle mass loading factor	–	0.4	0.4
Jet exit diameter, D_{jet}	mm	12.7	12.7
Jet bulk velocity	m/s	12	12
Jet-to-co-flow velocity ratio	–	12	12
Stokes number (defined in [43])	–	1.4	1.4

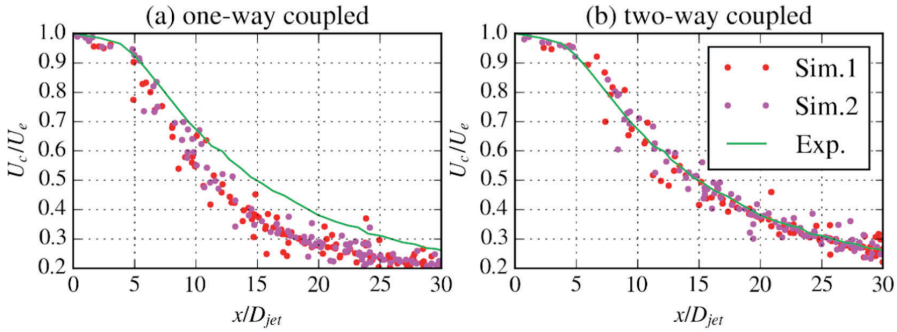

Fig. 5. Particle centerline velocity profile for one-way coupling (left) and two-way coupling (right). "Sim.1" and "Sim.2" stand for simulations employing spheres and spheroids with aspect ratio close to 1 respectively, "Exp." represents experiments.

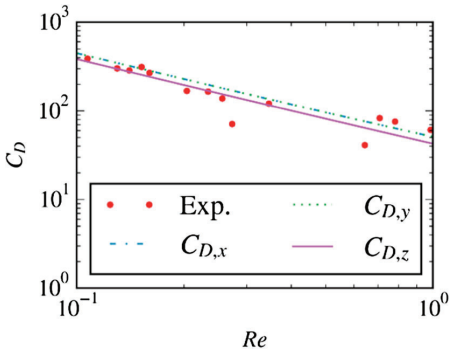

Fig. 6. Calculated drag coefficients for the three spatial directions compared to experimentally obtained drag force coefficient as function of Reynolds numbers.

coefficients from Madhav and Chhabra [38]. In their work, they conducted experiments of needle-shaped steel particle (particle density is 7484 kg/m^3, aspect ratio ranges from 27.35 to 39.53) free falling in tubes of silicone oil (density is 975 kg/m^3 and dynamic viscosity is 0.97 Pa·s) and they mapped drag coefficient-Reynolds number relations. We arbitrarily set up particle (with aspect ratio of 33.53) Reynolds numbers in the codes and compare particle drag coefficients calculated by the codes and data from Madhav and Chhabra [38]. The results are shown in Fig. 6, in which the label "Exp." represents experimental data extracted from Madhav and Chhabra [38], whereas, $C_{D,x}$, $C_{D,y}$ and $C_{D,z}$ are simulated particles drag coefficients produced by the spheroid model in the *x*-, *y*- and *z*-direction of particle frame, respectively. There are three drag force coefficients from the current study. This is due to how the spheroid model is implemented in the OpenFOAM platform. As previously mentioned in Section 2.3.1, particle drags are first calculated in the *x*-, *y*- and *z*-direction of particle frame separately, then converted to the format of vectors in the inertia frame. It can be seen from Fig. 6 that the simulated drag coefficients are close to the ones of experiments, thus validating the drag force formulas of the spheroid model. It also can be seen that $C_{D,x}$ and $C_{D,y}$ are the same, but they are different from $C_{D,z}$. This is because that the cross-sectional areas of spheroid particles in the *x*- and *y*-direction of particle frame are the same, but they are different from the ones in the *z*-direction.

4. Application to a simplified entrained flow gasifier

4.1. Simulation setup

The validated solver is employed to simulate particle-laden flows in a realistic gasifier configuration. Simonsson et al. [39] reported an atmospheric entrained flow gasifier experiment with stem wood and peat as fuels. A similar but somewhat simplified simulation setup is configured as seen in Fig. 7, where the simulation domain consists of two parts, i.e. a reactor and a burner inlet. The reactor is a cylinder with a length of 1 m and a diameter of 0.5 m. The burner inlet is also in cylinder shape with a length of 0.1 m. There are two air registers in the burner inlet. The primary air (orange part in Fig. 7), together with biomass fuels, is transported into the central cylinder tube of 50 mm diameter (hereafter referred as D). The secondary air is introduced via an annular pipe (blue part in Fig. 7, inner diameter 52 mm, outer diameter 56 mm) positioned outside the central tube.

Table 3 summarizes the fluid and particle properties. Operating parameters are set to that of the condition of wood swirl burner operated at equivalence ratio 0.5 [39]. Both swirl and non-swirl conditions are realized by varying the direction of the secondary air, particles are simulated as spherical particles and spheroidal particles with equivalent volume and aspect ratio of 10. In addition, spheroidal particles are injected with three initial orientations as *Spheroid 1*, *2* and *3* as shown in Fig. 2. These three orientations are evenly distributed and each of them makes up one third of the total particle mass flow. Three hexahedral meshes of 224,812, 425,790 and 748,512 cells have been used to test grid independence, respectively. The axial velocities of the fluid (without particles) at the centerline and various axial locations are compared. No significant difference between the latter two meshes is observed, but results from the first mesh are clearly different from the

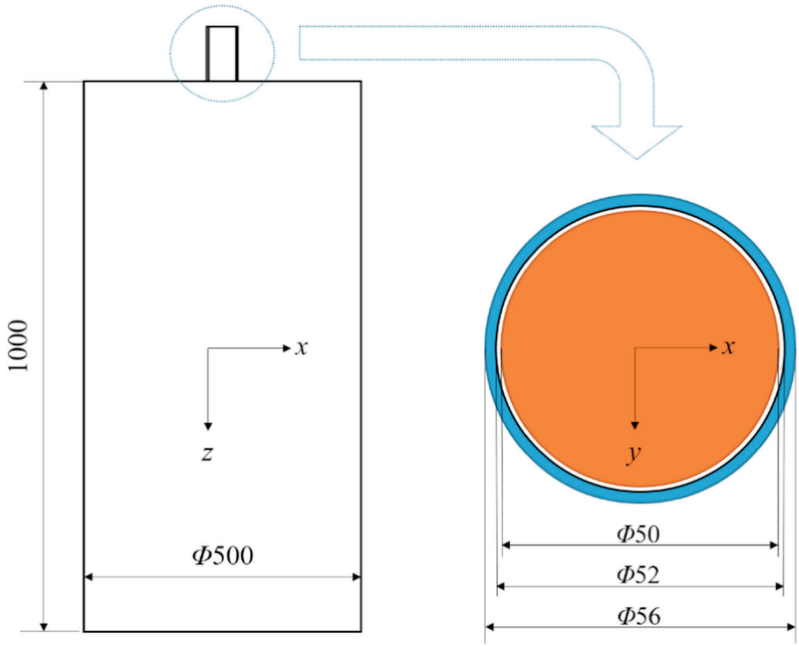

Fig. 7. Simulation domain of a simplified entrained flow reactor (Left: front view of the whole domain; right: inlet. Unit: mm).

Table 3
Simulation configurations for the simplified entrained flow reactor.

	Unit	Non-swirl	Swirl
Air density	kg/m^3	1.205	1.205
Primary air volume flow rate	L/min	535	535
Secondary air volume flow rate	L/min	410	410
Secondary air rotation speed	RPM	0	3172
Particle density	kg/m^3	650	650
Particle equivalent diameter	μm	250	250
Particle mass flow rate	kg/h	20.2	20.2

latter two. Therefore, the mesh of 425,790 cells (Fig. 8) is employed for further simulations. The time step for the simulation is 5×10^{-5} s. This work also uses "StochasticDispersionRAS" model from OpenFOAM 4.x for turbulent dispersion simulation, the model creates velocity perturbation randomly based on kinetic energy of turbulence and its general theory can be found in [40].

4.2. Results and discussions

In this subsection, simulation results are presented in the form of axial, radial, and tangential profiles at different axial locations, z/D, along the flow. Here, D refers to the diameter of inner tube, whereas r

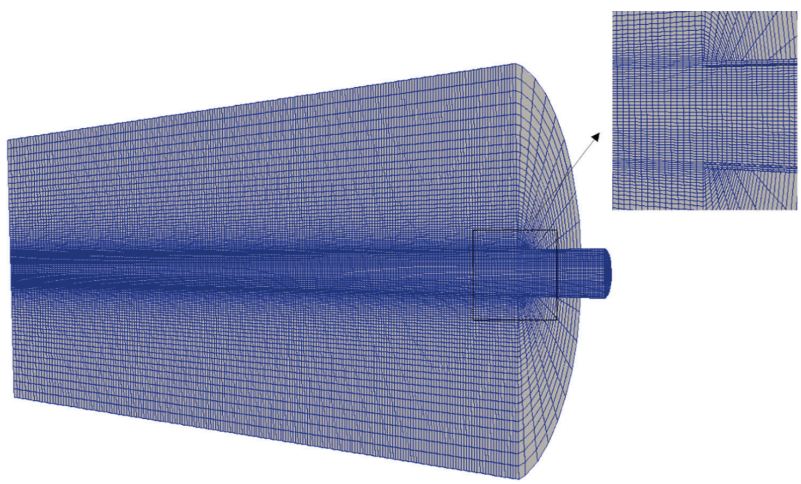

Fig. 8. Mesh of the simplified entrained flow gasifier.

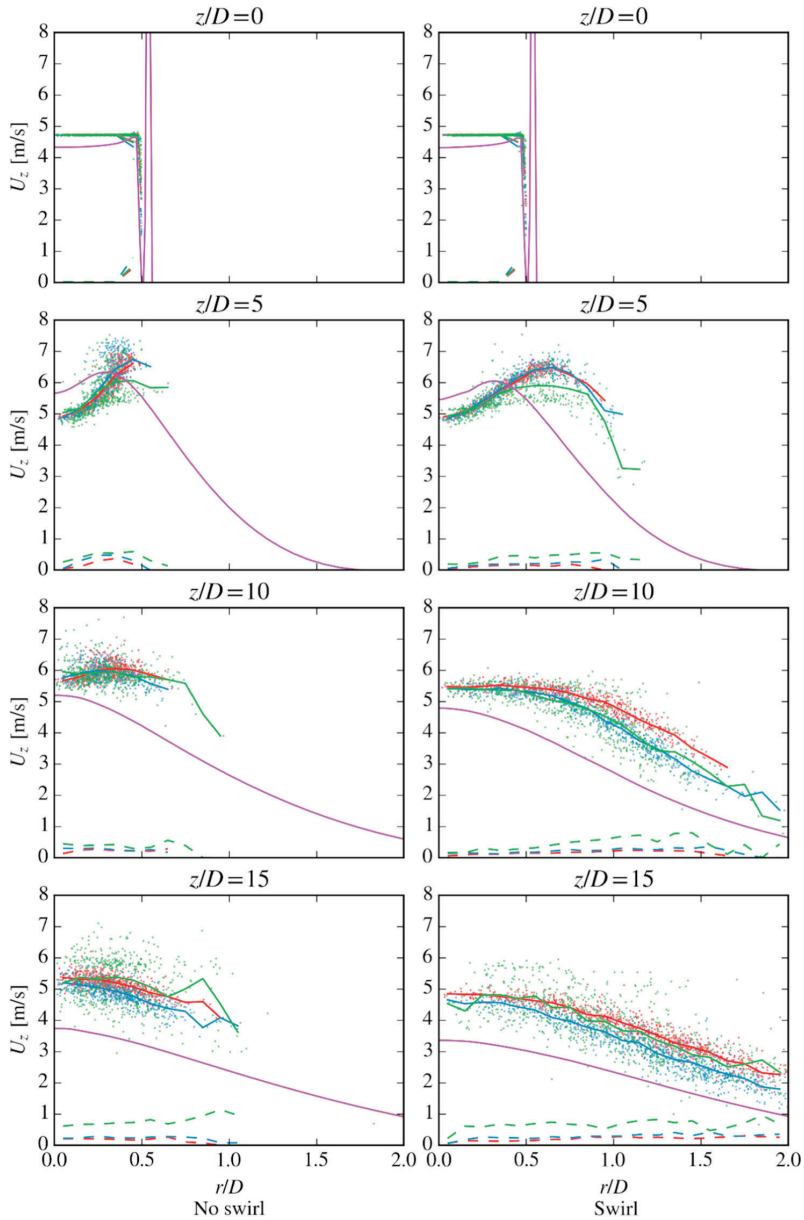

Fig. 9. Particle and fluid axial velocity distribution along reactor radius at different heights along the reactor (vertical) for non-swirl and swirl conditions (horizontal). Solid line: fluid or averaged particle velocity; dash line: standard deviation of particle velocity; scatter: particle velocity. Purple: fluid; red: the sphere model; blue: the simplified non-sphere model; green: the spheroid model. (For interpretation of the references to color in this figure legend, the reader is referred to the web version of this article.)

and τ refer to radial and tangential coordinates, respectively. The results calculated from different approaches under both swirl and non-swirl conditions are compared. Particle results presented below are sampled over 50 time steps to ensure there are sufficient number of particles so that results are statistically independent.

4.2.1. Axial velocity profile

Fig. 9 shows axial velocities of fluid and particles velocity along the reactor radius at different axial locations. In terms of fluid velocities in both swirl and non-swirl conditions, at the axial location of $z/D = 0$, the peaks of axial velocities can be observed around radial location of $r/D = 0.52–0.56$ where secondary air is injected. The axial location of $z/D = 0$ is where primary air and secondary air enter the reactor from their respective tubes. As the flow develops further downstream, primary air and secondary air start to mix. At axial location of $z/D = 5$, the locations of the peak of fluid axial velocity under both swirl conditions

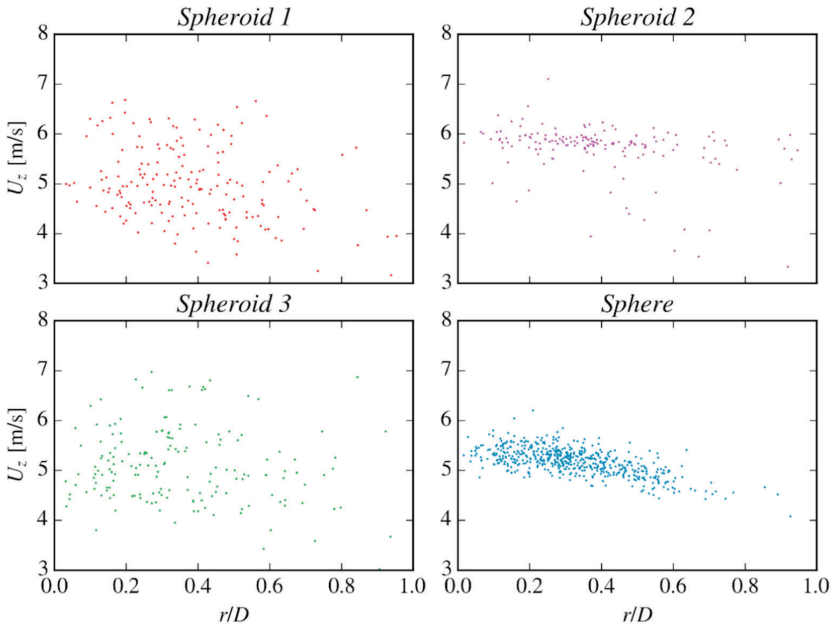

Fig. 10. Particle axial velocity distribution at $z/D = 15$ under non-swirl conditions. "Spheroid" means results are predicted by the spheroid model and "Sphere" means results are predicted by the sphere model, the number indicates the initial orientations of spheroidal particles as stated in Fig. 2.

move closer to the center in radial directions, instead of remaining around the radial location where secondary air is injected. The peaks disappear further downstream and overall axial velocities decrease at axial locations $z/D = 10$ and 15, where effects of secondary are much less prominent and the fluid momentum decays due to rapid mixing of primary air and secondary air.

Particles are injected with the exact same velocity as the primary air at the inlet ($z/D = -0.2$). Regardless of swirling conditions, particle axial velocities at the axial location of $z/D = 0$ only differs slightly from the fluid velocity in the radial region where r/D is less than 0.5. Particles, which have the same initial velocity as primary air, first accelerate ($z/D = 5$) and then slow down ($z/D = 10$ and 15) from upstream to downstream. It shows particles preserve similar trends when comparing to the fluid profiles, but with a time delay. This is expected as particles here have larger inertia than the fluid. When studying the differences at different swirling conditions, it can be observed that particles are distributed over a wider range of radial locations in swirl conditions than non-swirl conditions, due to the swirl of the fluid as it will be further explained in Section 4.2.2.

When comparing between the sphere model and the spheroid model, it can be seen from Fig. 9 that the spherical particles have a much narrower axial velocity distributions than the spheroidal particles, regardless of swirling conditions. The axial velocities of spherical particles concentrate in a narrow region and this pattern continues from upstream to downstream. However, the axial velocities of spheroidal particles become more divergent when they come downstream. A possible cause of such differences between spherical and spheroidal particles could come from initial orientations of spheroidal particle. Fig. 10 presents a more detailed overview of particle axial velocities at axial location of $z/D = 15$. For the simplicity, only the non-swirl conditions are shown. Particles of *Spheroid 1* and *Spheroid 3* have similar distribution patterns for axial velocity, ranging from 3 to 7 m/s, whereas particles of *Sphere* and *Spheroid 2* are narrowly distributed around 5 and 6 m/s, respectively. The major axes of *Spheroid 1* and *3* are perpendicular to the reactor axial direction, but is parallel in the case of *Spheroid 2*. Since large gradients of fluid axial velocity exist in radial directions due to the configuration of inlet conditions, particles of *Spheroid 1* and *Spheroid 3* are much easier to rotate than particles of *Spheroid 2*. As a result, the cross-sectional area of a *Spheroid 2* particle projected to the flow direction does not vary significantly from one particle to another and little differences between particle axial velocities and drag forces exist among particles of *Spheroid 2*.

Differences of averaged axial velocities of particles predicted by these three models can be observed from upstream to downstream. One factor that contributes to such differences could be how different models calculate particle projected cross-sectional areas to the flow when simulating particle drag forces. The sphere model treats pulverized biomass particles as spheres of equivalent volumes, this means the particle projected cross-sectional areas to the flow remain constant. The simplified non-sphere model use sphericity to compensate particle shape irregularities and thus making particle projected cross-sectional areas to the flow being different than the ones calculated by the sphere model. Although the simplified non-sphere model considers particles being non-spherical, the sphericity of a particle still remains constant as long as the shape of the particle does not change. This indicates particles of different orientations will have the same drag forces if other conditions are the same, which is not the case in reality. The spheroid model takes one step further by considering particle orientations by calculating particle torques and then modify particle drag forces. In this way, particles of different orientations will have different drag forces when other conditions are the same. Furthermore, values of standard derivation indicate how scattered (or dispersed) the particles are. The different ways modelling particles could also explain why the standard derivations of particle axial velocities predicted by the sphere model and the simplified non-sphere model are in closer agreement than the spheroid model as clearly seen in Fig. 9. Particles predicted by the spheroid model are more scattered from the other two models since the spheroid model considers particle orientations and one particle may have very different temporal development of orientations than another particle.

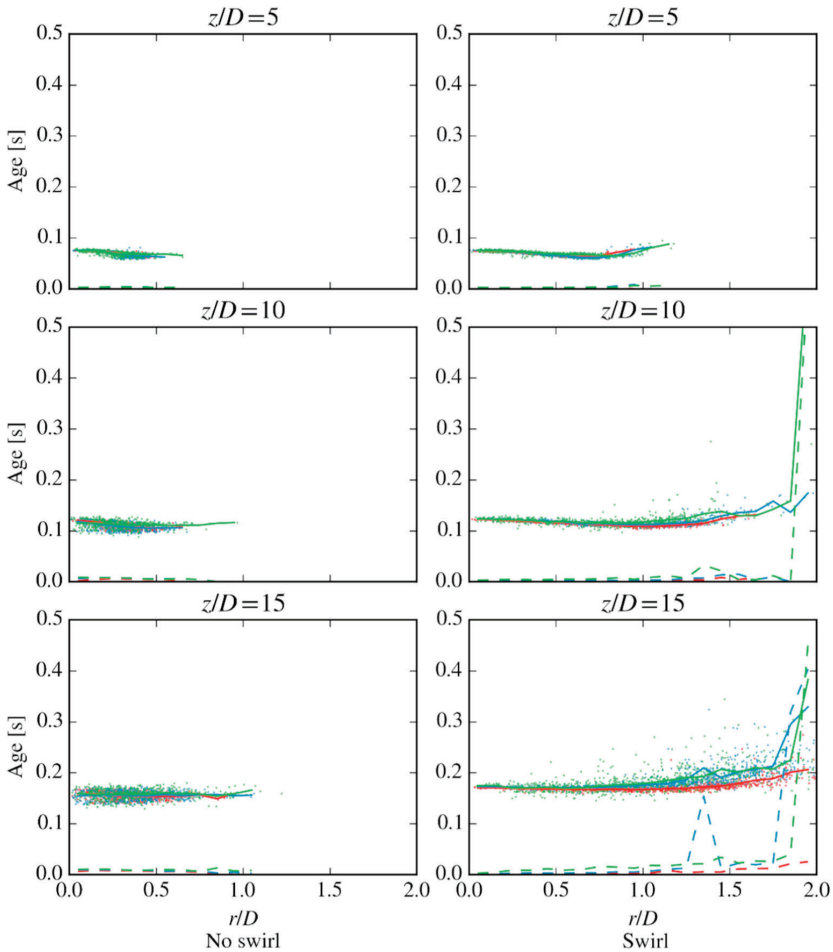

Fig. 11. Particle ages along reactor radius at different heights along the reactor (vertical) for non-swirl and swirl conditions (horizontal). Solid line: averaged particle age; dash line: standard deviation of particle age; scatter: particle age. Red: the sphere model; blue: the simplified non-sphere model; green: the spheroid model. (For interpretation of the references to color in this figure legend, the reader is referred to the web version of this article.)

The particle axial velocity is closely connected to particle residence time. In theory, particle residence time, t, over a certain distance, L, is dependent on particle velocity development along the distance, $U(L)$. This can be expressed by

$$t = \int \frac{dL}{U(L)} \tag{21}$$

Therefore, a higher axial velocity predicts a shorter residence time if other conditions are the same. Particle ages along the reactor radius at different axial locations and swirling conditions are shown in Fig. 11. Particle age refers to the time it takes for a particle to reach the position of the measurement from the inlet, thus can be used as an indicator for particle residence time. From upstream to downstream, particle age variations become bigger under both swirl and non-swirl conditions. This phenomenon is especially pronounced for spheroidal particles under swirl conditions. Given the same axial location, particle ages, due to the differences of axial velocities, are also different along radial directions. It can also be seen that particle ages vary more in the spheroid model than the sphere model, especially in swirl cases. This is in agreement with patterns observed on particle axial velocities.

4.2.2. Radial and tangential velocity profiles

Fig. 12 shows the particle and fluid radial velocity distribution along the reactor radius. The radial velocity, U_r, is defined as the velocity component that is perpendicular to axial direction and parallel to radial direction. In non-swirl cases, fluid radial velocities at axial location of $z/D = 0$ peak around the radial location where secondary air is injected. This is due to the mixing of primary air and secondary air in radial direction. Since the fluid has higher radial velocity than the particles, they are accelerated by the fluid in the radial direction. As the flow develops further downstream, fluid radial velocity decays rapidly due to fast mixing and remains small. However, particles have much higher inertia than fluid so their radial velocities still increase. When there are swirls in the flow field, despite the fact that the fluid has very similar radial velocity profile as in the non-swirl cases, particle radial velocities are different from non-swirl cases. At axial location of $z/D = 5$, particle radial velocities increase along the radius in the swirl cases whereas in the non-swirl cases velocities do not increase significant along the radius. When there are swirls in the flow fields, particles have tangential velocities because of the swirling of fluids. This creates the possibility for particles to have higher radial velocities. Particles must have enough centripetal forces to keep circular motions

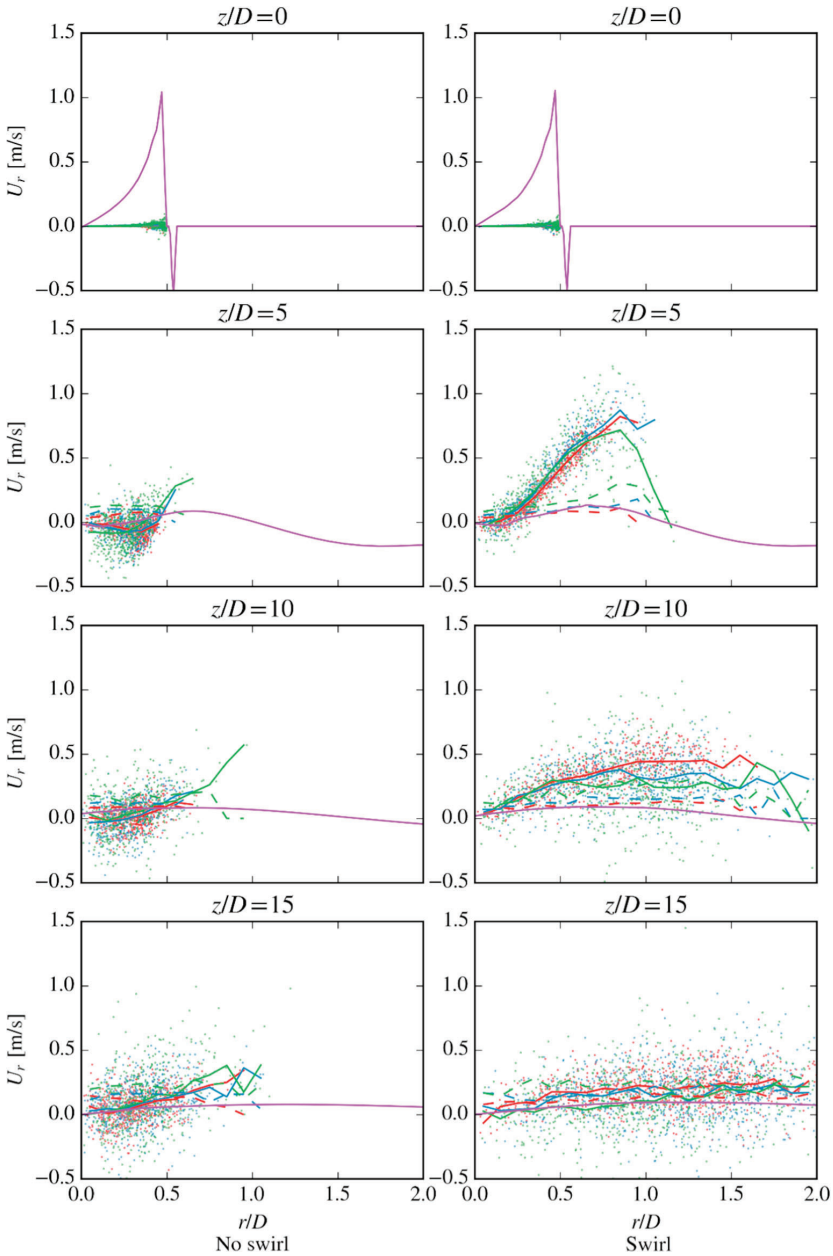

Fig. 12. Particle and fluid radial velocity distribution along reactor radius at different heights along the reactor (vertical) for non-swirl and swirl conditions (horizontal). Solid line: fluid or averaged particle velocity; dash line: standard deviation of particle velocity; scatter: particle velocity. Purple: fluid; red: the sphere model; blue: the simplified non-sphere model; green: the spheroid model. (For interpretation of the references to color in this figure legend, the reader is referred to the web version of this article.)

at certain radius, otherwise, particles have centrifugal motion, thus resulting velocities and displacements in radial directions. This is confirmed in Fig. 13, where the particle and fluid tangential velocity distribution along reactor radius is presented. Tangential velocity, U_t, is defined as the velocity component that is perpendicular to axial direction and radial direction. In Fig. 13, when there is no swirl, from upstream to downstream, fluid tangential velocity remains very small, particle tangential velocities on the other hand first start at 0 m/s then become dispersed to a range of ± 0.5 m/s. One possible cause for this could be the fact that dispersion model is applied in all simulations. The model creates velocity perturbation randomly, which gives particle tangential velocities. In swirl cases, fluid tangential velocities can clearly be observed. In the upstream of $z/D = 0$, fluids have the highest tangential velocities at the location where secondary air is injected into

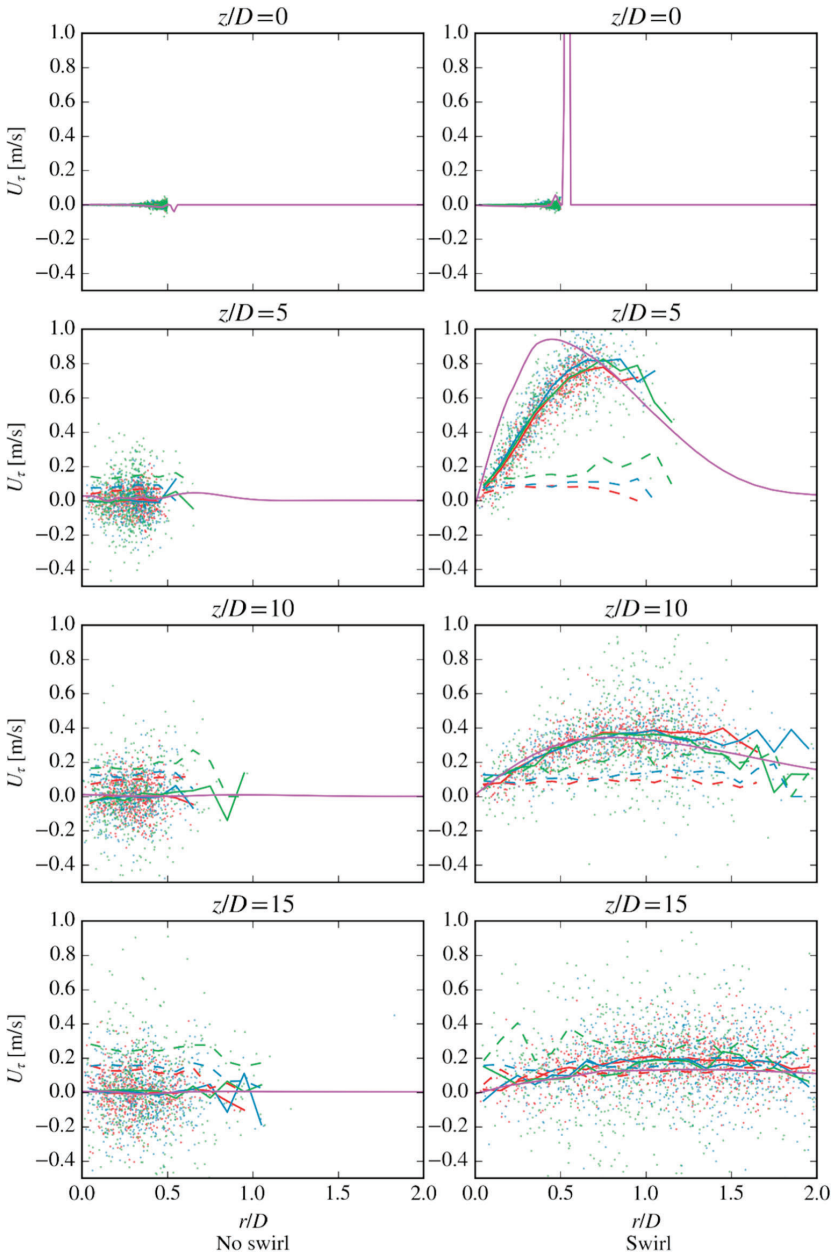

Fig. 13. Particle and fluid tangential velocity distribution along reactor radius at different heights along the reactor (vertical) for non-swirl and swirl conditions (horizontal). Solid line: fluid or averaged particle velocity; dash line: standard deviation of particle velocity; scatter: particle velocity. Purple: fluid; red: the sphere model; blue: the simplified non-sphere model; green: the spheroid model. (For interpretation of the references to color in this figure legend, the reader is referred to the web version of this article.)

the reactor, as the flow develops to axial locations of z/D = 5, 10 and 15, fluid tangential velocities decay due to rapid mixing of primary and secondary air. Particles tangential velocities, on the other hand, remain concentrated around the vicinity of 0 m/s at the axial location of z/D = 0, then becomes accelerated by the fluid at z/D = 5, then decay further downstream at z/D = 10 and 15. The slower tangential velocity decays for particles compared to the fluid can be explained by the fact that particles have larger inertia than fluids. Regardless of swirl conditions, the spheroid model predicts larger standard deviations of radial and tangential velocities than the other two models. This trend is similar to what is observed in axial velocity profiles and could be explained in a similar way as stated in Section 4.2.1.

Fig. 14 shows particle concentrations at swirl conditions using the classical sphere model and the implemented spheroid model. A cross-

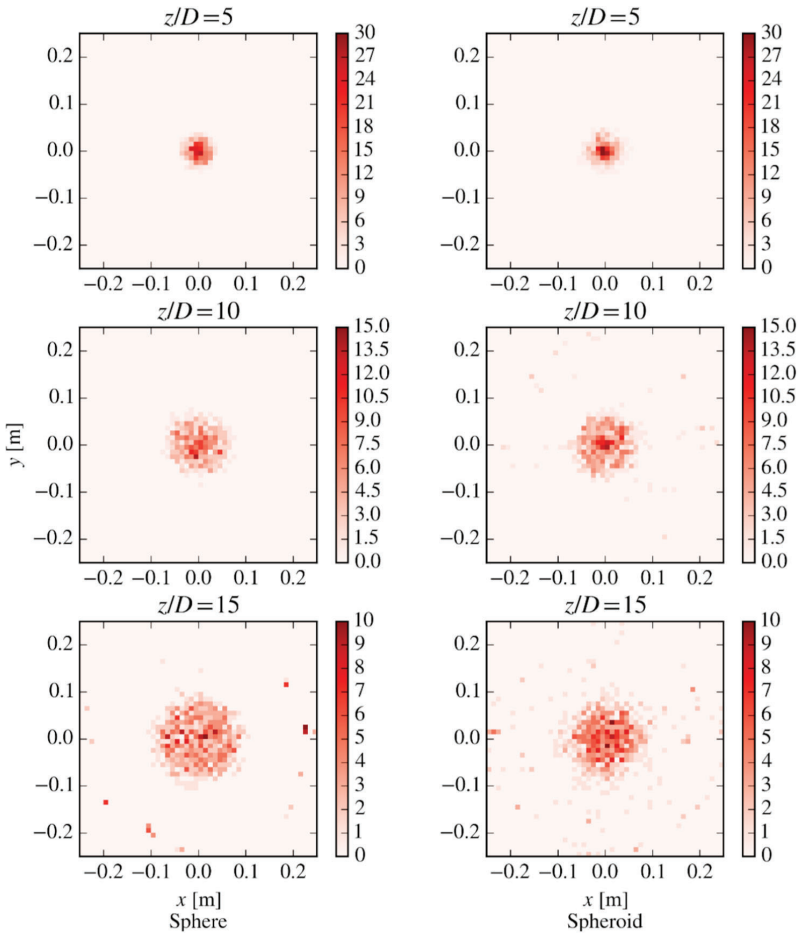

Fig. 14. Reactor cross-section indicating particle concentrations of swirl conditions at different heights along the reactor (vertical) for the spherical and spheroidal particles (horizontal). The color bar indicates the local concentration of particle i.e. number of particles per unit space, "sphere" and "spheroid" means they are predicted by the sphere model and the spheroid model, respectively.

sectional space of $z/D = \pm 0.05$ in axial direction is sampled at $z/D = 5$, 10 and 15, respectively. Then each cross-sectional space is evenly divided into 50 × 50 unit spaces in the *xy*-plane. The color bar indicates the local concentration of particle i.e. number of particles per unit space. In the upstream region ($z/D = 5$), both the sphere model and spheroid model give very similar results that particles are concentrated in the center. As the particles develop with the flow to further downstream, particles spread out. Many particles can be still observed around the center in the simulation using the sphere model further downstream ($z/D = 15$), whereas a more evenly distributed particle profile can be found in the results using spheroid model. This is in agreement with the aforementioned expectation that spheroidal particles are more dispersed and thus locally less concentrated.

4.2.3. Expected implications of model for non-spherical under reactive conditions

The observed phenomena in the cold flow simulation has also implications for the CFD simulations of biomass conversion using Eulerian-Lagrangian method. For example, when simulating the entrained flow gasification of biomass, where swirl conditions are typically expected, there can be significant differences between simulations using the sphere assumption and the spheroid assumption. Spheroidal particles have larger surface areas than spherical particles of the same volume. This makes heating up spheroidal particles easier than spherical particles in the same environment. A faster heating process could prompt the conversion of biomass particles, especially the endothermic drying process, and consequently using a spherical model approach may underestimate this. Furthermore, in an entrained flow gasifier, some volatile gases released from the fuel reacting with oxygen to provide heat for the gasification reactions. Reactants must be mixed on a microscale level and be present in the reactive mixture for a certain period of time in order to undergo thermal conversion [23]. In other words, local species concentrations and residence times are determining factors of the chemical reactions. As found in the cold flow simulation, spheroidal particles are clearly more dispersed than spherical particles under swirl conditions. Simulations using the spherical particle model may underpredict the mixing of volatile gases and oxygen, thus presumably leading to a slower combustion of volatile gases. Apart from gas phase reactions, the choice of sphere or spheroid model also affects gas-solid phase reactions. The traditional spherical particle model may produce more concentrated char clusters and thus resulting a slower conversion process. Similar analysis can also be conducted for the

simplified non-sphere model, as it predicts less scattered results in terms of particle velocities when compared to the spheroid model. However, it should be noted that in the later stage of the entrained flow gasification of biomass, as biomass particles react and convert, shapes of biomass particles become more and more spherical as evidenced in a previous study [5]. Particle size changes can affect the particle aspect ratio. It also may influence pulverized biomass particle size distribution in the flame as this is the case for coal [41]. Nevertheless, the overall implications of replacing spherical particle models with spheroid particle models are in need for further studies under reactive conditions, which is the next step of our research.

5. Conclusions

This work presents a detailed implementation of the spheroid particle model for simulating pulverized biomass particle. The spheroid particle model is implemented into an Eulerian-Lagrangian CFD solver in OpenFOAM and is verified and validated against DNS and experiments. Non-reactive test cases are executed to predict particle behaviors in a configuration similar to an entrained flow gasifier. When comparing to simulations by using the sphere model and the simplified non-sphere model, the spheroid model shows different results in terms of particle axial, radial and tangential velocities. Larger standard deviations of particle velocities are also observed in the case of the spheroid model. This could be caused by the fact that the spheroid model takes particle orientations into account while the other two models do not. Moreover, under swirling conditions, the spheroid model gives more diverse particle concentrations and residence times than the traditional sphere model. All the above indicates that using the spheroid model could have major influences on reactive simulation and this should be further investigated.

Acknowledgements

This work is a part of the GAFT project (Gasification and FT-Synthesis of Lignocellulosic Feedstocks; project number: 244069) and is also in partnership with Sino-Norwegian Partnership on Sustainable Energy (project number: 250146). Both of them are co-funded the Research Council of Norway and industrial partners. In addition, L. Zhao thanks the support of Nature Science Foundation of China through Grant No. 11702158, 91752205 and 11490551.

The authors would also like to express gratitude to Professor Helge I. Andersson for helping implement particle torque. We would also like to thank Mr. Fredrik Grøvdal for his mathematical support about spheroid sphericities. In addition, we acknowledge Dr. Niranjan Reddy Challabotla for his help in understanding torques of spheroid. At the time when this paper is written, all of the three researchers are affiliated with Department of Energy and Process Engineering, Norwegian University of Science and Technology, Norway.

References

[1] Ari I, Sari R. Differentiation of developed and developing countries for the Paris Agreement. Energy Strategy Rev 2017;18:175–82. https://doi.org/10.1016/j.esr.2017.09.016.
[2] Zwart RWR, Boerrigter H, van der Drift A. The impact of biomass pretreatment on the feasibility of overseas biomass conversion to Fischer-Tropsch products. Energy Fuels 2006;20:2192–7. https://doi.org/10.1021/ef060089f.
[3] Li T, Wang L, Ku X, Güell BM, Løvås T, Shaddix CR. Experimental and modeling study of the effect of torrefaction on the rapid devolatilization of biomass. Energy Fuels 2015. https://doi.org/10.1021/acs.energyfuels.5b00348.
[4] Gubba SR, Ma L, Pourkashanian M, Williams A. Influence of particle shape and internal thermal gradients of biomass particles on pulverised coal/biomass co-fired flames. Fuel Process Technol 2011;92:2185–95. https://doi.org/10.1016/j.fuproc.2011.07.003.
[5] Panahi A, Levendis YA, Vorobiev N, Schiemann M. Direct observations on the combustion characteristics of Miscanthus and Beechwood biomass including fusion and spherodization. Fuel Process Technol 2017;166:41–9. https://doi.org/10.1016/j.fuproc.2017.05.029.
[6] Gao X, Zhang Y, Li B, Yu X. Model development for biomass gasification in an entrained flow gasifier using intrinsic reaction rate submodel. Energy Convers Manage 2016;108:120–31. https://doi.org/10.1016/j.enconman.2015.10.070.
[7] Ku X, Jin H, Lin J. Comparison of gasification performances between raw and torrefied biomasses in an air-blown fluidized-bed gasifier. Chem Eng Sci 2017;168:235–49. https://doi.org/10.1016/j.ces.2017.04.050.
[8] Simone M, Biagini E, Galletti C, Tognotti L. Evaluation of global biomass devolatilization kinetics in a drop tube reactor with CFD aided experiments. Fuel 2009;88:1818–27. https://doi.org/10.1016/j.fuel.2009.04.032.
[9] Zhang W, Tainaka K, Ahn S, Watanabe H, Kitagawa T. Experimental and numerical investigation of effects of particle shape and size distribution on particles' dispersion in a coaxial jet flow. Adv Powder Technol 2018. https://doi.org/10.1016/j.apt.2018.06.008.
[10] van Wachem B, Zastawny M, Zhao F, Mallouppas G. Modelling of gas-solid turbulent channel flow with non-spherical particles with large Stokes numbers. Int J Multiphase Flow 2015;68:80–92. https://doi.org/10.1016/j.ijmultiphaseflow.2014.10.006.
[11] Haider A, Levenspiel O. Drag coefficient and terminal velocity of spherical and nonspherical particles. Powder Technol 1989;58:63–70. https://doi.org/10.1016/0032-5910(89)80008-7.
[12] Ma L, Jones JM, Pourkashanian M, Williams A. Modelling the combustion of pulverized biomass in an industrial combustion test furnace. Fuel 2007;86:1959–65. https://doi.org/10.1016/j.fuel.2006.12.019.
[13] Backreedy RI, Fletcher LM, Jones JM, Ma L, Pourkashanian M, Williams A. Co-firing pulverised coal and biomass: a modeling approach. Proc Combust Inst 2005;30(II):2955–64. https://doi.org/10.1016/j.proci.2004.08.085.
[14] Rosendahl L. Using a multi-parameter particle shape description to predict the motion of non-spherical particle shapes in swirling flow. Appl Math Model 2000;24:11–25. https://doi.org/10.1016/S0307-904X(99)00023-2.
[15] Hölzer A, Sommerfeld M. New simple correlation formula for the drag coefficient of non-spherical particles. vol. 184. 2008. doi:10.1016/j.powtec.2007.08.021.
[16] Schiemann M, Haarmann S, Vorobiev N. Char burning kinetics from imaging pyrometry: particle shape effects. Fuel 2014;134:53–62. https://doi.org/10.1016/j.fuel.2014.05.049.
[17] Vorobiev N, Becker A, Kruggel-Emden H, Panahi A, Levendis YA, Schiemann M. Particle shape and Stefan flow effects on the burning rate of torrefied biomass. Fuel 2017;210:107–20. https://doi.org/10.1016/j.fuel.2017.08.037.
[18] Grow DT. Mass and heat transfer to an ellipsoidal particle. Combust Flame 1990;80:209–13. https://doi.org/10.1016/0010-2180(90)90128-E.
[19] Li J, Zhang J. Analytical study on char combustion of spheroidal particles under forced convection. Powder Technol 2017;313:210–7. https://doi.org/10.1016/j.powtec.2017.02.054.
[20] The OpenFOAM Foundation. OpenFOAM n.d. https://openfoam.org (accessed May 25, 2018).
[21] Ku X, Li T, Løvås T. Influence of drag force correlations on periodic fluidization behavior in Eulerian-Lagrangian simulation of a bubbling fluidized bed. Chem Eng Sci 2013;95:94–106. https://doi.org/10.1016/j.ces.2013.03.038.
[22] Ku X, Li T, Løvås T. Eulerian-Lagrangian simulation of biomass gasification behavior in a high-temperature entrained-flow reactor. Energy Fuels 2014;28:5184–96. https://doi.org/10.1021/ef5010557.
[23] Andersson B, Andersson R, Håkansson L, Mortensen M, Sudiyo R, Van Wachem B. Computational fluid dynamics for engineers. 2011. doi:10.1017/CBO9781139093590.
[24] Liu AB, Mather D, Reitz RD. Modeling the effects of drop drag and breakup on fuel sprays. SAE Int Congr Expo 1993;298:1–6. https://doi.org/10.4271/93007.
[25] Marchioli C, Fantoni M, Soldati A. Orientation, distribution, and deposition of elongated, inertial fibers in turbulent channel flow. Phys Fluids 2010;22:033301https://doi.org/10.1063/1.3328874.
[26] Mortensen PH, Andersson HI, Gillissen JJJ, Boersma BJ. Dynamics of prolate ellipsoidal particles in a turbulent channel flow. Phys Fluids 2008;20:093302https://doi.org/10.1063/1.2975209.
[27] Zhang H, Ahmadi G, Fan F-G, McLaughlin JB. Ellipsoidal particles transport and deposition in turbulent channel flows. Int J Multiphase Flow 2001;27:971–1009. https://doi.org/10.1016/S0301-9322(00)00064-1.
[28] Spring KW. Euler parameters and the use of quaternion algebra in the manipulation of finite rotations: a review. Mech Mach Theory 1986;21:365–73. https://doi.org/10.1016/0094-114X(86)90084-4.
[29] Morton HS, Junkins JL, Blanton JN. Analytical solutions for Euler parameters. Celest Mech 1974;10:287–301. https://doi.org/10.1007/BF01586859.
[30] Mandø M, Rosendahl L. On the motion of non-spherical particles at high Reynolds number. Powder Technol 2010;202:1–13. https://doi.org/10.1016/j.powtec.2010.05.001.
[31] Jeffery GB. The motion of ellipsoidal particles immersed in a viscous fluid. Proc R Soc A Math Phys Eng Sci 1922;102:161–79. https://doi.org/10.1098/rspa.1922.0078.
[32] Andersson HI, Zhao L, Barri M. Torque-coupling and particle–turbulence interactions. J Fluid Mech 2012;696:319–29. https://doi.org/10.1017/jfm.2012.44.
[33] Gallily I, Cohen AH. On the orderly nature of the motion of nonspherical aerosol particles. II. Inertial collision between a spherical large droplet and an axially symmetrical elongated particle. J Colloid Interface Sci 1979. https://doi.org/10.1016/0021-9797(79)90287-X.
[34] Zhao L, Andersson HI. Why spheroids orient preferentially in near-wall turbulence. J Fluid Mech 2016;807:221–34. https://doi.org/10.1017/jfm.2016.619.
[35] Ravnik J, Marchioli C, Soldati A. Application limits of Jeffery's theory for elongated particle torques in turbulence: a DNS assessment. Acta Mech 2018. https://doi.org/10.1007/s00707-017-2002-5.
[36] Lau TCW, Nathan GJ. Influence of Stokes number on the velocity and concentration

distributions in particle-laden jets. J Fluid Mech 2014. https://doi.org/10.1017/jfm.2014.496.
[37] Elgobashi S. An updated classification map of particle-laden turbulent flows. In: Balachandar S, Prosperetti A, editors. IUTAM Symp. Comput. Approaches to Multiph. Flow. Dordrecht: Springer Netherlands; 2006. p. 3–10. doi:10.1007/1-4020-4977-3_1.
[38] Madhav GV, Chhabra RP. Drag on non-spherical particles in viscous fluids. Int J Miner Process 1995;43:15–29. https://doi.org/10.1016/0301-7516(94)00038-2.
[39] Simonsson J, Bladh H, Gullberg M, Pettersson E, Sepman A, Ögren Y, et al. Soot concentrations in an atmospheric entrained flow gasifier with variations in fuel and burner configuration studied using diode-laser extinction measurements. Energy Fuels 2016;30:2174–86. https://doi.org/10.1021/acs.energyfuels.5b02561.
[40] Gosman AD, Loannides E. Aspects of computer simulation of liquid-fueled combustors. J Energy 1983. https://doi.org/10.2514/3.62687.
[41] Muto M, Tanno K, Kurose R. A DNS study on effect of coal particle swelling due to devolatilization on pulverized coal jet flame. Fuel 2016;184:749–52. https://doi.org/10.1016/j.fuel.2016.07.070.
[42] Lundell F, Carlsson A. Heavy ellipsoids in creeping shear flow: transitions of the particle rotation rate and orbit shape. Phys Rev E 2010;81.
[43] Jebakumar AS, Abraham J. Comparison of the structure of computed and measured particle-laden jets for a wide range of Stokes numbers. Int J Heat Mass Transfer 2016;97:779–86. https://doi.org/10.1016/j.ijheatmasstransfer.2016.02.074.

Paper 2

Particle morphology, orientation and volume fraction of biomass particles with different aspect ratio in a jet flow during devolatilization

Llamas, Ángel David García; **Guo, Ning**; Li, Tian; Gebart, Rikard; Løvås, Terese; Umeki, Kentaro.

(Submitted to *Fuel*, currently under review)

Morphology and volume fraction of biomass particles in a jet flow during devolatilization

Ángel David García Llamas[1*], Ning Guo[2], Tian Li[2], Rikard Gebart[1], Terese Løvås[2], Kentaro Umeki[1]

[1]Energy Engineering, Division of Energy Science, Luleå University of Technology, Luleå, Sweden

[2]Department of Energy and Process Engineering, Faculty of Engineering, NTNU - Norwegian University of Science and Technology, Trondheim, Norway

*Corresponding author. Email: anggar@ltu.se; Tel: +46-722 192952

Abstract

Particle size, aspect ratio (AR, defined here as major over minor dimension), orientation and volume fraction have been measured for a stream of pulverized biomass particles undergoing devolatilization. Milling of raw biomass for thermochemical conversion yields elongated particles with high AR. Particle shape affects the heat and mass transfers and motion of particles within a jet, potentially shifting the particle group regimes. Therefore, the effects of carrier gas flow and fuel AR on the devolatilization behavior of biomass particles streams have been addressed experimentally. Two shapes of dried Norwegian Spruce have been used: one nearly equant (AR=1.8±0.64) and another elongated (AR=3.8±2.9), both derived from the same sieve size of 200–250 μm. Experiments were performed in a laboratory-scale flat-flame assisted laminar drop tube reactor, where similar mass flows of particles (10–16 g h^{-1}) were injected with two different flow rates of CO_2 to a high temperature flame zone (methane flame at O_2-to-fuel equivalence ratio of λ=0.63). Time and space-averaged measurements of particle morphology and velocity during conversion were obtained with 2D particle tracking velocimetry (PTV) together with image analysis. Carrier gas flow acted as thermal ballast, affecting the heating rate to the gas and particles. Heterogeneity in morphological changes was observed, and the behavior was affected by heating rate, particle shape and carrier gas flows.

This paper describes phenomena relevant for the understanding of biomass devolatilization under very fast heating rates, such as shrinking, transient swelling, spherodization and lateral migration, and relates them to differences in heating rate and particle shape.

Keywords: Biomass, Devolatilization, PTV, morphology, aspect ratio

1. Introduction

Biomass is a carbon neutral alternative to fossil fuels [1] and could achieve negative emission in combination with carbon capture. Second generation biofuel production via gasification and catalytic synthesis is also a promising technology [2,3,6]. In northern Europe, Norwegian spruce (*Picea Abies*) is the most common softwood cultivar, and its residues from the forestry and paper mill industry are available for thermochemical conversion. However, biomass has high volatile matter content and often encounters technical challenges related to tar formation during thermochemical conversion [4]. Therefore, the ideal technology for biomass gasification should provide means to reduce the tar problem. The solution can be achieved by operating at high temperatures (>1373 K) to promote tar reforming reactions. Entrained-flow biomass gasification (EFBG) meets the requirements of tar-free syngas for fuel reforming, and at the same time, it can be easily scaled up for energy conversion [5]. Since EFBG presents very short fuel residence times, complete fuel conversion is limited by the most unreactive products towards thermochemical conversion: soot and char, mainly formed during the devolatilization stage. Devolatilization is mainly heat-driven, and therefore the stability of a self-sustained EFBG relies on high gas temperatures and intense mixing close to the burner outlet. These can be affected by operational parameters (flow rates of fuel and gas) or fuel-related properties, such as the ash content or the size and shape of the particles.

In EFBG, particle size must be small enough to be pneumatically conveyed and thermally thin to minimize the conversion time. This is generally achieved by milling, which is energetically demanding for obtaining very small size fractions due to the fibrous nature of the feedstock [6]. Besides, wood tends to break in the direction of the fiber, resulting in particles with high aspect ratio (i.e. length-to-

width ratio) [7] and presents anisotropic thermal properties relative to the direction of the grain [8]. Consequently, the conversion rate during devolatilization in EFBG is almost inevitably affected by limitations in transport phenomena due to the size of the biomass particles. Particle shape also affects this limitation during biomass devolatilization. This was investigated by Lu et al. [9], who showed that equant or nearly spherical particles had a long conversion time compared to the more elongated (cylindrical) shapes with similar sphere-equivalent diameter. In addition, AR affects the motion of particles conveyed by gas, adding rotation as another degree of freedom to the particle motions, potentially affecting the external heat transfer rate to the particle [10]. Besides, rotating particles traversing areas with flow strain may encounter forces in other directions rather than the main particle trajectory [11]. This might cause dispersion, potentially shifting the local volume fraction to be from group particles regime to isolated particle regime.

During devolatilization, the advection of gas from the reacting particle is accompanied by simultaneous changes of phase (melting), volume, shape, and thermal properties [12]. Apparent density changes were studied by Holmgren et al. [13], who proposed a devolatilization model through volume loss for pinewood and a density loss model for straw particles, since the latter ones preserved their volume during conversion and the first ones shrank. In addition to shrinking, melting and spherodization are also common for low ash-content lignocellulosic biomass feedstocks [14,15], including a short swelling stage in some cases [16,17]. Although swelling is usually disregarded for the biomass devolatilization models contrary to coal [18], it could occur at high heating rate because swelling is directly linked to the reactive boiling and bubbling of the molten phase. All these complex transformations in particle morphology during conversion modify the apparent gasification rate [19] and the transport phenomena and particle motions. Considering these changes in computational fluid dynamics (CFD) simulations has proven useful to predict pyrolysis gas composition and particle conversion times more accurately [18]. However, despite the importance of fuel conversion in energy conversion applications, experimental *in-situ* measurements of particle morphology during fast devolatilization in drop tube reactors are rare.

Solid-to-fluid interaction effects must be considered when particle-laden flows become dense, adding another limitation to conversion. With a DNS (direct numerical simulation), Russo et al. [22] observed a significant delay in devolatilization of a pulverized biomass flow at particle volume fraction above 10^{-4} due to the decrease in local gas temperature with the presence of particles. The near burner zone in EFBG can contain a region with high particle volume fractions (or short distances among particles) due to low flow rates of gasifying agent. In fact, short distances among particles have been also related to increased soot yields in biomass gasification [23]. Particle shape can also play an important role in solid-fluid interactions, since elongated particles always have a higher volume than equant ones for the same minimum dimension. Thus, for the same mass flow rate, samples with different aspect ratios could have different particle number densities while having the same volume fraction. A knowledge gap still exists on the effect of particle aspect ratio on particle volume fractions and the consequence on devolatilization.

The objective of this study is to elucidate the effect of aspect ratio on the morphological changes experienced by spruce particles during devolatilization. *In-situ* experiments at different carrier gas flow provided information about the sensitivity of these changes to modifications in the operation parameters. Additional measurements of particle orientation and volume fraction help to understand the heat and mass transfer during conversion and provide validation data for the development of CFD models.

2. Methodology

2.1 Feedstock

The fuel used was Norwegian spruce (*Picea Abies*) supplied by Biomassateknologicentrum (Biomass technology center, BTC), in Umeå, Sweden. Fuel properties are shown in Table 1. The received particles were obtained using a large-scale hammer mill at BTC and sieved down to 200–250 µm with a sieve shaker (AS200, Retsch Technology). The particle size fraction was chosen to be well above the resolution of the imaging system, still having low internal heat transfer limitations. From this size

fraction, two fractions with different aspect ratios (AR), one equant and another elongated, were separated using a method similar to the one used by Lu et al. [9], and explained thereafter. The feedstock was dried in an oven at 105 °C overnight and kept in a drying cabinet before every experiment.

Table 1 here

Shape segregation was carried out by manually sieving small amounts of the initial size fraction (200–250 µm) with a 225 µm sieve to avoid skewing the distribution. By applying single short shakes on a homogeneously distributed thin bed of particles over the sieve, particles with greater fluidity (lower aspect ratio, or more spherical) fall first, leaving enough time between pulses to inspect the shape of the particles passing through and store them if necessary. These particles were collected until elongated fractions started to pass through, which was observed easily after every shake using a handheld lens and verified using an optical microscope, as shown in Figure 1. Size distribution of the segregated particles was measured using a dynamic image analysis method with CAMSIZER XT (Retsch Technology GmbH). Figure 2 shows the distributions of volume-based particle size and aspect ratio for elongated and equant particles. Particle sizes are distributing in the overlapping ranges. However, elongated particles have slightly larger particle diameter due to the separation method. The aspect ratios decrease along with the increment of the particle diameter while showing clear differences between two samples; the volume-averaged mean and standard deviation of aspect ratio were 3.8±2.9 for the elongated particles and 1.8±0.64 for the equant ones.

Figure 1 here

Figure 2 here

2.2 Experimental setups and procedures

Experiments have been performed in a laboratory-scale pulverized jet burner where heat was supplied using a McKenna flat flame burner as shown in Figure 3 and Figure 4. The experimental matrix consisted in 2x2 conditions for two fuel aspect ratios at two carrier gas flows. Measurements

consisted in high speed imaging of devolatilizing particles and image post-processing to obtain geometry and velocity information. Fuel-rich atmosphere around the jet was achieved with a $CH_4/CO_2/O_2$ premixed flame at an air-to-fuel equivalence ratio of 0.625. The flows of reactant gases were chosen to achieve a product composition similar to the one found in the near-burner zone of entrained-flow gasifiers and oxy-fuel burners [24,25], as shown in Table 2. The particles were injected in the reactor through a hole in the center of the burner along with a stream of CO_2. Biomass feeding rate was in the order of 10 $g \cdot h^{-1}$, calibrated with a precision balance before the experiments. Gas composition of the combustion mixture was measured using a 490 Micro GC (gas chromatography) from Agilent before feeding biomass particles.

Table 2 here

As can be seen in Figure 3, the reactor consists of a cylindrical vessel with four view ports perpendicular to each other. Gas and particles were injected to the reactor from the upper part and were extracted from below. All the walls are heated externally up to 500 °C using heating tapes and insulated by mineral fiber insulation (not represented in the schemes for simplicity, more data about the temperature of the walls can be found in the supplementary materials). The supporting flat flame surrounds the 7 mm diameter outlet where particles and carrier gas are injected in the reaction zone. The biomass feeder was in-house made, consisting of a modified syringe pump and a mechanical vibrator. Upstream from the burner outlet, particles and gas flow through 0.7 m of pipe measured between the level of the bed of particles in the feeder and the burner outlet. The feeder pipe is coaxial to the reactor vessel. The gas flow rates were regulated by mass flow rate controllers (EL-FLOW, Bronkhorst High-tech B.V.).

For conducting high speed imaging, a pulsed laser sheet was sent through two opposing windowpanes crossing the reactor's axis (Dual power 527nm Litron, NdYAG laser). Two cameras (SpeedSense VEO 410 from Dantec Dynamics), with their sensors placed at 420 mm from the laser

sheet, captured the scattered light from the particles within the laser sheet thickness. Both cameras were equipped with 100 mm macro lenses (Milvus 2/100M ZF2. from ZEISS) on a Scheimpflug system. The laser was aligned with the centerline by tuning the position of the laser source with a traverse system so that the light would always cross the exact center of the view ports. Laser sheet thickness was 2 mm. Fields of views (FOV) of the two cameras were 20x80 mm in width and length, as shown with colored areas in Figure 3. It should be noted that Camera 1 (perpendicular to the flow) does not have visual access of the burner outlet. Therefore, the Camera 2 was tilted 64° against the laser sheet to allow visual access to the burner outlet. A Scheimpflug mount system allows further tilting of the camera sensor to make the image focal plane parallel to the laser plane. A standard multi-level calibration target (parallel to the laser sheet and in contact with the thin wire) was used to convert the pixels into physical distance and to de-warp the images deformed by perspective (Camera 2), using a pinhole camera calibration model, as in [26]. The minimum spatial resolution was 53.9 μm per pixel for the camera 2 and 41.6 μm per pixel for the Camera 1. Images were recorded at 800 Hz with an exposure time of 625 μs in double frame mode, for the duration of 3.75 s. Both cameras were synchronized with the laser trigger using a synchronizer (BNC model 575 pulse/delay generator from Intelek), with a time between pulses of 395 μs and a pulse width of 150 ns. The experimental results presented in this publication only correspond to the data obtained from the Camera 2. Results from Camera 1 were used to corroborate the measurements from Camera 2 to eliminate the possible uncertainties in the de-warping process. Camera 1 appears in the drawings to remark the limitations of the FOV from the presence of the window frame, motivating the tilting of Camera 2

Figure 3 here

2.3 Data analysis

Dynamic Studio 6.8 from Dantec Dynamics was used to post-process the collected images. Afterwards, Matlab was used to collect the data delivered from Dynamic Studio 6.8. Before

submitting the images to any method for particle shape recognition or velocimetry, image processing was applied to de-warp the images to an orthogonal perspective and to eliminate the areas with dispersed incandescent signal from sub-micron particles (e.g. soot, PAH, inorganic elements), as summarized in Figure 4. The image processing method consisted of the following steps:

Step 1. De-warping raw images and rescaling them to a field of view (FOV) of 20x74 mm with 800x2960 pixels. De-warping is required since the camera is placed at an angle with respect to the reactor's axis and it is achieved using an image model fit for a pinhole camera extracted from the calibration images.

Step 2. Arithmetic averaging of all de-warped images. This generates an image with the average background grayscale level.

Step 3. Subtraction of the arithmetic mean (Step 2) from the de-warped images (Step 1) and thresholding to leave only the particles and the areas with dispersed incandescent signals.

Step 4. Creating a set of images containing only the areas with dispersed incandescent signals by blurring with an opening-closing-median filter.

Step 5. Extraction of the dispersed incandescent signals by subtraction of images obtained in Step 4 from images obtained in Step 3.

PTV (particle tracking velocimetry) and size and shape characterization methods were applied to the images obtained in Step 5, using Dynamic Studio 6.8 from Dantec Dynamics. PTV calculates particle velocity by solving the cross-correlation matrix of particle positions between two frames, estimating the position of the particle as the centroid of the pixel values. Thus, the velocity vectors are snapped to the instantaneous particle positions (Lagrangian approach). The main constraints for accuracy are particle detection and the mathematical method used for solving the cross-correlation problem, which is affected by overlaps, high displacements or out-of-plane movements. Therefore, for high particle densities and velocities, the solution is not trivial and could produce outliers. To minimize the uncertainty, the cross-correlation problem for each particle is only solved for a specific region around the particle (a square of 3.2 mm). The dimensions of this region were selected as 3-4 times of the

expected maximum displacement. Particle overlap is rare and not taken into account for the velocity correlation. Displacements perpendicular to the laser plane could take place, but the laser sheet is thick enough to allow the tolerance of movement, judging from the measured horizontal displacement. Size and shape characterization are done simultaneously to PTV for each particle detected. The software stores all the values of velocity and morphology detected for each frame, and Matlab is used to time-average and downscale the data to a regular grid of 1.82x1.82 mm. High accuracy in size and shape characterization was achieved. Additional information on the comparison between Camsizer and high speed camera measurements can be found in the supplementary material.

Figure 4 here.

2.5 Mass flow rate of particles

Obtaining a stable biomass feeding rate for laboratory-scale experiments is a challenging task due to particle bridging and low feeding rate. The feeding rate measured with a laboratory balance prior to the experiments is inevitably inaccurate for short durations resolved in this study. The balance has a resolution of 1 mg, which is too large to measure the weight of a single particle. Using a high precision balance with more significant digits does not solve this issue, because of their longer response time (2 seconds). The method used here calculates the approximate mass flow rate for every experiment as a product of the average mass per particle times the average particle number flux through the burner outlet area. The average mass of each particle was obtained from an approximation of volume from the particle sizing method, assuming constant density.

Figure 5 represents number and mass flow rates for all the experimental conditions. It can be noted that the mass flow rates of equant and elongated particles lay within the same order of magnitude, for a significantly different particle number flow rate. This is the result of elongated particles having a

much higher volume per particle than the equant ones. In addition, experiments at high carrier gas flow had on average a higher flow rate. This does not necessarily mean a correlation between carrier gas flow and feeding rate, especially in this case, since it does not comply with the physical principle of the feeding mechanism: feeding rate is determined by the decrease of the level of the bed of biomass particles within the syringe feeder. Therefore, we deem this dependency on carrier gas flow rate to be fortuitous, probably caused by the technical uncertainties in adjusting the feeding rate from one experiment to another.

Figure 5 here

3. Results and discussions

3.1 Influence of carrier gas and particle volume fraction on heating rate

Carrier gas flow rate affects the heating rate of the particles since it acts as thermal ballast. Increasing the (inert) carrier gas flow adds more mass to be heated up from room temperature, consequently decreasing the heat flux to the particles. Therefore, increasing the carrier gas flow rate decreases the heating rate of the particles. From equilibrium calculations of the premixed $CH_4/CO_2/O_2$ supporting flame (see Table 2), a decrease of 20 K in the overall temperature should be expected solely by doubling the amount of carrier gas. In practice, the Reynolds number is low and mixing is controlled by mass diffusion; thus, the gas temperature close to the burner outlet should be even lower than the one predicted by equilibrium calculations, causing a decrease in the heating rate of the particles. High volume fraction of particles can also decrease the temperature of the gas, and affect their temperature. This can alter greatly the devolatilization rate, since phase change (melting) and volatile yields are promoted by very fast heating rates.

In any case, higher heating rates should lead to faster devolatilization and thus a much earlier appearance of a dispersed cloud of incandescent matter (i.e. soot). To investigate the influence of the carrier gas flow on the heating rate, we have studied the time required for the maximum intensity of light from disperse incandescent matter and the volume fraction of particles for centerline grid squares. For the first study, we have averaged all the pixel values from images obtained from the Step 4 in Figure 4 with the interrogation windows size of 6X6 mm, which are aligned center to the centerline of the burner. Then, these curves were normalized to the maximum average intensity for each experimental condition. A space-time transform was applied to the distances from the burner outlet depending on the amount of carrier gas flow, using measurements of carrier gas velocity without particles (more information about gas velocity measurements and image processing can be found in the supplementary materials). The results from this study are portrayed in Figure 6, which represents the normalized intensity of light emitted from the dispersed incandescent matter versus the residence time of the gas. In this figure it is clear that the onset of incandescence from disperse volatile matter was faster for conditions at low carrier gas flow. The time taken to achieve maximum normalized intensity at high carrier gas flow (20 ms) was twice of that at low gas flow (40 ms). This will translate in a delay in devolatilization for the cases at high gas flow, which can be attributed to a combination of the amount of carrier gas and particle volume fraction.

Figure 6 here

Volume fractions were obtained for a rectangular grid of 1.82x7 mm to avoid misrepresenting them due to high inter-particle distances. Figure 7 represents volume fractions for grid squares at the centerline of the jet. All experimental conditions presented similar volume fractions close to the inlet, with locally very high volume fractions close to the centerline. The values were approaching the boundary where particles could begin to affect the temperature of the gas (volume fraction larger than 10^{-4}) [22]. Within this region, small differences in volume fraction could affect devolatilization significantly. The initial volume fractions are similar for low and high gas flows and slightly lower for

278 elongated particles than for equant particles. It can be seen that high carrier gas flows did not benefit
279 conversion, and particles traveled a longer distance to reach the same volume fractions as the cases
280 at low carrier gas flows. This could explain why the slope to reach maximum intensity of dispersed
281 incandescent matter is steeper for elongated particles at high gas flow when compared to equant
282 particles at high gas flow. In any case, the choice of carrier gas flow seems to delay devolatilization
283 more than the uncertainty in the biomass feeding rate, and consequently the particle volume
284 fraction.

285

286 **Figure 7 here**

287

288 ### 3.2 Particle velocimetry

289 Figure 8 shows the time-averaged absolute particle velocity downstream the burner outlet, for all
290 reaction conditions. Velocity values are time averages for all particles within grid squares at the same
291 axial distance from the burner outlet, representing average velocity for different parallel cross
292 sections of the jet. As expected, experiments at low carrier gas flows exhibited slightly lower particle
293 velocities immediately after exiting the burner outlet. This can be explained by the exchange of
294 momentum between gas and particles within the feeder tube. Afterwards, particle velocity increased
295 for all cases, showing statistically equivalent behaviors from 20 to around 35 mm from the burner
296 outlet for all cases. Thereupon, all the cases decelerated on average, although considerably faster at
297 low carrier gas flows. In addition, during the deceleration stage, standard deviation increased,
298 indicating heterogeneity in the motion of particles in the jet. This is further documented in Figure 9,
299 which shows the radial velocity profiles of the particles at different heights from the burner outlet.
300 For low carrier gas flows, the deceleration of the jet is propagated from the external regions towards
301 the centerline, while at high carrier gas flows, particles in the center of the jet remained at high

velocity longer. For all cases, particles at the edges of the jet decelerated much faster than at the centerline.

Figure 8 here

Particles at low carrier gas flow rates (high heating rates) exhibit an earlier deceleration downstream the burner outlet than the cases at high carrier gas flow. The effect was more significant for equant particles than for elongated particles. Particles in the external regions of the jet decelerated significantly earlier than at the center. Such quick deceleration cannot be solely explained by the momentum exchange with the surrounding gas flow since the particle velocity profiles before the deceleration stage are flat, and the radial gas flow velocities without particles within this stage are narrowly distributed around 0.5 $m \cdot s^{-1}$. Therefore, if the gas flow is not the cause of these changes, it requires an explanation based on particle density and shape changes.

Figure 9 here

3.3 Morphological changes

Figure 10 presents projected mean minimum and maximum diameters and particle volume as a function of the distance from the burner outlet. These are time averages for all particles within grid squares at the same distance from the burner outlet. To avoid misrepresentation by capturing particles partially out of the field of view, average values from the first and last grid squares have been discarded. The initial minimum dimension of the particles represented in Figure 10 is higher than the mean sieve size, especially for the elongated particles. This contradicts that the particles had size fractions within the boundaries of the sieve sizes, as it can be seen in Figure 2. The mean of the volume-averaged particle size distribution obtained with the high speed imaging software was measured around 10% higher than the one obtained with a commercial particle size analyzer. Further details can be found in the supplementary material.

The discrepancy in the measured particle size distributions arises from the geometrical descriptors used by the particle size analyzer and by the high speed camera software. The particle size analyzer uses breadth as the minimum dimension, which is a good descriptor of the sieve size and the high speed camera software uses the minimum axis of the fitted ellipsoid for the projected area of the particle, which overestimates the minimum diameter for elongated particles. However, no common particle dimension descriptors were found for the two methods, so the data retrieved by the high speed camera software had to be used this way.

Figure 10 here

Average particle size decreased monotonically with distance from the burner outlet after 15 mm. The graphs from Figure 10 are averages for all particles within the grid squares at the same height from the burner outlet. Cases at low carrier gas flows (high heating rate) are also the ones with the fastest shrinking, indicating that their devolatilization was also faster than at high gas flows. Around 40 mm from the burner outlet, the average particle dimensions increased again for all the cases at low carrier gas flow. This is an indication of swelling for a significant number of particles within the jet.

Figure 11 represents the radial distribution of mean particle projected volume at different distances from the burner outlet. For elongated particles, it is easily observable that either swelling occurs preferentially at the edges of the jet or that swollen particles were ejected to the edges preferentially, while particles close to the centerline shrink faster. Swelling is a well-known phenomenon in other heterogeneous fuels, such as coal [27] or black liquor [28] and has been observed for biomass under certain conditions [29]. The main parameter of control for swelling is heating rate, well described for bituminous coal particles by Fletcher et al. [18]. The experimental results from the previous study revealed that devolatilization at very high heating rates promotes swelling, (10^4–10^5 $K \cdot s^{-1}$). However, these results might not be exactly the same for other biomass

fuels, due to differences in the plasticity and composition of the molten phase. The differences in the radial distribution of particle volume are not as intense for equant particles, compared to the elongated ones at the same flow conditions, indicating that either the initial aspect ratio of the feedstock or the heating rate is affecting the swelling rate. Since particle feeding rates were also lowest under low carrier gas flow conditions, we can attribute the higher tendency for swelling solely to feedstock aspect ratio. This heterogeneity in the radial distribution of particle volume can explain in part the deceleration of the particles at the edges of the jet: swelling would decrease the apparent density of the particles, increasing buoyancy, and increase the surface perpendicular to the motion, increasing the drag coefficient.

Figure 11 here

Figure 12 represents the aspect ratio distribution at different distances from the burner outlet. At the burner outlet, higher aspect ratios were seen at the edges for the more elongated particles. This could be explained by the tendency of elongated particles to disperse radially in flows with a radial velocity gradient [30]. At further distances from the burner outlet, when swelling begins to occur, aspect ratios begin to decrease at one edge of the jet for all conditions. Eventually, further downstream, both edges of the jet present low aspect ratios. This indicates spherodization at the edges of the jet, which can be correlated to swelling of a molten phase due to bubbling. Particle lateral migration towards the external regions of the jet, which present lower gas velocities, could decelerate the particles, explaining the decrease in the velocity trend after 35 mm from the burner outlet in Figure 8.

Figure 12 here

3.4 Particle volume fraction changes

Figure 13 represents the radial distribution of volume fraction at different distances from the burner outlet. For the low gas flow cases after the particle swelling stage (>40mm from the burner outlet), the maximum volume fractions start to shift to the edges of the jet, as a combination of lateral migration and swelling. Since lateral migration due to gradients in the flow field should be more intense for cases at high gas flow, there must be an additional radial force drifting away the particles from the centerline axis at low carrier gas flows. This force could be related to momentum conservation due to fast volatile release of volatiles, enhanced by high heating rates, similar to the jet force described by Elfasakhany et al. for pulverized biomass flames [31]. Interestingly, from Figure 12 we know that these particles at the edges of the jet have a lower aspect ratio and from Figure 11 that they have a higher particle volume, indicating that the same swollen particles that are dispersing laterally and spherodizing, are the ones contributing to the overall deceleration of the average particle velocity within the jet.

In order to substantially affect the volume fraction at the centerline and produce an accumulation of swollen particles at the sides, lateral migration needs to be faster than the average velocity of the jet, and cannot be solely explained by differences in the drag coefficient or particles getting out of the field of view or external perturbations. Enhanced volatile release at high heating rates [32] could increase the momentum of these particles, favoring dispersion. Reactive boiling of a molten phase can explain the fast exchange of momentum, as well as the swelling and spherodization.

Figure 13 here

4. Conclusions

This study has experimentally measured size, shape and particle velocity as well as volume fraction of devolatilizing biomass particles in a jet flow as a way to assess the influence of carrier gas flow and

particle aspect ratio on the devolatilization behavior. Experiments were carried out under CO_2 rich atmospheres to resemble devolatilization conditions under entrained-flow gasification. A combination of high carrier gas flows and high particle volume fractions delayed the onset of disperse incandescent matter (i.e. soot), within the jet, affecting the heating rate of particles and their conversion behavior. Particle swelling was observed at low carrier gas flows (high heating rates), and was also accompanied by spherodization, lateral migration and fast deceleration. Decelerated swollen particles contributed to a substantial decrease in the average velocity of the particle flow downstream the burner outlet. Radial migration and swelling were more intense for high heating rates and elongated particles. Momentum conservation due to fast volatile loss, enhanced at high heating rates, could explain the fast radial migration of swollen particles, however this hypothesis needs further investigation.

This study remarks the importance of considering local fuel concentration, particle shape and particle velocities for the modelling and simulation of streams of biomass particles undergoing devolatilization. The modification of operational parameters used for the active control of suspension firing techniques, such as EFBG or oxyfuel combustion can affect the temperature of the jet and the heating rate of the particles, and the high aspect ratios of biomass feedstocks can enhance effects related to the heating rate, such as swelling, melting, spherodization and lateral migration.

Acknowledgements

The authors would like to thank Norrbottens Research Council and the Kempe Foundation for funding this research, in addition, this work was carried in cooperation with GAFT project, co-funded by Research Council of Norway and industrial partners (Project Number: 244069).

References

[1] Cherubini F, Peters GP, Bernsten T, Strømman AH, Hertwich E. CO_2 emissions from biomass combustion for bioenergy: atmospheric decay and contribution to global warming. GCB Bioenergy 2011; 3:413–26. https://doi.org/10.1111/j.1757-1707.2011.01102.x.

[2] Hansen J, Sato M, Kharecha P, Beerling D, Berner R. Target atmospheric CO_2 : Where should humanity aim? Open Atmos Sci J 2008;2:217–31.

[3] Naik SN, Goud VV, Rout PK, Dalai AK. Production of first and second generation biofuels: A comprehensive review. Renew Sustain Energy Rev 2010;14:578–97. https://doi.org/10.1016/j.rser.2009.10.003.

[4] Milne T, Evans RJ. Biomass Gasifier " Tars ": Their Nature , Formation , and Conversion. Constraints 1998:v. https://doi.org/10.2172/3726.

[5] Qin K. Entrained Flow Gasification of Biomass. Ph.D. thesis 2012.

[6] Repellin V, Govin A, Rolland M. Energy requirement for fine grinding of torrefied wood. Biomass and Bioenergy 2010;34:923–30. https://doi.org/10.1016/j.biombioe.2010.01.039.

[7] Svoboda K, Poho M, Hartman M. Pretreatment and feeding of biomass for pressurized entrained flow gasification 2009;90:629–35. https://doi.org/10.1016/j.fuproc.2008.12.005.

[8] Blasi C. Heat, momentum and mass transport through a shrinking biomass particle exposed to thermal radiation. Chem Eng Sci 1996;51:1121–32.

[9] Lu H, Ip E, Scott J, Foster P, Vickers M, Baxter LL. Effects of particle shape and size on devolatilization of biomass particle. Fuel 2010;89:1156–68. https://doi.org/10.1016/j.fuel.2008.10.023.

[10] Richter A, Nikrityuk PA. Drag forces and heat transfer coefficients for spherical, cuboidal and ellipsoidal particles in cross flow at sub-critical Reynolds numbers. Int J Heat Mass Transf 2012;55:1343–54. https://doi.org/10.1016/j.ijheatmasstransfer.2011.09.005.

[11] Tran-cong S, Gay M, Michaelides EE. Drag coefficients of irregularly shaped particles 2004;139:21–32. https://doi.org/10.1016/j.powtec.2003.10.002.

[12] Pecha MB, Arbelaez JIM, Garcia-Perez M, Chejne F, Ciesielski PN. Progress in understanding the four dominant intra-particle phenomena of lignocellulose pyrolysis: chemical reactions, heat transfer, mass transfer, and phase change. Royal Society of Chemistry; 2019. https://doi.org/10.1039/c9gc00585d.

[13] Holmgren P, Wagner DR, Strandberg A, Molinder R, Wiinikka H, Umeki K, et al. Size, shape and density changes of biomass particles during rapid devolatilization. Fuel 2017;206:342–51. https://doi.org/10.1016/j.fuel.2017.06.009.

[14] Dufour A, Castro-Ďaz M, Marchal P, Brosse N, Olcese R, Bouroukba M, et al. In situ analysis of biomass pyrolysis by high temperature rheology in relations with 1H NMR. Energy and Fuels 2012;26:6432–41. https://doi.org/10.1021/ef301310x.

[15] Zhu G, Zhu X, Xiao Z, Zhou R, Yi F. Pyrolysis characteristics of bean dregs and in situ visualization of pyrolysis transformation. Waste Manag 2012;32:2287–93. https://doi.org/10.1016/j.wasman.2012.07.004.

[16] Haas TJ, Nimlos MR, Donohoe BS. Real-time and post-reaction microscopic structural analysis of biomass undergoing pyrolysis. Energy and Fuels 2009;23:3810–7. https://doi.org/10.1021/ef900201b.

[17] Bharadwaj A, Baxter LL, Robinson AL. Effects of Intraparticle Heat and Mass Transfer on Biomass Devolatilization : Experimental Results and 2004:1021–31.

https://doi.org/10.1021/ef0340357.

[18] Shurtz RC, Kolste KK, Fletcher TH. Coal swelling model for high heating rate pyrolysis applications. Energy and Fuels 2011;25:2163–73. https://doi.org/10.1021/ef200240u.

[19] Ora MD. Reactivity and burnout of wood fuels. Ph.D. thesis 2011.

[20] Li T, Ku X, Løvås T. CFD simulation of devolatilization of biomass with shrinkage effect 2017;105:505–10. https://doi.org/10.1016/j.egypro.2017.03.348.

[21] Ku X, Li T, Løvås T. Effects of Particle Shrinkage and Devolatilization Models on High-Temperature Biomass Pyrolysis and Gasification. Energy & Fuels 2015;29:5127–5135. https://doi.org/10.1021/acs.energyfuels.5b00953.

[22] Russo E, Kuerten JGM, Geurts BJ. Delay of biomass pyrolysis by gas–particle interaction. J Anal Appl Pyrolysis 2014;110:88–99.

[23] Göktepe B, Umeki K, Gebart R. Does distance among biomass particles affect soot formation in an entrained flow gasification process? Fuel Process Technol 2016;141:99–105. https://doi.org/10.1016/j.fuproc.2015.06.038.

[24] Toftegaard MB, Brix J, Jensen PA, Glarborg P, Jensen AD. Oxy-fuel combustion of solid fuels. Prog Energy Combust Sci 2010;36:581–625. https://doi.org/10.1016/j.pecs.2010.02.001.

[25] Weiland F, Hedman H, Marklund M, Wiinikka H, Öhrman O, Gebart R. Pressurized oxygen blown entrained-flow gasification of wood powder. Energy and Fuels 2013;27:932–41. https://doi.org/10.1021/ef301803s.

[26] Scarano F, David L, Bsibsi M, Akkermans RAD. Comparison of two S-PIV techniques: pinhole model vs image dewarping and misalignment correction. Proc 12th Int Symp Appl Laser Tech to Fluid Mech 2004:1–12.

[27] Yu J, Lucas JA, Wall TF. Formation of the structure of chars during devolatilization of pulverized coal and its thermoproperties: A review. Prog Energy Combust Sci 2007;33:135–70. https://doi.org/10.1016/j.pecs.2006.07.003.

[28] Alen R. Swelling behavior of kraft black liquor and its organic constituents. Bioresour Technol 1994;49:99–103. https://doi.org/10.1016/0960-8524(94)90073-6.

[29] Cetin E, Moghtaderi B, Gupta R, Wall TF. Influence of pyrolysis conditions on the structure and gasification reactivity of biomass chars. Fuel 2004;83:2139–50. https://doi.org/10.1016/j.fuel.2004.05.008.

[30] Qi D, Luo L, Aravamuthan R, Strieder W. Lateral migration and orientation of elliptical particles in Poiseuille flows. J Stat Phys 2002;107:101–20. https://doi.org/10.1023/A:1014502402884.

[31] Elfasakhany A, Tao L, Espenas B, Larfeldt J, Bai XS. Pulverised wood combustion in a vertical furnace : Experimental and computational analyses. Appl Energy 2013;112:454–64. https://doi.org/10.1016/j.apenergy.2013.04.051.

[32] Gil M V., Riaza J, Álvarez L, Pevida C, Rubiera F. Biomass devolatilization at high temperature under N2 and CO2 : Char morphology and reactivity. Energy 2015;91:655–62. https://doi.org/10.1016/j.energy.2015.08.074.

List of tables included in the paper:

Table 1: Ultimate composition and ash analysis of the biomass samples

	Method	High AR	Low AR
Higher heating value, MJ kg^{-1}, dry basis		19.8	19.8
Elementary composition, % on dry mass basis			
Carbon	EN 15104:2011	49.5	49.5
Hydrogen	EN 15104:2011	6.1	6.1
Nitrogen	EN 15104:2011	0.1	0.2
Oxygen	By difference	44.1	44.2
Inorganics	ICP-SFMS	0.2	0.2
Ash analysis, mg/kg on dry mass basis, raw sample			
Al	ICP-SFMS	8.29	
Ca	ICP-SFMS	815	
Fe	ICP-SFMS	16.7	
K	ICP-SFMS	580	
Mg	ICP-SFMS	86.9	

Table 2: Gas composition and adiabatic flame temperature for the experimental conditions, *At standard temperature and pressure conditions

Fresh gas composition (values introduced in the mass flow controllers)					
	O_2 ($l \cdot min^{-1}$)*	CO_2 ($l \cdot min^{-1}$)*	CH_4 ($l \cdot min^{-1}$)*	N_2 shield ($l \cdot min^{-1}$)*	CO_2-carrier gas ($l \cdot min^{-1}$)*
Low carrier gas flow	5.36	3.58	4.29	6.79	0.14
High carrier gas flow	5.36	3.58	4.29	6.79	0.27

Post-combustion gas composition (sampled from exhaust gas using gas chromatography)							
	O_2 vol%	CO_2 vol%	CH_4 vol %	N_2 vol%	H_2O vol%	CO vol%	H_2 vol%
Low carrier gas flow	0.0	13.4	0.0	29.0	29.5	20.9	7.1
High carrier gas flow	0.0	13.8	0.0	28.8	29.5	20.8	7.0

Adiabatic flame temperatures (K, without N_2, from equilibrium calculations)	
Low carrier gas flow	2612
High carrier gas flow	2632

List of figures included in the paper:

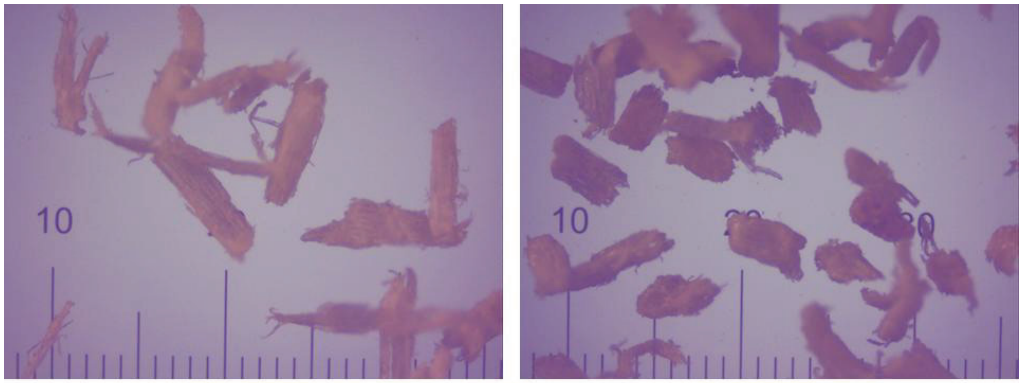

Figure 1: Optical microscope images of the biomass particles used in the experiments (a) high aspect ratio, -elongated- (b) low aspect ratio –equant or nearly spherical-. The lines of the scales in the pictures are separated 100 µm from each other.

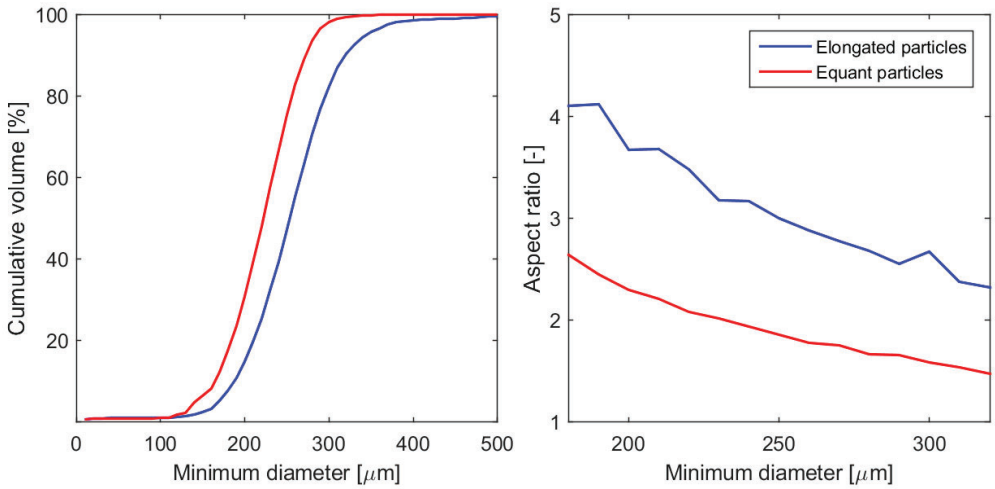

Figure 2: Distributions of particle size and aspect ratio of biomass samples for elongated and equant particles.

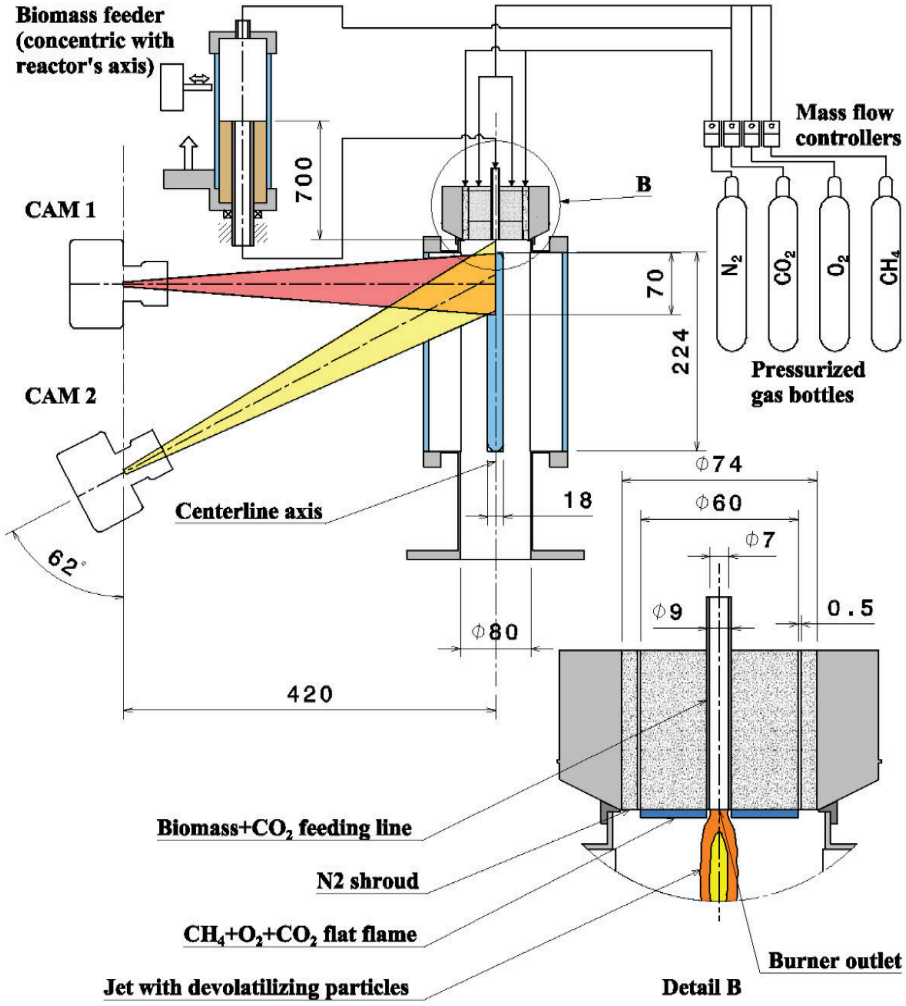

Figure 3: Detailed cross-sectional scheme of the experimental setup. All units are in mm.

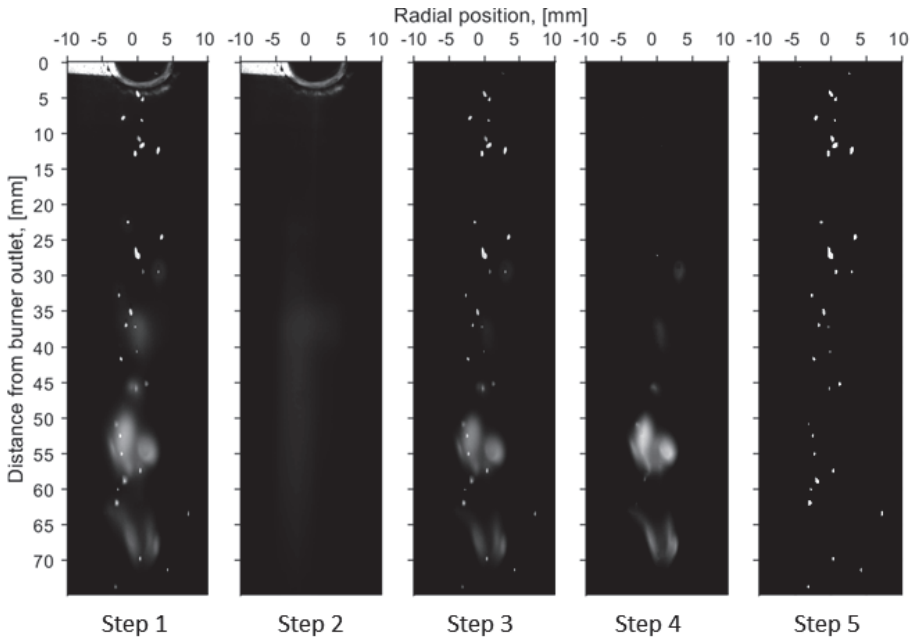

Figure 4: Sequence of image processing steps prior to morphology analysis and particle velocimetry. The images represented here are a case with high carrier gas flow and equant particles obtained at 800 Hz. The element on top of the first two images is the outlet of the burner and a partial sheen from the laser sheet. Bright blurry areas are clouds of disperse incandescent matter. Biomass particles are seen as bright spots due to the scattering of the laser sheet that illuminates them. Videos for 4 different cases are available in supplementary information.

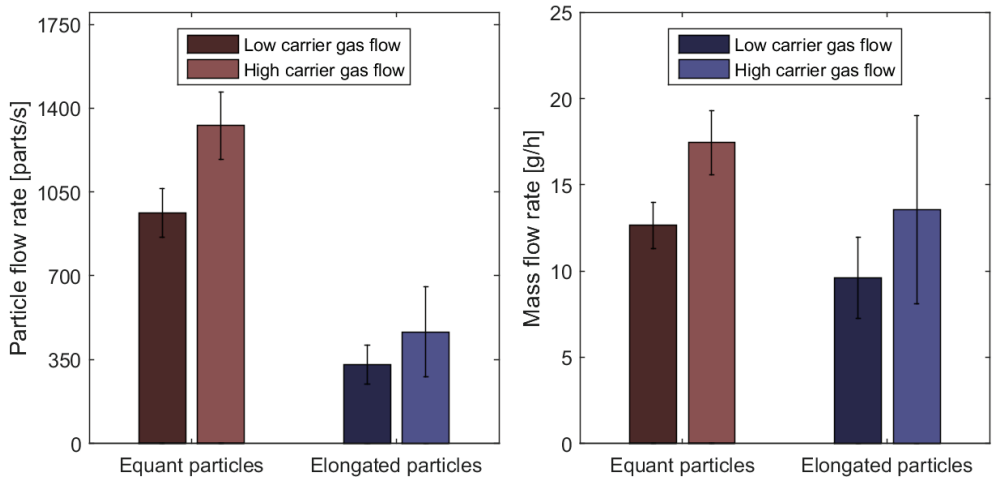

Figure 5: Number and mass flow rates of particles for all experimental conditions, error bars represent standard deviation.

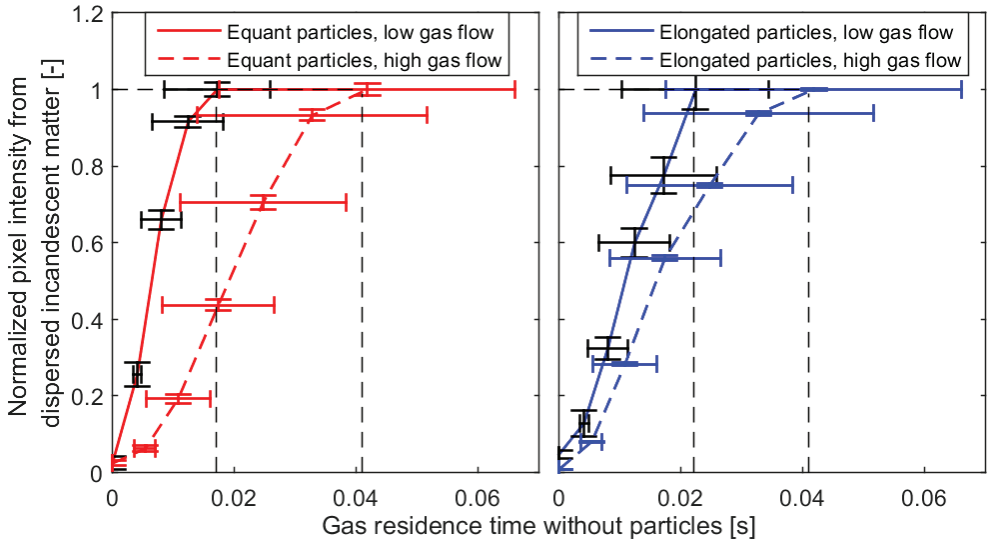

Figure 6: Normalized intensity of light emitted from dispersed incandescent matter versus gas residence time without particles. Horizontal error-bars represent uncertainty in residence time of the gas flow without particles, vertical error bars represent standard deviation of pixel intensity within the studied regions.

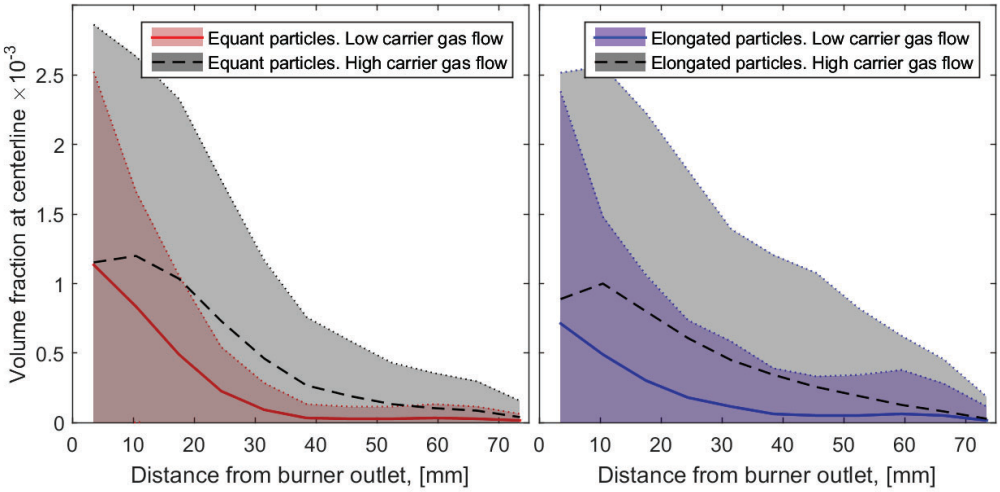

Figure 7: Volume fraction at centerline versus distance from the burner outlet. Shaded areas represent standard deviation.

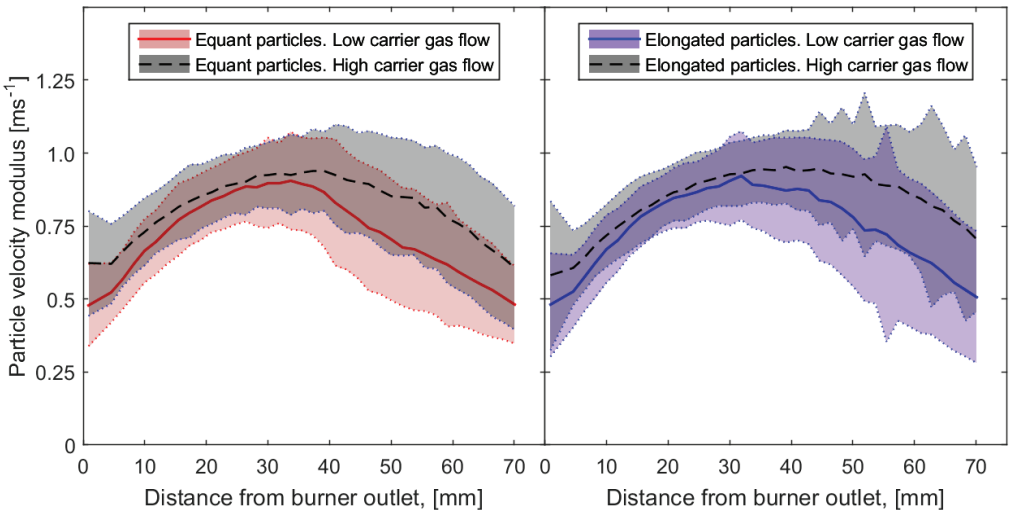

Figure 8: Time-averaged absolute particle velocity versus distance from burner outlet. Shaded areas represent standard deviation.

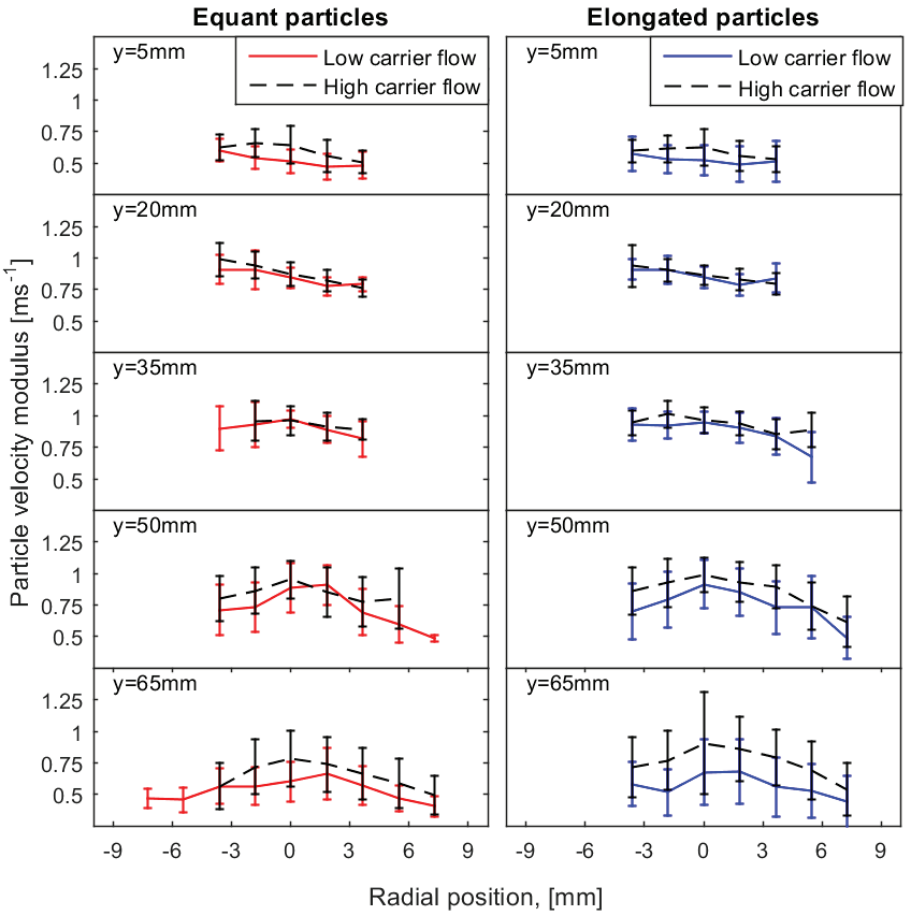

Figure 9: Radial distribution of particle velocity at different distances from burner outlet, y represents distance from the burner outlet. Error bars represent standard deviation.

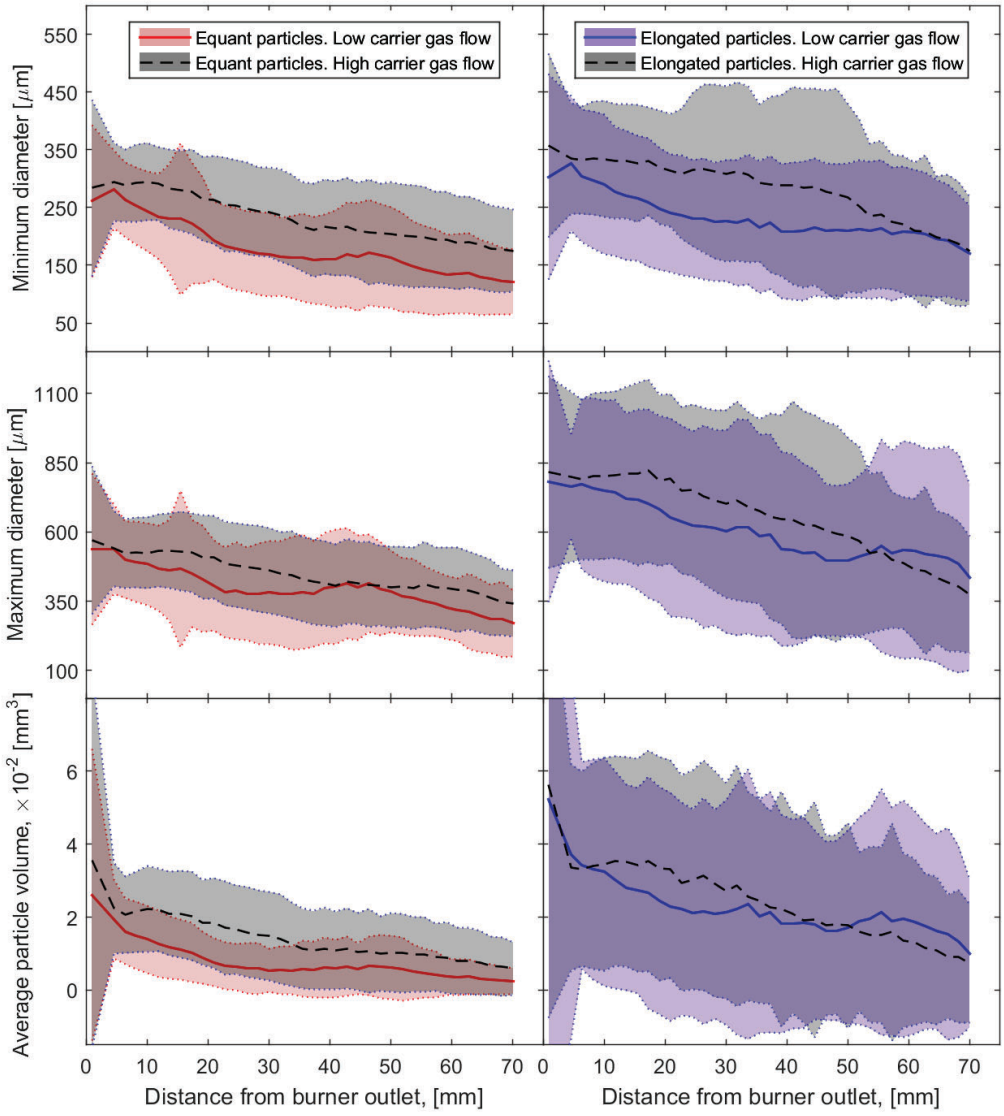

Figure 10: Time-averaged size properties of particles (maximum, minimum diameter and volume) for different jet cross sections versus distance from burner outlet. Shaded areas represent standard deviation.

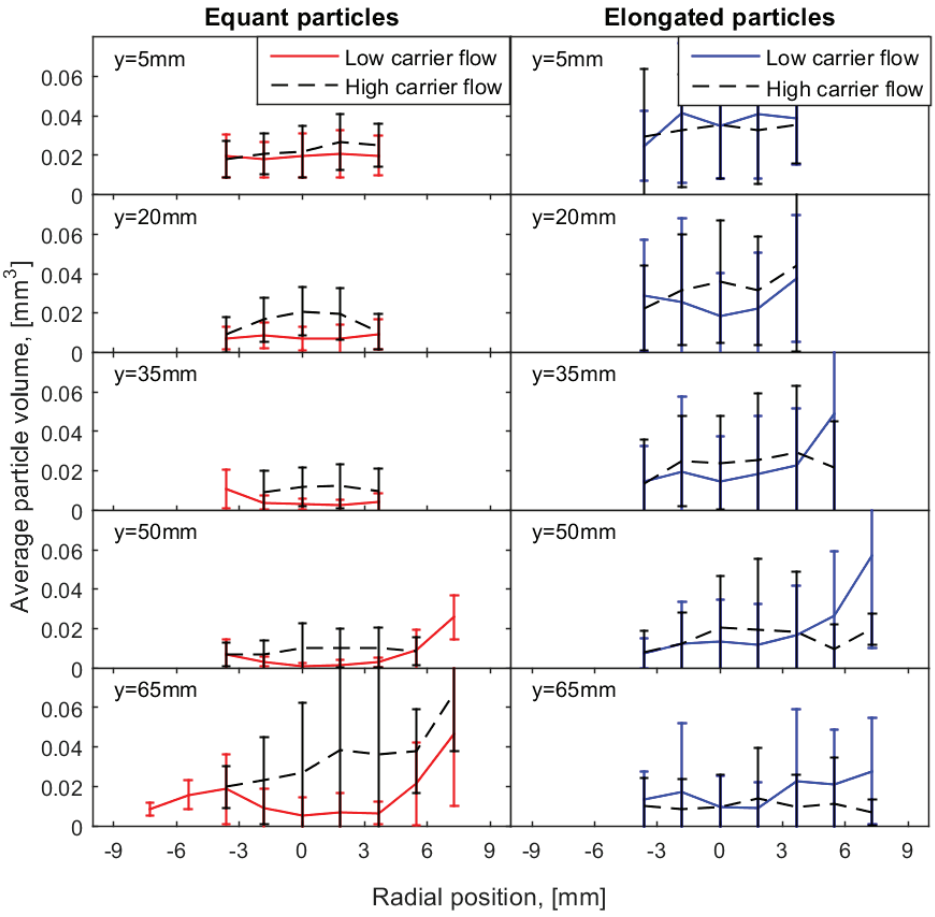

Figure 11: Radial distributions of particle volume at different distances from the burner outlet, y represents distance from the burner outlet. Error bars represent standard deviation.

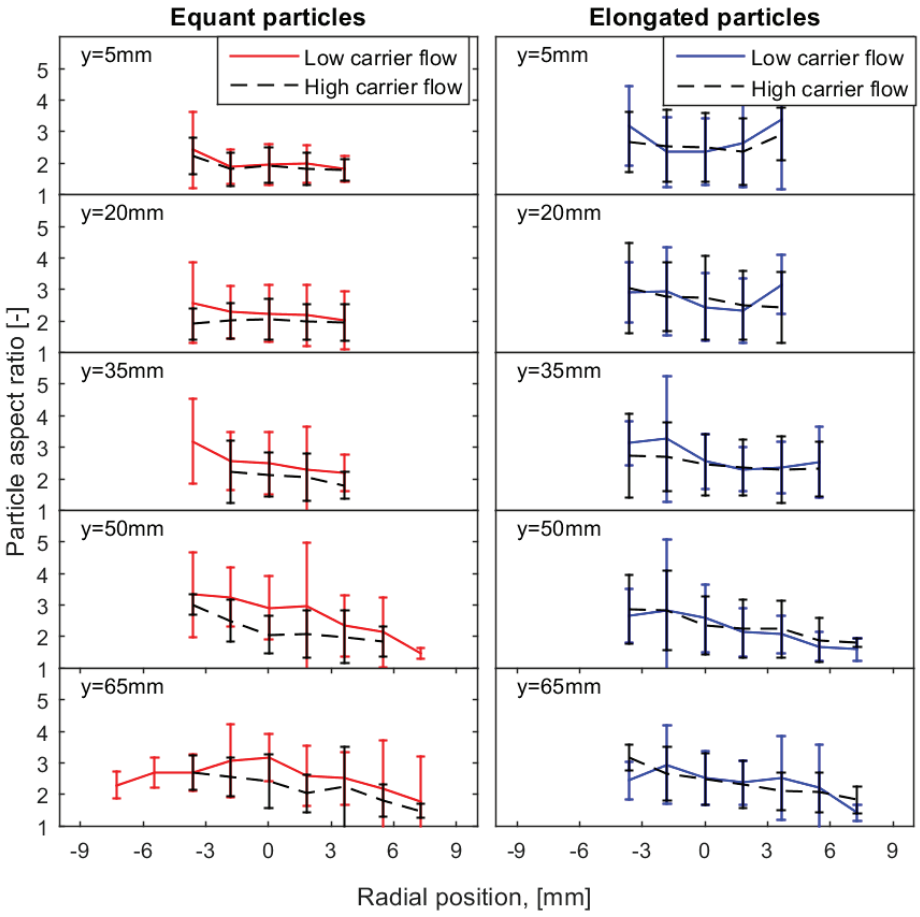

Figure 12: Radial distributions of aspect ratio at different distances from the burner outlet, y represents distance from the burner outlet. Error bars represent standard deviation

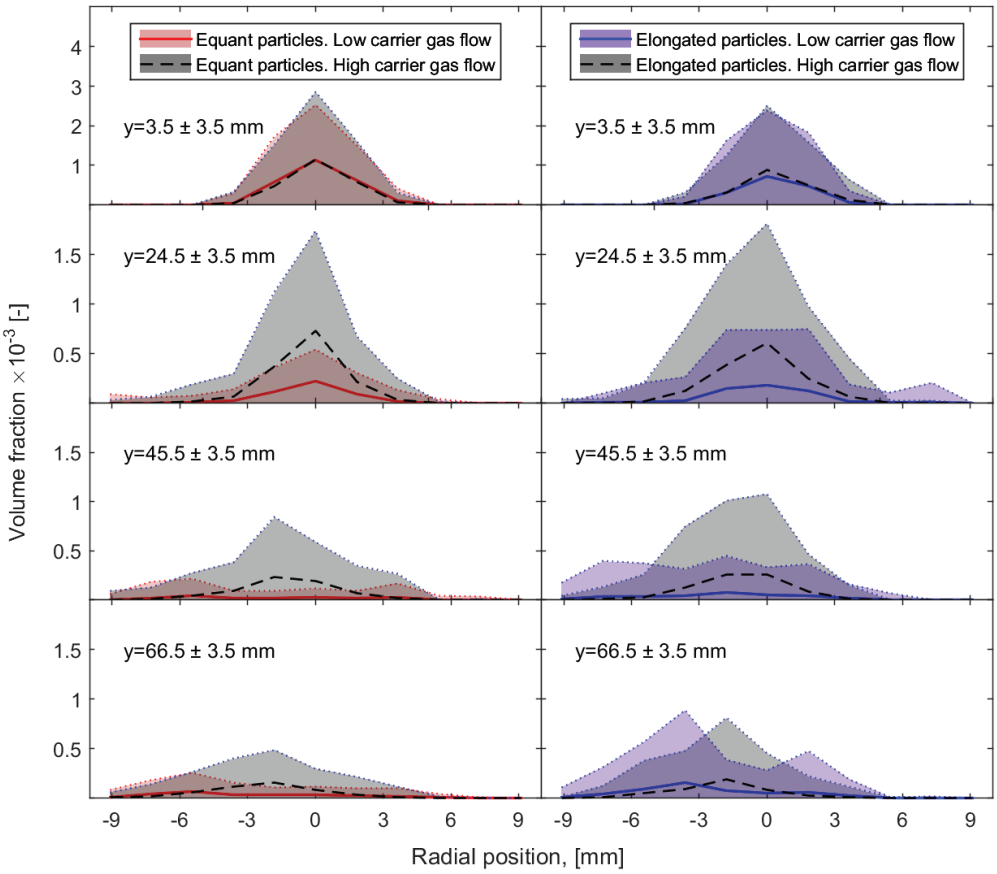

Figure 13: Radial distributions of volume fraction at different distances from the burner outlet. Shaded areas represent standard deviation, notice that the scale of the vertical axis is different for the first two graphs.

Supplementary materials

This document aims to clarify some points not mentioned in the main article, in support of a proper description of the setup, methodology and some further results not deemed important for the storyline of the article.

1. Reactor setup

Figure S1 is a 3D representation of the reactor vessel. The external walls of the reactor were heated with heating tape. The temperature of the external wall of the reactor measured at 50 mm from the burner outlet was 516 ± 17 °C.

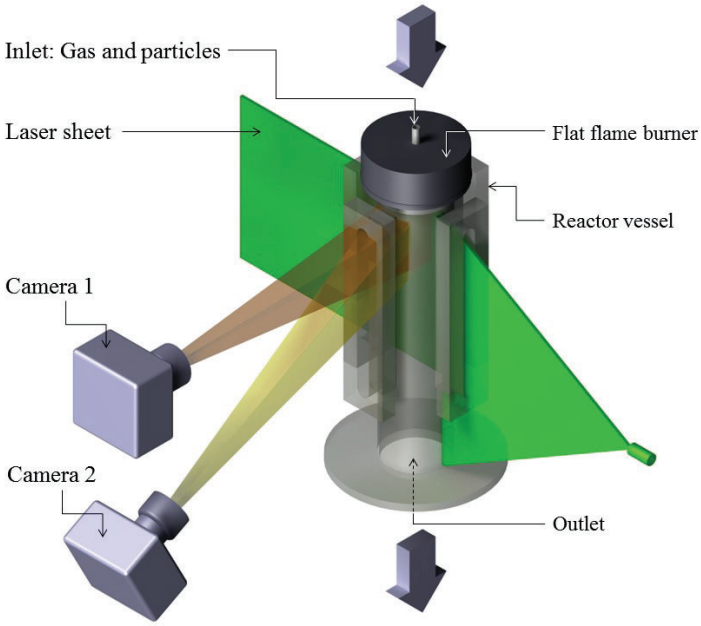

Figure S1: 3D representation of reactor setup

Figure S2 is a snapshot taken from the perspective of Camera 2 with a color camera.

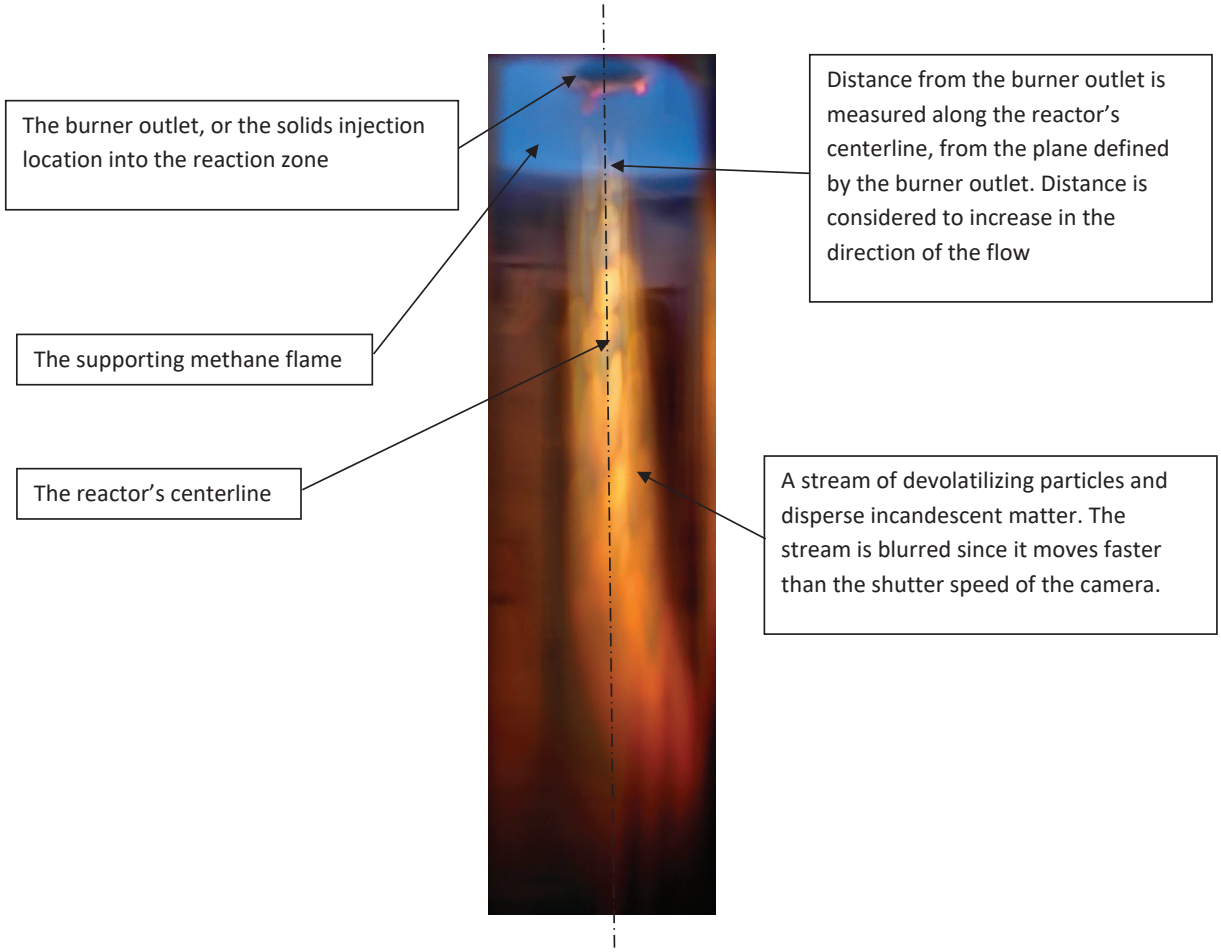

Figure S2: Snapshot taken with a color camera from the same position as camera 2. The blue region is the chemiluminiscence from the planar methane flame. The hole in its center is the burner outlet, where the biomass is injected in the reactor. The trail of blurry incandescent matter is the devolatilizing jet of particles. The walls of the reactor are seen with a red sheen not because they are incandescent, but because they reflect the color of the devolatilizing stream.

2. Uncertainty in size and shape characterization using PTV

2D laser scattering methods such as PTV can only account the cross-sectional projected area of a particle, which depends on its spatial orientation. However, a particle's volume or surface area cannot be inferred from a single cross-section. In addition, several dimensions can characterize the projected area of an irregular particle, depending where the chord is drawn. To overcome these uncertainties, statistical geometric descriptors, such as Feret or Martin diameter provide statistically significant measurements of particle size and shape when averaged over a sufficient number of particles, independent of their orientation. Therefore, the accuracy of size and shape measurements using cross-sectional light-scattering methods relies on the choice of the geometric descriptors for a sufficiently large amount of samples. Particle size distributions from Camsizer measurements (section 2.1) used shortest chord (breadth) for the minimum dimension and maximum Feret diameter to characterize length over a very large number of particles (>2000000). Particle size from Dynamic Studio calculates minimum and maximum dimensions from the diameters of an ellipse fitted to the pixel mask of a particle. Then, a time and spatial averaging for a regular square grid of 1.82x1.82 mm was performed

to achieve a statistically significant number of particles for each grid square. Size and shape characterization from PTV measurements was compared with Camsizer measurements under non-reactive flow conditions. Figure S3 represents the size fraction distributions obtained with the two measurement techniques. The volume-averaged particle size distributions obtained with the two methodologies present good agreement with each other. In addition, mean and standard deviation of particle minor and major axis remained constant for centerline grid squares. This indicates a sufficient number of samples, and mean values as good indicators of particle dimension. It also shows that the particle size measurements have negligible bias against the axial positions, giving confidences on the size changes observed in the results under reactive conditions.

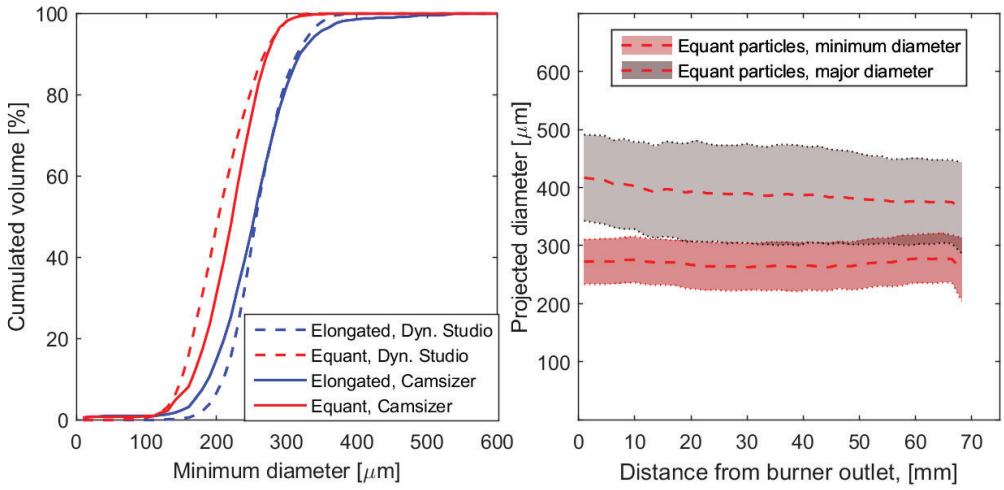

Figure S3: Size fraction distributions measured with Camsizer and PIV techniques (left) and minimum and maximum dimensions of equant particles under non-reactive conditions versus distance from the burner outlet. Shaded areas represent standard deviation.

3. Uncertainty estimation for the feeding rate

The number flux was obtained from PTV data. Therefore, the mass flow rate $\dot{m}$ in $\mathrm{kg \cdot s^{-1}}$, with its associated standard deviation, $\sigma_{\dot{m}}$ can be expressed as:

$$\dot{m} = \bar{m}_{part} \cdot \bar{\Phi}_N \cdot A_{burner} \pm \sigma_{\dot{m}} \quad \text{(S1)}$$

Where $\bar{m}_{part}$ is the average mass per particle in kg, $\bar{\Phi}_N$ is the particle flux, with units $\mathrm{m^{-2} \cdot s^{-1}}$ and A_{burner} is the area of the burner outlet in $\mathrm{m^2}$. The uncertainty of the mass flow rate $\sigma_{\dot{m}}$ can be obtained by propagation from (1), assuming no cross-correlation and no error in the measurement of the outlet area of the burner as:

$$\left(\frac{\sigma_{\dot{m}}}{\dot{m}}\right)^2 \approx \left(\frac{\sigma_{\bar{m}_{part}}}{\bar{m}_{part}}\right)^2 + \left(\frac{\sigma_{\bar{\Phi}_N}}{\bar{\Phi}_N}\right)^2. \quad \text{(S2)}$$

The mass per particle is approximated to the volume per particle multiplied by density as:

$$\bar{m}_{part} = \bar{V}_{part} \cdot \rho_{spruce} \quad \text{(S3)}$$

where $\overline{V}_{part}$ is the average volume per particle in m^3 and ρ_{spruce} is the density of the spruce particles: 420 Kg·m^{-3} (Repola, 2006) .The uncertainty of the mass per particle is thus proportional to the volume per particle. For this method, particle volume is calculated from the approximation to prolate ellipsoids with mean breadth and maximum average Feret diameters $\overline{d}_{min}$ and $\overline{d}_{max}$ obtained from particle sizing data as:

$$\overline{V}_{part} = \frac{\pi}{6} \cdot \overline{d}_{max} \cdot \overline{d}_{min}{}^2. \quad \text{(S4)}$$

Therefore, the error associated to the mass per particle can be expressed as a function of the uncertainties in minimum and maximum diameter:

$$\left(\frac{\sigma_{\overline{V}_{part}}}{\overline{V}_{part}}\right)^2 \approx \left(\frac{\sigma_{\overline{d}_{max}}}{\overline{d}_{max}}\right)^2 + 2 \cdot \left(\frac{\sigma_{\overline{d}_{min}}}{\overline{d}_{min}}\right)^2, \text{ and hence} \quad \text{(S5)}$$

$$\sigma_{\overline{m}_{part}}{}^2 = (\overline{m}_{part})^2 \cdot \left(\left(\frac{\sigma_{\overline{d}_{max}}}{\overline{d}_{max}}\right)^2 + 2 \cdot \left(\frac{\sigma_{\overline{d}_{min}}}{\overline{d}_{min}}\right)^2\right). \quad \text{(S6)}$$

The average flux of biomass particles, $\overline{\phi}_N$, through the planar surface resultant of the intersection between the laser sheet and the burner outlet, A_{in}, is the product of the average number of particles crossing this surface at any entry event, $\overline{n}_{in}$, times the average frequency of entry, $\overline{f}_{in}$, over the area of the surface:

$$\overline{\phi}_N = \frac{\overline{n}_{in} \cdot \overline{f}_{in}}{A_{in}} \quad \text{(S7)}$$

The area A_{in}, would be seen as a line at 0 mm from the burner outlet by the imaging system, see Figure S2. Using this line as a reference to determine the number flux would be impractical, since particles cannot be detected by the software when they are too close to the borders of the image and particle centroids are used as a reference for particle position. Therefore, the area A_{in} considered for the calculation of the number flux was taken 1.83 mm below the burner outlet. At this height, particle size distributions were still not affected by conversion and particles presented little lateral migration. The incoming rate of particles per second $\overline{f}_{in}$ and its standard deviation $\sigma_{\overline{f}_{in}}$ were calculated from the average time difference between particles entering this area. The average number of particles crossing A_{in} between the period of the incoming rate, $\overline{n}_{in}$ and its associated standard deviation $\sigma_{\overline{n}_{in}}$ were obtained from the average number of particles crossing the surface during the period of the average incoming rate. Therefore, the uncertainty of the mass flow rate was approximated by propagation to:

$$\left(\frac{\sigma_{\dot{m}}}{\dot{m}}\right)^2 \approx \left(\frac{\sigma_{\overline{d}_{max}}}{\overline{d}_{max}}\right)^2 + \left(\frac{2 \cdot \sigma_{\overline{d}_{min}}}{\overline{d}_{min}}\right)^2 + \left(\frac{\overline{f}_{in}}{\overline{\phi}_N \cdot A_{in}}\right)^2 \cdot \sigma_{\overline{n}_{in}}{}^2 + \left(\frac{\overline{n}_{in}}{\overline{\phi}_N \cdot A_{in}}\right)^2 \cdot \sigma_{\overline{f}_{in}}{}^2 \quad \text{(S8)}$$

4. Heating rate estimation from images

Figure S4S4 represents the averaged images from the step 5 in the image processing method, normalized to the maximum pixel value from all the images. Figure S5 represents the normalized intensity of the light signals averaged for squares of 6x6 mm centered at the reactor's axis (radial position=0 mm).

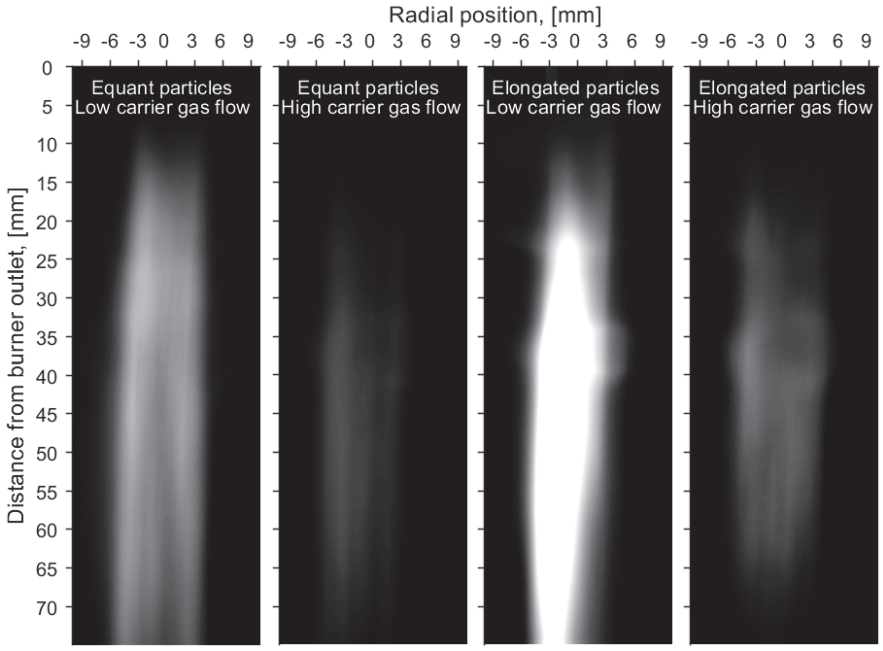

Figure S4: Averaged images of light emitted from disperse incandescent particles that are not biomass particles (i.e. soot) for different conditions. All pixel values are normalized to the maximum pixel intensity

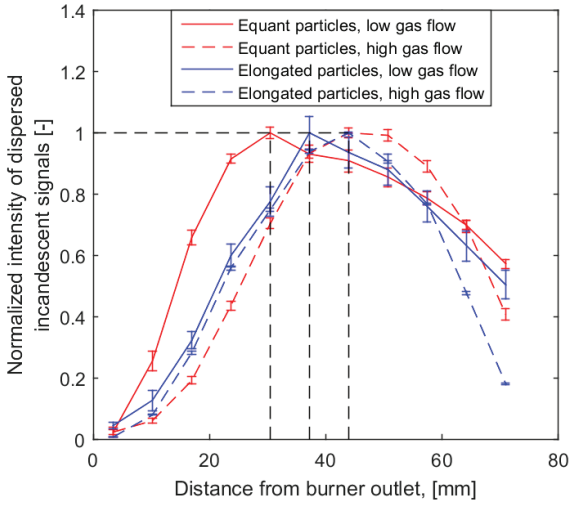

Figure S5: Normalized intensity of dispersed incandescent signals to the maximum value for each image. Error bars represent standard deviation of the all the averaged pixel values for all the images in step 5 contained within the 6x6 squares centered at the reactor's axis

Figure S6 represents the carrier gas flow velocities measured under hot flow conditions with PIV, using 10 nm seeding particles of titanium dioxide. The space time-transform used for Figure S6 in the article are obtained from here. Cases at high carrier gas flow present on average a lower velocity due to the additional mass of gas preventing expansion.

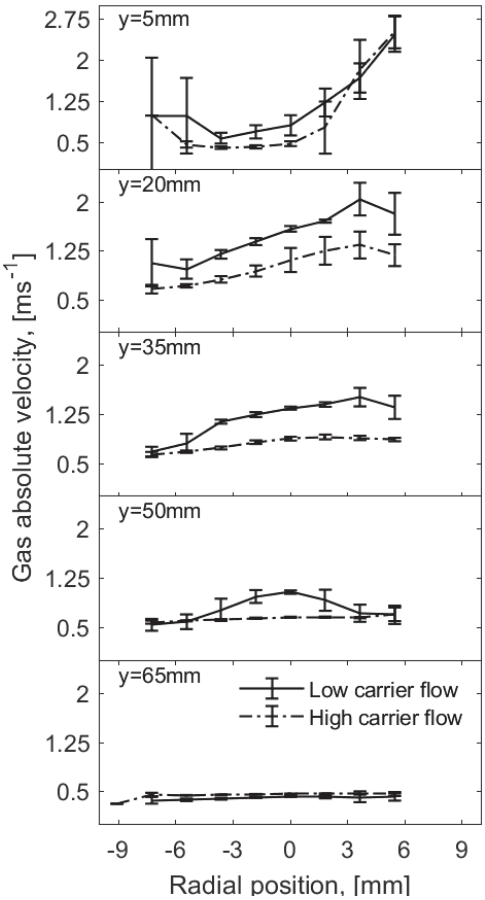

Figure S6: Radial distribution of carrier gas flow without biomass particles at different heights from burner outlet

5. Particle orientation

Figure S7 shows the distribution of alignment between major axis and the flow direction, with lighter colors of the bars representing further distances from the burner outlet and 0° representing coincidence with the flow direction. Particles ended up aligned with the direction of the flow, with no significant differences based on the experimental conditions.

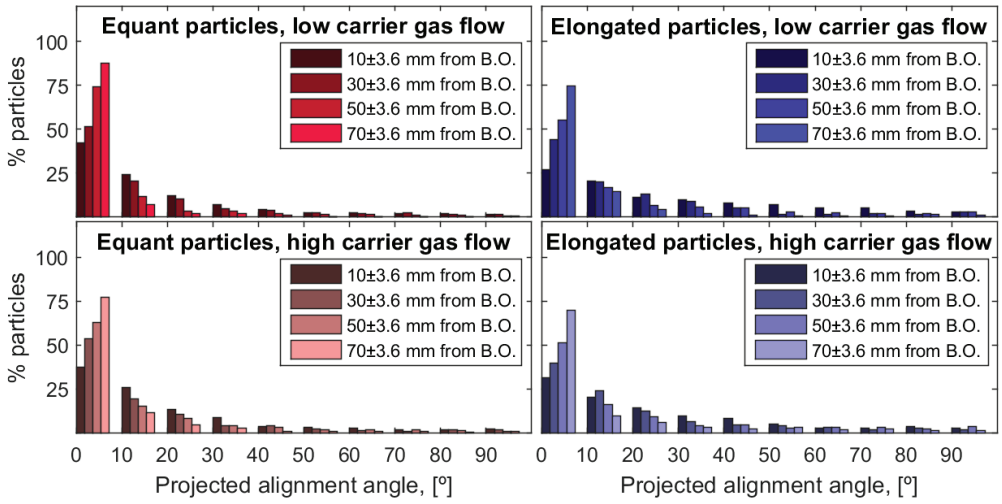

Figure S7: Time averaged histograms of projected alignment angle with the flow direction. Increasing distances from the burner outlet are represented with lighter colors.

References

Repola, J. (2006). Models for Vertical Wood Density of Scots Pine , Norway Spruce and Birch Stems , and Their Application to Determine Average Wood Density. *Silva Fennica*, *40*(July).

Paper 3

Computational fluid dynamic simulations of pulverized biomass conversion using spheroidal approximation

Guo, Ning; Llamas, Ángel David García; Li, Tian; Umeki, Kentaro; Gebart, Rikard; Løvås, Terese.

(Accepted for Publication in *Fuel*)

Computational fluid dynamic simulations of thermochemical conversion of pulverized biomass in a dilute flow using spheroidal approximation

Ning Guo[1], Ángel David García Llamas[2], Tian Li[1*], Kentaro Umeki[2], Rikard Gebart[2], Terese Løvås[1]

[1]Department of Energy and Process Engineering, Faculty of Engineering, NTNU - Norwegian University of Science and Technology, Trondheim, Norway

[2]Energy Engineering, Division of Energy Science, Luleå University of Technology, Luleå, Sweden

*Corresponding author. Email: tian.li@ntnu.no; Tel: +47-73592696

Abstract

A drag force model for spheroids, referred as the spheroid model, was implemented in OpenFOAM, in order to better predict the thermochemical conversion of pulverized biomass. Our previous work has found that the spheroid model predicts more dispersed results in terms of particle velocities and local concentrations comparing to other conventional particle models under non-reactive conditions. This work takes the spheroid model one step further, by validating against experiments performed under *reactive* conditions with a newly implemented heat transfer model for spheroids as well as updated devolatilization kinetic parameters. In addition, simulations were conducted in a configuration similar to a pilot-scale entrained flow gasifier for more realistic scenarios. Particle mass and axial velocity development were compared accordingly using four different modelling approaches with increasing complexity. When compared with models of spheroidal shape assumptions, the sphere and simplified non-sphere model predict 61 % and 43 % longer residence times, respectively. The combination of the spheroid shape assumption with the heat transfer model for spheroids tends to promote drying and devolatilization. On the other hand, the traditional spherical approach leads to longer particle residence times. These opposing effects are believed to be a major contributing factor to the fact that no significant differences among modelling approaches were found in terms of syngas production at the outlet. Furthermore, particle orientation information was reported in both experiments and simulations under

reactive conditions. Its dependency on gas velocity gradient under reactive conditions is similar to what was reported under non-reactive conditions.

Keywords

spheroidal particle, pulverized biomass, CFD, entrained flow gasifier, OpenFOAM

1. *Introduction*

The transport sector is a major emitter of harmful pollutants and accounted for approximate 25% of the global CO_2 emissions in 2016 according to International Energy Agency [1]. As an alternative to traditional liquid fossil fuels, biofuels present a great potential in reducing carbon emissions in this sector [2]. One viable option of producing biofuels is to use gasification technology to gasify pre-treated pulverized biomass to produce syngas; the produced syngas can then be converted to biofuels through Fischer-Tropsch synthesis [3]. Entrained flow gasification is believed to be a promising option for gasification technology, since it is highly efficient, produces less tar in the flue gas and can be employed on large scales [4]. As part of optimizing the underlying thermal conversion of the solid biomass, it becomes necessary to understand the details of the physical and chemical processes involved, both through experimental investigation as well as modelling and simulation. This involves comprehensive studies of gas-particle flows under reacting, and sometime highly turbulent, conditions.

The shape of the pulverized biomass has been given considerable attention in recent works. Results from several research groups have repeatedly shown that pulverized biomass particles are irregularly shaped due to their fibrous structure [5][6][7]. However, it is common practice for simplicity to assume that pulverized biomass particles are spherical [8][9][10]. This approach could potentially lead to simulation results significantly deviating from reality as particle shape is known to affect particle behaviors in terms of hydrodynamics and hence thermochemical conversion. Modelling and experimental efforts investigating the shape effects have been made for both coal particles [11][12][13] and biomass particles [14][15]. However, studies of biomass in a condition that is similar to entrained flow gasification are scarce.

To address this issue, a reasonable first step is to study non-spherical particle hydrodynamic behaviors under non-reactive conditions. Trubetskaya et al. [16] provided an approach that uses an infinite cylinder with volume-to-surface ratio (based on 2D dynamic imaging measurement) to represent the various distribution of sizes and shapes of biomass particles in combustion models. Haider and Levenspiel [17], Zastawny et al. [18], Rosendahl [19], and Hölzer and Sommerfield [20] proposed various drag force models for particles of various shapes, such as cylinders, elliposoids, discs, fibers and other non-spherical particles. Jeffery [21] and Rosendahl [19] reported on different models for particle torques

depending on particle shape. Based on their work, our previous study considered pulverized biomass particles to be prolate spheroids and investigated the effects on particle velocity, residence time and local concentration under non-reactive conditions, quantitatively with considerations of particle torques [22]. It was found that different shape assumptions lead to different predictions of particle residence times and local concentrations [22].

Given the aforementioned findings under non-reactive conditions, one can postulate that the particle shape plays an important and complex role also under reactive conditions. Non-spherical particles have larger ratios of surface area to volume than spherical particles. Additionally, morphological changes occur during the particle thermochemical conversion as evidenced by Panahi et al. [7], which are difficult to predict. They influence particle heat and mass transfer, hence affecting drying, devolatilization and char conversion. Lu et al. [15] investigated effects of particle shapes on biomass devolatilization, and both experiments and simulations show that less symmetrical particles react faster than near spherical particles, which indicates that shape irregularity impacts the overall conversion rate already at relatively small particle sizes (~320 μm). This is confirmed by the analytical study of Li and Zhang [23] who found that the aspect ratio of particles presents a positive correlation to char combustion rate under forced convection.

All of the works mentioned above point towards the importance of accurately modelling the force, torque, shape and surface area of particles as non-spherical under reactive conditions. Various attempts have been made to address these problems in reactive multi-particle settings [24]. One approach is to introduce a shape factor to account for particle shape irregularities, such as the work of Bhuiyan and Naser [25], who modelled co-firing process of biomass and coal under oxy-fuel conditions. Another alternative approach is to employ a more sophisticated particle hydrodynamics model with considering particle orientations and directionalities. Bonefacic et al. [26] and Yin et al. [27] both conducted numerical studies for co-firing biomass with coal and compared differences between two modelling methods (spherical and cylindrical shape assumptions for biomass particles). Bonefacic et al. [26] found that the concentrations of carbon monoxide and nitrogen monoxide in the flue gases were more accurately predicted when using the cylindrical shape assumption than the spherical one, even though biomass only makes up 20% weight in the biomass/coal fuel mixture. Yin et al. [27] found that biomass

volatiles were released earlier and more completely in simulation with cylindrically shaped biomass particles when compared to spherical ones. Even though some of these studies compared simulation results with experimental data of gas species, their simulations were not compared with experimental data of the particles themselves. In addition, to the authors' best knowledge, a thorough comparison of these different modelling approaches under entrained flow gasification of only pulverized biomass has not been conducted and their effects on the resulting syngas quality need to be examined.

Built on our previous non-reactive study [22], this work takes one-step further to study shape effects under reactive conditions and serves three purposes. First, it aims to quantitatively study the differences between the sphere model, the simplified non-sphere model and the spheroid model under reactive conditions. Subsequently, it provides information on particle orientation, which is usually not included in other simulation works. Thirdly, the results from simulations are compared with experimental results in terms of biomass particle hydrodynamics in a drop tube burner, which is rarely found in literature. The current work furthermore adapts the particle surface area to the prolate spheroid for more accurately capture the mass and heat transfer. A heat transfer model for spheroids and a new set of kinetic parameters for devolatilization that are more suitable for entrained flow gasification conditions are employed to better simulate thermochemical conversion of pulverized biomass. It should be noted that the main purpose of this paper is to study the shape effects of biomass particles in entrained flow gasification process using CFD simulations. It does not aim to assess different kinetic models for thermochemical biomass conversions, so only simple models are used in this regard.

The paper is divided in four sections. Section 2 outlines the theory and methodology of the three particle hydrodynamic models, heat transfer models and the devolatilization kinetic parameters. Section 3 compares simulations using the spheroid model to experiments in a lab-scale drop tube reactor under reactive conditions. Section 4 applies different particle shape and heat transfer approaches to an entrained flow gasifier for a comparative analysis and Section 5 summarizes the conclusions and gives future recommendations.

2. *Modelling theory and methodology*

The CFD simulations were conducted in an Eulerian-Lagrangian framework using the open source platform, OpenFOAM 4.1 and were solved with a modified solver based on coalChemistryFoam [28]. There are two options for modelling particle mass loss in OpenFOAM. The first one assumes that the particle size decreases, but its density remains constant. The other one assumes that the particle density decreases, but its size remains constant. Indeed, neither of them can reflect reality that both size and density changes attribute to the particle mass loss [29]. Additionally, the shrinkage behavior is still not well understood for sub-millimeter pulverized biomass particles under the investigated high temperature conditions. Due to the lack of overwhelming evidence of either models' superiority, the first option was chosen based on the work of Ku et al. [30]. This configuration in OpenFOAM would furthermore make it easier to implement changes to the particle aspect ratios in the future.

The theory and methodology is consistent with the work of Ku et al. [28] and will not be repeated here (the considered chemical reactions and their rates can be found in the supplementary material). However, since this work investigates biomass particles using different shape approaches, only the different particle hydrodynamic models (Section 2.1) and heat transfer models (Section 2.2) are described in here in more detail, as to the work of Ku et al. [28] where the common practice of simulating pulverized biomass particles as spheres is employed. In addition, a new set of kinetic parameters for devolatilization is applied and is explained in Section 2.3.

2.1. *Particle hydrodynamics*

This section briefly explains the employed theory of particle hydrodynamics, as detailed information on particle hydrodynamics and underlying conservation equations can be found in our previous paper, i.e. Guo et al. [22]. In this work, all particles are subject to gravity and buoyancy in the simulations. In addition, three different particle models are used to account for particle drag and torque: the sphere model, the simplified non-sphere model and the spheroid model. The sphere model is a widely used approach and considers particles as spheres of equivalent volume [28]. As a result, all particles behave the same. The simplified non-sphere model, reported by Haider and Levenspiel [17], compensates for the effects of different particle shapes by introducing an overall shape factor to characterize particle

shape irregularities. It represents a more realistic treatment of biomass particles, but still does not account for rotational motions of particles. The spheroid model treats particles as prolate spheroids. Particle drag force and torque are both calculated based on the work of Hölzer and Sommerfield [20] and Jeffery [21], respectively. The directions or orientations of the particles are considered by introducing overall, lengthwise and crosswise sphericity of the particle. When the spheroid model is applied, the particle surface area for heat and mass transport is corrected to the surface area of a spheroid. In addition, the current model allows for different particles having different aspect ratios, although it does not allow particle aspect ratio to change for the given particle throughout the thermochemical conversion process. It should be noted that several experiments have shown that biomass particles will indeed gradually transform into spherical geometries [7][31]. However, to the best knowledge of the authors, no good model has yet been proposed to account for a changing particle aspect ratio due to conversion, which is beyond the scope of the present work. The current spheroid model is for simplicity a point-based model with torque being one-way coupled and has potentials for further improvement. Ideally, to model the particle rotation, one should resolve the flow around the particles, which is computationally expensive. Even so, this still does not consider the morphological changes caused by the conversion processes. Additional forces may be introduced by those processes thus alternating particle orientations. However, these details are beyond the scopes of this work, which intends to provide a first-step simple tool to study the effect of particle shape and orientation, and to reveal the capacity of the implemented model, including the deficiencies.

2.2. Particle heat transfer model

It is common practice to model particle heat transfer by the Ranz-Marshall model for external convection [32][33]. In this model, the particle Nusselt number is calculated as:

$$Nu = 2 + 0.6Re^{\frac{1}{2}}Pr^{\frac{1}{3}}, \quad (1)$$

where *Nu* is the particle Nusselt number, *Re* is Reynolds number and *Pr* is the Prandtl number. However, the Ranz-Marshall model is developed based on a spherical approach and employing it to simulate non-sphere particles could potentially lead to inaccurate predictions.

To remedy this, Kishore and Gu [34] proposed a simple Nusselt number correlation for spheroids:

$$Nu = 2\lambda^{0.3} + Pr^{0.4}\left(0.4Re^{0.5}\lambda^{0.83} + 0.06Re^{\frac{2}{3}}\lambda^{0.1}\right), \quad (2)$$

where λ is aspect ratio of the spheroid, here defined as the ratio of the particle's major to minor axis. It should be noted that the above correlation is limited to the following range of flow conditions: $1 \leq Re \leq 200$, $0.25 \leq \lambda \leq 2.5$ and $1 \leq Pr \leq 1000$. The applicability range of this model is somewhat different than that found typically in entrained flow gasifiers of pulverized biomass particles under atmospheric pressures. Particle Reynolds number of pulverized coal is reported to be mostly in the range of 1 and 10, but can reach up to 100 [35]. Since biomass particles tend to have larger sizes, their particle Reynolds numbers are subject to increase, depending on their pretreatment methods. The particle aspect ratio could also be smaller than 0.25 or larger than 2.5, depending on pretreatment process and morphological changes under reactive conditions, whereas the maximum particle aspect ratio used in this work is 10. In addition, the Prandtl number of the gas flow is estimated to be around 0.69 – 0.75 (based on Prandtl number of air at 0 – 1600 °C, 1 bar). Even though the particle flow in this work may be outside of the given applicability range, this correlation is applied here due to lack of other alternatives. This model is hereafter referred to as Kishore-Gu model.

2.3. Particle devolatilization

In entrained flow gasifiers, biomass particles are subject to fast heating rates, high peak temperatures and short residence times. To accommodate such conditions, the devolatilization kinetic parameters developed by Johansen et al. [31] is applied here. The devolatilization rate is formulated as a single-step first-order Arrhenius reaction as follows:

$$\frac{\mathrm{d}m_{devol}}{\mathrm{d}t} = -Ae^{-\frac{E}{RT_p}}m_{devol}, \quad (3)$$

where m_{devol} is the remaining volatile in the particle [kg], t is time [s], A is pre-exponential factor (18.9×10^3 s^{-1}), E is the activation energy (2.1305×10^7 $J\cdot kmol^{-1}$), R is the universal gas constant [$J\cdot K^{-1}\cdot kmol^{-1}$], and T_p is the particle temperature [K].

3. Comparison with experiment of a lab-scale reactor

The spheroid model has been previously validated under non-reactive conditions [22], and is in this paper further validated under reactive conditions. The simulations presented in this section are based on experiments of pulverized biomass particles injected through a laminar, flat flame assisted drop tube reactor. The experimental and simulation setups are described in Section 3.1, followed by a discussion of the resulting particle and flow axial velocities and particle alignment angles in Section 3.2.

3.1. Experiment and simulation setups

Fig. 1 presents a real photograph and 3D illustration of the flat flame drop tube reactor, which consists of biomass and gas feeder tubes, a porous flat flame burner, four windows for optical access, a reactor body, and exhaust tubes. The simulation geometry was simplified to consist of two cylindrical parts: feeder and reactor, as shown in Fig. 2. The feeder is a 100 mm long cylinder with a radius of 3.5 mm. The reactor is a 360 mm long cylinder with a radius of 40 mm. There are three inlets to the domain. *Inlet F* is a circular face with a diameter of 7 mm and acts as fuel inlet. *Inlet A* is an annular ring with 62.5 mm inner diameter and 73.5 mm outer diameter. *Inlet B* is an annular ring with 7 mm inner diameter and 62.5 mm outer diameter, and it represents the outlet of the porous flat flame burner in the experiment. The outlet is a circular face with a diameter of 71 mm. Other parts are treated as walls.

Selected gases with or without biomass particles were injected via these three inlets according to the experiment, as listed in Table 1. The protective N_2 was injected via *Inlet A*. Biomass particles were carried by CO_2 and injected through *Inlet F*. In the experiment, a mixture of CH_4, O_2 and CO_2 was supplied to the flat flame burner (i.e. prior to the laminar flame) and their flow rates are listed under

Inlet B (experiment) in Table 1. The mixture was ignited and exited the burner (i.e. post-flame) via *Inlet B*. However, in order to save computational costs in the simulations, it is common not to include the combustion process of these gas mixtures in the burner. Chemical reactions are assumed to reach adiabatic equilibrium instead and the products (and their mass fractions) can therefore be calculated accordingly and used in the simulations [36][37]. Following this practice, the gas compositions listed under *Inlet B* (simulation, post-flame) in Table 1 were used as inlet boundary conditions in the simulations. The boundary conditions of the velocity for all these inlets were set to be uniform and were calculated based on their respective flow rates.

The temperature boundary conditions were configured as follows. It was assumed that the temperature of *Inlet F* was at room temperature (300 K). The same temperature was set for *Wall 1V*, as the feeding tube was water cooled. As previously mentioned, *Inlet B* is where the outlet of the porous flat flame burner is located, and it was assumed that chemical equilibrium was achieved here. As a result, the adiabatic flame temperature upon chemical equilibrium, 2560 K, was used here. It should be mentioned that particles were expected to be dried fast at such high temperatures, so particle moisture was assumed to be 0% in Table 2. Based on experimental measurements, the temperature was assumed to be linearly dependent on the height. Therefore, *Inlet A* and *Wall 1H* were set to be 838 K, *Outlet* and *Wall 2H* were set to be 583 K, and *Wall 2V* had a temperature profile linearly interpolated between these two values.

The biomass particles used in the experiments were Norwegian spruce (picea abies). Hence the initial particle density was assumed to be 1100 kg/m^3 with zero porosity, based on the previous work of Li et al. [5]. Similar skeletal densities in the range of 900 – 1200 kg/m^3 have also been reported in other simulation works [36][38]. For simplicity it is assumed that there is no porosity within the biomass particles in the current CFD simulations. The particle sizes were configured according to the experiment, represented by a Rosin-Rammler distribution as shown in Fig. 3. The relationship between the particles' equivalent diameter and aspect ratio was measured in the experiment as shown in Fig. 4, and a simple polynomial formula was used to reflect this trend in the simulations. The particle composition used in the simulation is listed in Table 2, where volatile gases and their percentages are based on the Beechwood data from Ku et al. [28]. Most of the particles were expected to be in the drying and

devolatilization stages. Released volatiles were modelled based on the same devolatilization model and kinetic parameters, regardless of species. Given that the ratio of particle to gas flow mass (or volume) fraction was so low here, the chemical effects of composition of volatile species were expected to be insignificant. Therefore, the estimation of the volatile species and their percentages used in Table 2 is considered sufficiently appropriate in this context. In terms of particle initial orientation, due to the lack of experimental data on this particular point, it was assumed that every one third of particles have their major axes parallel to the *x*-, *y*- and *z*-directions respectively in the gas flow frame when the spheroid model is used. After conducting grid independence tests based on axial velocities of gas flow under reactive conditions without injecting biomass particles, a mesh of 184960 hexahedral cells was used for further simulations in this section, together with the spheroid model and the Kishore-Gu model.

3.2. Results and discussions

3.2.1. Gas flow axial velocities under non-reactive conditions

Fig. 5 presents the axial velocities of the gas flow at different positions away from the burner outlet under non-reactive conditions, without injecting any biomass particles. It provides an overview of the overall gas flow fields, without the complications and influences of chemical reactions and biomass particles. One can see that there is less or even no experimental data outside the radial position of ± 3.5 mm. This is because the experimental data for gas flow was obtained based on tracer particles (TiO_2) injected via *Inlet F*, located within the radial position of ± 3.5 mm. From upstream to downstream (i.e. from 0 mm to 70 mm away from burner outlet), the stream wise axial velocity of the gas flow increase, both in the experiments and the simulations. Since the gas at *Inlet F* (radial position within ± 3.5 mm) had a lower volumetric flow rate per cross-sectional area than that of *Inlet B* (radial position between ± 3.5 mm and ± 31.25mm, part of which is outside the radial range shown in Fig. 5), the aforementioned increasing trend in axial velocity is expected, as the gas from *Inlet F* was accelerated by the gas from *Inlet B*. The simulation match reasonably with the experiment, especially in the middle region of the radial position and from 20 mm to 50 mm away from burner outlet. However, further up-stream some deviation is noted. Several reasons can contribute to this discrepancy. First, asymmetries in the experiment can be clearly detected. This might be caused by the biomass feeder not being completely

283 perpendicular to the ground level in the experimental setup. Furthermore, the experimental data in the
284 upstream (0 mm and 11 mm away from burner outlet) may also be less reliable, due to the fact that the
285 tracer particles had just left the burner outlet and entered the measuring laser plane. In theory, a tracer
286 particle needs to be optically measured twice for post-processing to calculate its velocity based on its
287 time and position at the two measuring points. There is a possibility that some particles that just entered
288 or left the laser plane were only optically measured once, which makes their velocity calculations by the
289 post-processing routine less reliable. Given these factors, it is possible to conclude that the simulations
290 and experiments match reasonably well, apart from close to the inlet, which forms the basis for further
291 simulations with reactive biomass particles.
292
293 *3.2.2. Particle axial velocities under reactive conditions*
294 Fig. 6 shows axial velocities of biomass particles, along the radial direction of the reactor, at different
295 positions downstream from the burner outlet under *reactive* conditions. By comparison, good
296 agreements between simulation results and the experiments are achieved. Some discrepancies are
297 evident and believed to be due to the same reasons as explained in 3.2.1, i.e. reactor asymmetry and
298 particle measurement errors in and out of the laser plane. In the range from 0 mm to 70 mm downstream
299 of the burner outlet, the experimental data indicates that the biomass particles first accelerate, then
300 decelerate. This is not surprising, as when particles are transported further away from the burner outlet,
301 the slip velocities become higher. As a result, drag forces acting on the biomass particles plays an
302 increasing important role and eventually slows down the biomass particles. However, this observed
303 deceleration could not be reproduced in the simulations downstream of the burner outlet. One possible
304 cause could be temperature differences between the experiments and the simulation. The temperature
305 boundary conditions in the simulation were configured only based on a few measurement points at the
306 reactor wall, which may give rise to uncertainties related to temperature predictions in the downstream.
307 This likely results in an over prediction of the gas temperature in the downstream, thus also an over
308 prediction of the gas velocity, supported by the observation of higher particle velocities in the
309 simulations. In addition, the contribution to mass losses based on particle size, aspect ratio and density
310 affect the balance between drag and gravity. The biomass particles in the simulation were assumed to

311 have constant density and aspect ratio. Their mass loses were reflected by size changes only, which is a
312 known shortcoming of the models compared to the experiment. Also, Panahi et al. [7] observed particle
313 spherodization phenomena when biomass particles went through pyrolysis at high temperatures, which
314 was not included in the models in the current simulations. It was also observed that a certain number of
315 biomass particles had sudden changes to their trajectories in the experiments. Similar phenomena was
316 also reported by Elfasakhany et al. [39] and they argued this was caused by the rapid release of volatiles
317 from fibrous biomass particles. This could also explain certain standard deviation exists in the
318 experiments, while biomass particles in the simulation tend to have very similar axial velocities.
319
320 *3.2.3. Particle projected alignment angles under reactive conditions*
321 The particle alignment angle is here defined as the angle between the particle's major axis and the
322 gravity direction. It is an important parameter for determining the particles' hydrodynamics, as particle
323 force and toque are coupled in the present spheroid model. The probability density function of particle
324 projected alignment angles at different positions away from burner outlet is presented in Fig. 7. Projected
325 values are used instead of real 3D values as the current experimental setup can only generate one single
326 laser plane for each measurement. Note that the term "projected" value is conceptually the same in the
327 experiments and the simulations, but differ slightly in their respective post-processing methodologies.
328 In the experiment, laser observed biomass particles have projections in the laser plane, and these
329 projections are the basis to derive projected alignment angles. In the simulations, a virtual plane is
330 created for each particle and it is defined by the gravity line and the particle point, and the particle
331 projected alignment angle is calculated based on its projection on this virtual plane. In the upstream
332 close to the burner outlet, the particle projected alignment angles are in the experiments distributed
333 between 0 – 90° with a preferential concentration close to 0°. As the biomass particles are transported
334 further away from the burner outlet downstream, this preference towards 0° became even more evident.
335 This trend, however, is not reflected in the simulations. At the outlet, numerical results show that one
336 third of particles tend to have projected alignment angles of 0°, while the other two thirds have 90°. This
337 is however in line with the initial configurations of particles upon injection, where every one third of
338 particles have their major axes parallel to *x*-, *y*- and *z*-directions respectively. As particles are transported

downstream, their projected alignment angles are more randomly distributed over the range between 0° and 90°. Njobuenwe and Fairweather [40] have shown that for inertial fibers in turbulent flows, the fiber is mostly anisotropically aligned with the flow direction, where large velocity gradient exists, otherwise they are isotropically aligned. Based on the axial velocity data under non-reactive conditions presented in Fig. 5, it is reasonable to assume that velocity gradients in the experiments were more evident than simulations due to thermal expansion of gas flow fields under reactive conditions.

4. Application to a simplified entrained flow gasifier

In this section, the aforementioned three different particle models are applied to simulate entrained flow gasification of pulverized biomass under close to realistic operating conditions. A simplified simulation configuration is a setup based on a pilot-scale entrained flow gasifier as described in earlier sections and is outlined Section 4.1. In Section 4.2, results are presented based on the three particle models as presented above.

4.1. Simulation configurations

In Section 3, a laminar lab-scale reactor was simulated, and a reasonable next step is to scale up and apply the simulation models to a larger and turbulent reactor under more realistic operating conditions. Hence, the pilot-scale entrained flow gasifier reported by Simonsson et al. [41] was chosen as a comparative target for the simulations. As seen in Fig. 8, the gasifier was simplified into two parts, feeder and reactor. The feeder is 100 mm long and has two air registers, inner central tube and outer annular tube. Primary air was injected with biomass into the 50 mm diameter central tube. Secondary air entered via the annular tube with diameter of 52 mm and 56 mm. The reactor part is a 3.5 m long cylinder with diameter of 50 cm.

Boundary and initial conditions were configured based on the operating conditions with an 0.5 air-fuel equivalence ratio, as stated in Simonsson et al. [41]. Primary air was injected at 535 $l \cdot min^{-1}$, secondary air was injected at 410 $l \cdot min^{-1}$ with 3172 rpm to provide swirl. Inlet temperature was set at 300 K. The wall and the internal initial temperature were set at 1428.46 K, based on the experimental measurement by Simonsson et al. [41]. Standard k-ε model was employed to simulate the flows. A mesh

of 1872910 hexahedral cells was selected for further simulations after a grid independence test based on centerline temperature results from reactive simulations without injecting biomass particles.

Pulverized biomass particles were injected at 20.2 $kg \cdot h^{-1}$. The particle composition is listed in Table 3. The volatile gases and their percentages are based on the data from Thunman et al. [42], which is summarized in Haseli et al. [43]. The original paper presenting the experiments (Simonsson et al. [41]) did not provide approximate analysis of the volatiles. However, the goal is to compare the differences between four particle modelling approaches in a realistic configuration. Therefore, the volatile data used here in the current CFD simulations could sufficiently serve the purpose. The particle density is 1100 kg/m^3 as in Section 3. The particle size distribution is described in Fig. 9. The particle aspect ratio is set to 10 based on our previous study [22], as this was not reported in the experimental work from Simonsson et al. [41]. There are two reasons that the aspect ratio is intentionally configured this way. First, Panahi et al. [7] has reported that the average aspect ratio could be 8.2 for Beechwood particles whose average dimensions are 190 × 1500 μm. Second, the simulations are intended to highlight the differences among the different modelling approaches, rather than to compare with experimental results. Therefore, a slightly higher aspect ratio could make the differences among the four approaches more pronounced and serves the purpose of the simulations presented in this section.

Depending on the configurations of the biomass particle models, simulations of four cases are presented in this section, which are listed in Table 4. There are two major motivations to employ such case configurations. The first one is to study the effects of different particle hydrodynamic models based on different assumptions of particle shape. Hence the sphere model was used in *Case 1*, the simplified non-sphere model was used in *Case 2*, the spheroid model was used in *Case 3* and *4*, where particle initial orientations were configured as the same as in Section 3. The other reason is to investigate the impact of the choice of particle heat transfer model. It is common to only use a spherical based heat transfer model, which deviates from the fact that biomass particles are non-spherical. As a result, in *Case 3* and *4*, the Ranz-Marshall model and Kishore-Gu model were used, respectively, here also in combination with the spheroid particle model to study their differences in simulations of entrained flow gasification of pulverized biomass particles.

4.2. Results and discussions

Most results in this section are presented along reactor radial direction, r/D, at different heights, z/D, of the reactor. r is the radial position of the reactor, z is the axial position of the reactor and D is the diameter of the inner tube where biomass particles are injected. The inner central tube, where biomass and air were injected, is located at radial direction of r/D = 0 – 0.5. The outer annular tube, where secondary air with swirl was injected, is located at radial direction of r/D = 0.52 – 0.56. The reactor wall is located at radial direction of r/D = 5. The inner inlet is located at z/D = -0.2, and the outer annular inlet is located at z/D = 0, which is also the start of the reactor. The outlet of the reactor is located at axial position of z/D = 70. All the results below are sampled at 12 s after particle injections start. When particles are sampled at different heights of the reactor, a z/D tolerance of ± 0.05 is applied, which is consistent with our previous non-reactive study [22].

4.2.1. Particle conversion

The rate of particle conversion can be represented by the normalized biomass particle mass, m/m_0, which is defined as the remaining mass of a particle, m, over the initial mass of the same particle, m_0. Fig. 10 shows normalized particle mass along the reactor radial direction (r/D) at different heights (z/D) along the reactor, but only particles with short residence times are sampled. The sampling method is explained as follows. It is reasonably assumed that most of the biomass particles could travel faster than 2 $m \cdot s^{-1}$ in the axial direction without recirculation, based on the results previously shown in Fig. 12. The residence time of a particle with axial velocity of 2 $m \cdot s^{-1}$ is used as threshold here. A biomass particle reaching the plotted axial position (z/D) is included if its residence time is shorter than or equal to the threshold, otherwise it is excluded. The reason for this sampling method is to exclude biomass particles that were trapped in recirculation zones of gas flow fields for a long time, so heat transfer can be studied with minimum influence of particle residence time. Of course, this sampling method is not perfect and, by its definition, will include or exclude particles that contradicts to the original sampling intention. However, it is a fast and simple method that can present an overview of biomass particles outside recirculation zones with tolerable errors. In addition, particles that have entered char conversion stages

are excluded in Fig. 10 since the difference is negligible and the focus here is on particles in drying and devolatilization stages.

The general trend is similar of all four cases, as shown Fig. 10. In the upstream where *z/D* is 0, the normalized particle mass of all cases is close to 1, as thermochemical conversion of biomass particles had just started or was about to start. As *z/D* increases, biomass particles followed the main flow of the surrounding gas and travelled further downstream, where they were heated up and started drying and devolatilization processes, making their normalized mass decreased. Around the axial location of *z/D* = 14, normalized particle masses in all cases are close to 0.15, meaning that particles finished most or all of the drying and devolatilization processes. This is in line with the fact that all biomass particles were configured with 15.4 % wt (weight) of char and ash.

Even though the final output is similar in all four cases, differences in their histories are still present. Their differences are insignificant in the beginning, because drying and devolatilization just began. As *z/D* increases, their differences start to manifest and become obvious at reactor axial location of *z/D* = 6. Normalized particle masses decrease faster in *Case 3* (spheroidRM) and *Case 4* (spheroidKG) than in *Case 1* (sphere) and *Case 2* (nonSphere). Such differences are most pronounced at reactor axial location of *z/D* = 6. This is believed to be caused by their different particle surface areas. *Case 3* (spheroidRM) and *Case 4* (spheroidKG) are based on the assumption of particles being spheroids, and their surface areas were accordingly adjusted, whereas *Case 1* (sphere) and *Case 2* (nonSphere) were essentially simulating particles as spheres of equivalent volume. As a result, the particle surface areas are larger in *Case 3* (spheroidRM) and *Case 4* (spheroidKG) when compared with the ones in *Case 1* (sphere) and *Case 2* (nonSphere), and thus subject to better heat transfer. The difference between *Case 1* (sphere) and *Case 2* (nonSphere) is due to the hydrodynamic models applied, as it is the only difference between the initial configurations of these two cases. The difference between *Case 3* (spheroidRM) and *Case 4* (spheroidKG) is due to the heat transfer models applied, as evidenced in Fig. 11, which shows the Nusselt number ratio predicted by the two heat transfer models at different Prandtl and Reynolds number with ranges that are applicable in an entrained flow gasifier (see discussion in Section 2.2). One can see that the Kishore-Gu model favors heat transfer more than the Ranz-Marshall model under current operating conditions. However, all the differences among these four cases become smaller again when

450 *z/D* increases from 10 to 14. At this stage, the majority of the particles have finished most or all of their
451 drying and devolatilization processes, their masses and surface areas became much smaller, and
452 differences in hydrodynamic and heat transfer models are less relevant.
453
454 *4.2.2. Axial velocities of gas flow and particles*
455 In the previous section, only particles with short residence time are sampled to filter out particles that
456 are in recirculation. This is useful when drying and devolatilization processes are of interest. However,
457 to capture a more realistic representation of the reactor, flow axial velocities of flow fields of all particles
458 along reactor radius (*r/D*) at different height (*z/D*) of the reactor are shown in Fig. 12. Gas flow axial
459 velocities of the four cases are similar with minor differences, so the flow axial velocity of *Case 1*
460 (sphere) is used to represent the flow fields and it is marked by an orange dashed line. In the beginning
461 where the axial location is $z/D = 0$, the flow axial velocity is represented by a plateau within $r/D \leq 0.5$,
462 where the biomass particles were injected via inner central tube. The gas flow axial velocity reaches a
463 maximum where the secondary air was injected, then decreases again as *r/D* increases. This is due to
464 that primary and secondary air flows were injected at different rates. As *z/D* increases, gas flows at
465 different radial positions mix, but they still have relatively high axial velocities due to thermal expansion.
466 One can also observe that axial velocities of the gas flows and particles are negative in regions where
467 *r/D* is relatively large. This means that there are recirculation zones in the gas flow fields. Further
468 downstream, gas temperatures are expected to drop and axial velocities of gas flow decrease.
469 Particles' axial velocities of the four cases are marked with dots with error bar. It can be seen that
470 they generally follow the flow field, especially near the inlet and far away from the inlet. In the
471 intermediate axial locations of $z/D = 5 – 20$, particle axial velocity differs among these four cases. With
472 exceptions, one can conclude that particles with spheroidal shapes have higher axial velocities. However,
473 it is difficult to determine the extent of each factor's influence as the situation is complex with many
474 changing variables. In these axial locations, rapid devolatilization occurs, particles in different cases are
475 subject to different velocity and temperature fields, different particle hydrodynamic and heat transfer
476 models and different mass loses; all of which could make particle axial velocity differences more
477 pronounced in this intermediate axial region among these four cases. Further downstream at axial

478 locations of $z/D \geq 35$, drying and devolatilization are presumably complete, biomass particles lose
479 majority of their mass, thus reducing inertia and making them follow more closely the flow fields as
480 observed in Fig. 12.
481
482 *4.2.3. Particle orientation*
483 Particle alignment angle, previously defined as the angle between the particle major axis and the
484 gravity direction, is a good representation of particle orientation. In a similar manner, Fig. 13 shows
485 probability density distribution of particle alignment angles of *Case 3* (spheroidRM) and *Case 4*
486 (spheroidKG) at different height (z/D) of the reactor. Both have similar trends and do not exhibit
487 significant differences. At axial location of $z/D = 0$, a small portion of particles have alignment angles
488 close to 0° while the rest close to 90°, this agrees with the initial configurations of particle orientations
489 where each 1/3 of particle were injected with major axis parallel to x-, y- and z-direction, respectively.
490 Then when z/D increases from 5 to 20, particle alignment angles tend to move more to 0°. However,
491 this trend does not hold further downstream. When z/D increases to 50, no preferential pattern of particle
492 alignment angles can be seen, and particles are randomly oriented. As previously stated, it is probably
493 due to velocity gradients, which can be observed from Fig. 12, especially when z/D ranges from 5 to 20,
494 making particles more preferably aligned to 0° (flow direction). At axial location of $z/D = 50$, no
495 significant axial velocity gradients can be seen in Fig. 12, making particle alignment isotropic. This
496 argument is further supported by Fig. 14, where alignment angles for particles at axial position of $z/D =$
497 5 are sampled and plotted separately, depending on whether the sampled particle is within or outside the
498 radial location of $r/D = 2$. Particles at radial positions $r/D \leq 2$ tend to have alignment angles closer to 0°
499 (see Fig. 14) and the gas flow at the radial position of $r/D \leq 2$ exhibits large gradients in axial velocities
500 (see Fig. 12), compared to what is observed for $r/D > 2$. One can therefore conclude that particle
501 orientations are dependent on gas flow velocity gradient.
502
503 *4.2.4. Syngas production and particle residence time*
504 As demonstrated above, the spheroidal particle approach affects the histories of the particle through
505 the reactor domain. In order to investigate the effect on the final gas composition at outlet, mass fractions

506 of CO are shown in Fig. 15 to indicate syngas productions in the entrained flow reactor. At axial location
507 of $z/D = 0 – 15$ where devolatilization are expected to be dominant, especially in the central radial region,
508 mass fractions of syngas increase rapidly. As z/D increases further, char conversion, which is
509 comparably slower, plays a more important role, and mass fractions of CO increase much slower and
510 more evenly along the radial direction. When comparing the four cases, one can see that their differences
511 are most pronounced at axial location of $z/D = 5$. *Case 4* (spheroidKG) has the highest mass fractions
512 of syngas, *Case 3* (spheroidRM) comes second, while *Case 1* (sphere) and *Case 2* (nonSphere) come
513 last. This agrees with what is observed in Fig. 10 regarding particle masses. Around the similar axial
514 location, *Case 4* (spheroidKG) has the highest mass loses, thus release more CO. The mass fractions of
515 *Case 1* (sphere) and *Case 2* (nonSphere) catch up later at axial location of $z/D = 10 – 20$, due to the
516 delay of particle thermochemical conversions. Around these axial locations, particles in *Case 1* (sphere)
517 and *Case 2* (nonSphere) are still in the middle of devolatilization, whereas particles in *Case 3*
518 (spheroidRM) and *Case 4* (spheroidKG) are comparably more subject to the slower char conversions.
519 As z/D increases further, mass fractions of CO are almost the same for all the cases. One can postulate
520 that most particles enter char conversion processes there, their particle masses and surface areas are
521 much less when compared to their initial values, hence the differences in particle hydrodynamic models
522 and heat transfer models are much less relevant. In addition, it seems that particle residence time plays
523 a more important role. In Fig. 16, particle ages along reactor radial direction at reactor outlet ($z/D = 70$)
524 are plotted. Particle age is defined as the time taken from injection to measurement and can therefore be
525 used to represent particle residence time. It can be seen that particles with spheroidal shape assumptions
526 have shorter residence times than the others. This corresponds to the observation of Fig. 12 that particles
527 with spheroidal shape assumptions have higher axial velocities at axial location of $z/D = 5 – 20$. Based
528 on post-processing calculations, the average residence times of particles sampled in Fig. 16 for *Case 1*
529 *– 4* are 4.5 s, 4.0 s, 2.8 s and 2.8 s, respectively. Residence times of *Case 3* (spheroidRM) and *Case 4*
530 (spheroidKG) are almost the same. This means that particle residence time is insensitive to the choice
531 of heat transfer model. Since particle residence time is connected to particle motion, such results also
532 indicate that the choice of heat transfer model does not alter particle hydrodynamics significantly.
533 However, the residence times of *Case 1* (sphere) and *Case 2* (nonSphere) are 61 % and 43 % longer

than *Case 4* (spheriodKG), respectively. This is due to the different hydrodynamic models employed. It should be noted that residence time plays an important role in chemical reactions. Even though particles in cases of spheroidal shape assumptions have more surface area for mass and heat transfer, *Case 1* (sphere) and *Case 2* (nonSphere) have longer particle residence times for particles to react, which is very relevant for slow process like char conversion.

However, it would be wrong to conclude that the choices of models of particle shape, hydrodynamics and heat transfer are not important. Particularly, if localized information of particles inside the reactor is more of interest, for example, for optimizing gasifier operation based on localized information (such as sintering at the walls), different model selections yield to different results, as stated above. But it seems that the tested particle models do not affect the syngas production rate at the outlet under current operating conditions. This most likely is due to the simplification applied in the study. For example, an isothermal boundary condition was configured in the simulations, based on the average value from only a few measurement points in the experiments. However, gasifiers in reality are expected to be operated in autothermal mode, thus the temperature of the gasifier wall is directly influenced by the particle conversion, instead of remaining constant in the current simulations. Moreover, current simulations use simplified chemical kinetic models, which might be insensitive to the differences of current four model configurations. Therefore, it is reasonable to believe differences in syngas production can be anticipated in future work if these potential issues could be properly addressed.

5. Conclusions

In this work, a new spheroid model for particle hydrodynamics, a heat transfer model for spheroids and a new set of parameters for devolatilization kinetics have been implemented in OpenFOAM. Simulations and experiments of a laminar flow drop tube reactor have been conducted. Based on the comparisons between experiments and simulations, the three new models have been further validated under reactive conditions. In addition, simulations with configurations similar to an entrained flow gasifier have been executed. Four different approaches involving different particle shapes, hydrodynamics and heat transfer models have been employed for quantitative comparison analyses. The spheroidal particle shape assumption with adjusted spheroidal surface area and the Kishore-Gu model

proves to favor particle thermochemical conversions, especially during drying and devolatilization process. However, the sphere and simplified non-sphere model predict 61 % and 43 % longer residence times, respectively, than the spheroid models, and longer residence time seems to favor the char conversion process. These factors have opposite effects on the total thermal conversion of the biomass particles and seem to compensate each other, making the overall syngas production at the outlet less affected by the choice of models, even though their differences are clearly seen in otherwise located regions. This could be caused by the isothermal temperature configuration at the walls and simplified chemical kinetics employed in the simulations. Particle orientation's dependency on velocity gradients even under reactive conditions are repeatedly found, agreeing with other researchers' work under non-reactive conditions.

Acknowledgement

The authors would like to acknowledge Research Council of Norway and industrial partners to fund this work via GAFT project (No. 244069). Moreover, the authors greatly appreciate Norrbotten Research Council and Kempe Foundation in Sweden for supporting the experimental campaign carried in this work. We also extend our gratitude to Dr. Kathrin Weber for useful discussions of biomass properties. Furthermore, UNINET Sigma2 and NTNU HPC Group provided high-performance computational resources for CFD simulations.

581 Nomenclature

Notation	Description
A	Pre-exponetional factor [s^{-1}]
d_{eq}	Equivalent diameter [m]
D	Diameter of inner central tube in Section 4 [mm]
E	Activation Energy [$J \cdot kmol^{-1}$]
KG	The Kishore-Gu model
m	Mass
m_{devol}	Remaining volatile in the particle [kg]
Nu	Nusselt number
Pr	Prandtl number
R	Universal gas constant [$J \cdot k^{-1} \cdot kmol^{-1}$]
RM	The Ranz-Marshall model
r	Radial position [m]
Re	Reynolds number
T_p	Particle temperature [K]
x, y, z	x, y, z (or axial) position [m]
λ	Particle aspect ratio
τ	Tangential position [m]
0	Initial stage

582

583

584 References

585 [1] IEA. CO2 Emissions from Fuel Combustion 2018. Paris: OECD; 2018.
586 https://doi.org/10.1787/co2_fuel-2018-en.

587 [2] Liaquat AM, Kalam MA, Masjuki HH, Jayed MH. Potential emissions reduction in road
588 transport sector using biofuel in developing countries. Atmos Environ 2010.
589 https://doi.org/10.1016/j.atmosenv.2010.07.003.

590 [3] Zwart RWR, Boerrigter H, van der Drift A. The impact of biomass pretreatment on the
591 feasibility of overseas biomass conversion to Fischer-Tropsch products. Energy and Fuels
592 2006;20:2192–7. https://doi.org/10.1021/ef060089f.

593 [4] Sikarwar VS, Zhao M, Clough P, Yao J, Zhong X, Memon MZ, et al. An overview of advances
594 in biomass gasification. Energy Environ Sci 2016;9:2939–77.
595 https://doi.org/10.1039/C6EE00935B.

596 [5] Li T, Wang L, Ku X, Güell BM, Løvås T, Shaddix CR. Experimental and modeling study of
597 the effect of torrefaction on the rapid devolatilization of biomass. Energy and Fuels
598 2015;29:4328–38. https://doi.org/10.1021/acs.energyfuels.5b00348.

599 [6] Gubba SR, Ma L, Pourkashanian M, Williams A. Influence of particle shape and internal
600 thermal gradients of biomass particles on pulverised coal/biomass co-fired flames. Fuel Process
601 Technol 2011;92:2185–95. https://doi.org/10.1016/j.fuproc.2011.07.003.

602 [7] Panahi A, Levendis YA, Vorobiev N, Schiemann M. Direct observations on the combustion
603 characteristics of Miscanthus and Beechwood biomass including fusion and spherodization.
604 Fuel Process Technol 2017;166:41–9. https://doi.org/10.1016/j.fuproc.2017.05.029.

605 [8] Gao X, Zhang Y, Li B, Yu X. Model development for biomass gasification in an entrained flow
606 gasifier using intrinsic reaction rate submodel. Energy Convers Manag 2016;108:120–31.
607 https://doi.org/10.1016/j.enconman.2015.10.070.

608 [9] Ku X, Jin H, Lin J. Comparison of gasification performances between raw and torrefied
609 biomasses in an air-blown fluidized-bed gasifier. Chem Eng Sci 2017;168:235–49.
610 https://doi.org/10.1016/j.ces.2017.04.050.

[10] Simone M, Biagini E, Galletti C, Tognotti L. Evaluation of global biomass devolatilization kinetics in a drop tube reactor with CFD aided experiments. Fuel 2009;88:1818–27. https://doi.org/10.1016/j.fuel.2009.04.032.

[11] Zhang W, Watanabe H, Kitagawa T. Direct numerical simulation of ignition of a single particle freely moving in a uniform flow. Adv Powder Technol 2017;28:2893–902. https://doi.org/10.1016/j.apt.2017.08.016.

[12] Zhang W, Tainaka K, Ahn S, Watanabe H, Kitagawa T. Experimental and numerical investigation of effects of particle shape and size distribution on particles' dispersion in a coaxial jet flow. Adv Powder Technol 2018. https://doi.org/10.1016/j.apt.2018.06.008.

[13] Zhang W, Watanabe H, Kitagawa T. Numerical investigation of effects of particle shape on dispersion in an isotropic turbulent flow. Adv Powder Technol 2018;29:2048–60. https://doi.org/10.1016/j.apt.2018.05.011.

[14] Riaza J, Gibbins J, Chalmers H. Ignition and combustion of single particles of coal and biomass. Fuel 2017;202:650–5. https://doi.org/10.1016/J.FUEL.2017.04.011.

[15] Lu H, Ip E, Scott J, Foster P, Vickers M, Baxter LL. Effects of particle shape and size on devolatilization of biomass particle. Fuel 2010;89:1156–68. https://doi.org/10.1016/J.FUEL.2008.10.023.

[16] Trubetskaya A, Beckmann G, Wadenbäck J, Holm JK, Velaga SP, Weber R. One way of representing the size and shape of biomass particles in combustion modeling. Fuel 2017;206:675–83. https://doi.org/10.1016/J.FUEL.2017.06.052.

[17] Haider A, Levenspiel O. Drag coefficient and terminal velocity of spherical and nonspherical particles. Powder Technol 1989;58:63–70. https://doi.org/10.1016/0032-5910(89)80008-7.

[18] Zastawny M, Mallouppas G, Zhao F, van Wachem B. Derivation of drag and lift force and torque coefficients for non-spherical particles in flows. Int J Multiph Flow 2012;39:227–39. https://doi.org/10.1016/j.ijmultiphaseflow.2011.09.004.

[19] Rosendahl L. Using a multi-parameter particle shape description to predict the motion of non-spherical particle shapes in swirling flow. Appl Math Model 2000;24:11–25. https://doi.org/10.1016/S0307-904X(99)00023-2.

639 [20] Hölzer A, Sommerfeld M. New simple correlation formula for the drag coefficient of non-
640 spherical particles. Powder Technol 2008;184:361–5.
641 https://doi.org/10.1016/j.powtec.2007.08.021.
642 [21] Jeffery GB. The Motion of Ellipsoidal Particles Immersed in a Viscous Fluid. Proc R Soc A
643 Math Phys Eng Sci 1922;102:161–79. https://doi.org/10.1098/rspa.1922.0078.
644 [22] Guo N, Li T, Zhao L, Løvås T. Eulerian-Lagrangian simulation of pulverized biomass jet using
645 spheroidal particle approximation. Fuel 2019;239:636–51.
646 https://doi.org/10.1016/j.fuel.2018.10.137.
647 [23] Li J, Zhang J. Analytical study on char combustion of spheroidal particles under forced
648 convection. Powder Technol 2017;313:210–7. https://doi.org/10.1016/j.powtec.2017.02.054.
649 [24] Tabet F, Gökalp I. Review on CFD based models for co-firing coal and biomass. Renew
650 Sustain Energy Rev 2015;51:1101–14. https://doi.org/10.1016/J.RSER.2015.07.045.
651 [25] Bhuiyan AA, Naser J. Computational modelling of co-firing of biomass with coal under oxy-
652 fuel condition in a small scale furnace. Fuel 2015;143:455–66.
653 https://doi.org/10.1016/J.FUEL.2014.11.089.
654 [26] Bonefacic I, Frankovic B, Kazagic A. Cylindrical particle modelling in pulverized coal and
655 biomass co-firing process. Appl Therm Eng 2015;78:74–81.
656 https://doi.org/10.1016/j.applthermaleng.2014.12.047.
657 [27] Yin C, Rosendahl L, K. Kær S, J. Condra T. Use of numerical modeling in design for co-firing
658 biomass in wall-fired burners. Chem Eng Sci 2004;59:3281–92.
659 https://doi.org/10.1016/J.CES.2004.04.036.
660 [28] Ku X, Li T, Løvås T. Eulerian–Lagrangian Simulation of Biomass Gasification Behavior in a
661 High-Temperature Entrained-Flow Reactor. Energy & Fuels 2014;28:5184–96.
662 https://doi.org/10.1021/ef5010557.
663 [29] Ku X, Li T, Løvås T. Effects of Particle Shrinkage and Devolatilization Models on High-
664 Temperature Biomass Pyrolysis and Gasification. Energy and Fuels 2015;29:5127–35.
665 https://doi.org/10.1021/acs.energyfuels.5b00953.

[30] Ku X, Li T, Løvås T. CFD-DEM simulation of biomass gasification with steam in a fluidized bed reactor. Chem Eng Sci 2015;122:270–83. https://doi.org/10.1016/j.ces.2014.08.045.

[31] Johansen JM, Jensen PA, Glarborg P, De Martini N, Ek P, Mitchell RE. High Heating Rate Devolatilization Kinetics of Pulverized Biomass Fuels. Energy and Fuels 2018;32:12955–61. https://doi.org/10.1021/acs.energyfuels.8b03100.

[32] Ranz WE, Marshall Jr. WR. Evaporation from drops - Part I. Chem Eng Prog 1952.

[33] Ranz WE, Marshall Jr. WR. Evaporation from drops - Part II. Chem Eng Prog 1952.

[34] Kishore N, Gu S. Effect of Blockage on Heat Transfer Phenomena of Spheroid Particles at Moderate Reynolds and Prandtl Numbers. Chem Eng Technol 2011;34:1551–8. https://doi.org/10.1002/ceat.201100007.

[35] Kriebitzsch S, Richter A. LES simulation of char particle gasification at Reynolds numbers up to 1000. Combust Flame 2020;211:185–94. https://doi.org/10.1016/J.COMBUSTFLAME.2019.08.028.

[36] Johansen JM, Gadsbøll R, Thomsen J, Jensen PA, Glarborg P, Ek P, et al. Devolatilization kinetics of woody biomass at short residence times and high heating rates and peak temperatures. Appl Energy 2016;162:245–56. https://doi.org/10.1016/j.apenergy.2015.09.091.

[37] Li T, Niu Y, Wang L, Shaddix C, Løvås T. High temperature gasification of high heating-rate chars using a flat-flame reactor. Appl Energy 2018;227:100–7. https://doi.org/10.1016/j.apenergy.2017.08.075.

[38] Tolvanen H, Keipi T, Raiko R. A study on raw, torrefied, and steam-exploded wood: Fine grinding, drop-tube reactor combustion tests in N2/O2 and CO2/O2 atmospheres, particle geometry analysis, and numerical kinetics modeling. Fuel 2016;176:153–64. https://doi.org/10.1016/j.fuel.2016.02.071.

[39] Elfasakhany A, Tao L, Espenas B, Larfeldt J, Bai XS. Pulverised wood combustion in a vertical furnace: Experimental and computational analyses. Appl Energy 2013;112:454–64. https://doi.org/10.1016/j.apenergy.2013.04.051.

[40] Njobuenwu DO, Fairweather M. Simulation of inertial fibre orientation in turbulent flow. Phys Fluids 2016;28:063307. https://doi.org/10.1063/1.4954214.

694 [41] Simonsson J, Bladh H, Gullberg M, Pettersson E, Sepman A, Ögren Y, et al. Soot
695 Concentrations in an Atmospheric Entrained Flow Gasifier with Variations in Fuel and Burner
696 Configuration Studied Using Diode-Laser Extinction Measurements. Energy & Fuels
697 2016;30:2174–86. https://doi.org/10.1021/acs.energyfuels.5b02561.
698 [42] Thunman H, Niklasson F, Johnsson F, Leckner B. Composition of volatile gases and
699 thermochemical properties of wood for modeling of fixed or fluidized beds. Energy and Fuels
700 2001;15:1488–97. https://doi.org/10.1021/ef010097q.
701 [43] Haseli Y, van Oijen JA, de Goey LPH. A detailed one-dimensional model of combustion of a
702 woody biomass particle. Bioresour Technol 2011;102:9772–82.
703 https://doi.org/10.1016/j.biortech.2011.07.075.
704
705

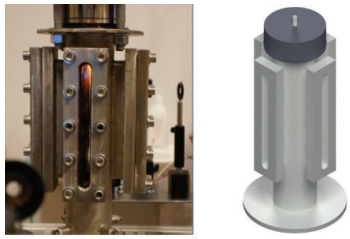

706

707 Fig. 1 Lab-scale flat flame drop tube reactor (a) photo; (b) simplified 3D illustration.

708

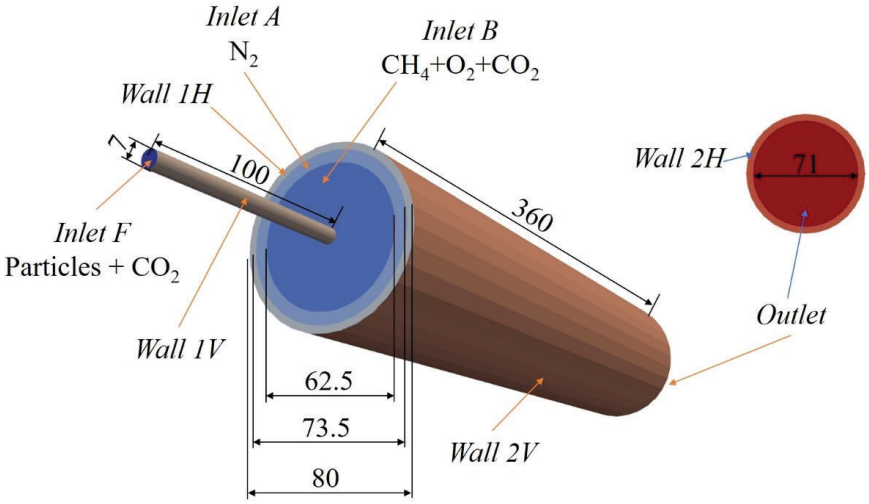

709

710 Fig. 2 Simulation geometry of the flat flame drop tube reactor. Dimension unit: mm.

711

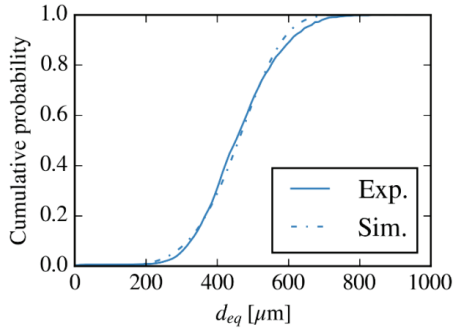

712

713 Fig. 3 Particle size distribution. “Exp.” and “Sim.” represent experiment and simulation data,
714 respectively. d_{ep} is particle equivalent diameter.

715

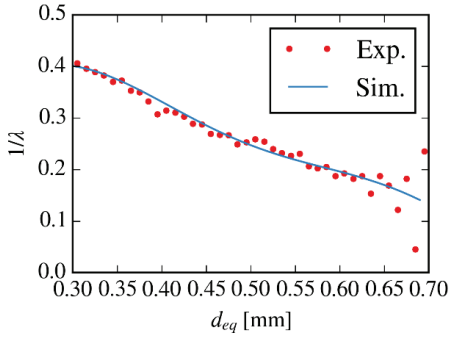

716

717 Fig. 4 The relationship between particle aspect ratio, λ, and equivalent diameter, d_{eq}. Only particles
718 with equivalent diameter of 0.3 – 0.7 mm are shown in this figure as they make up around 90% of all
719 the particles. "Exp." and "Sim." represent experiment and simulation data, respectively.

720

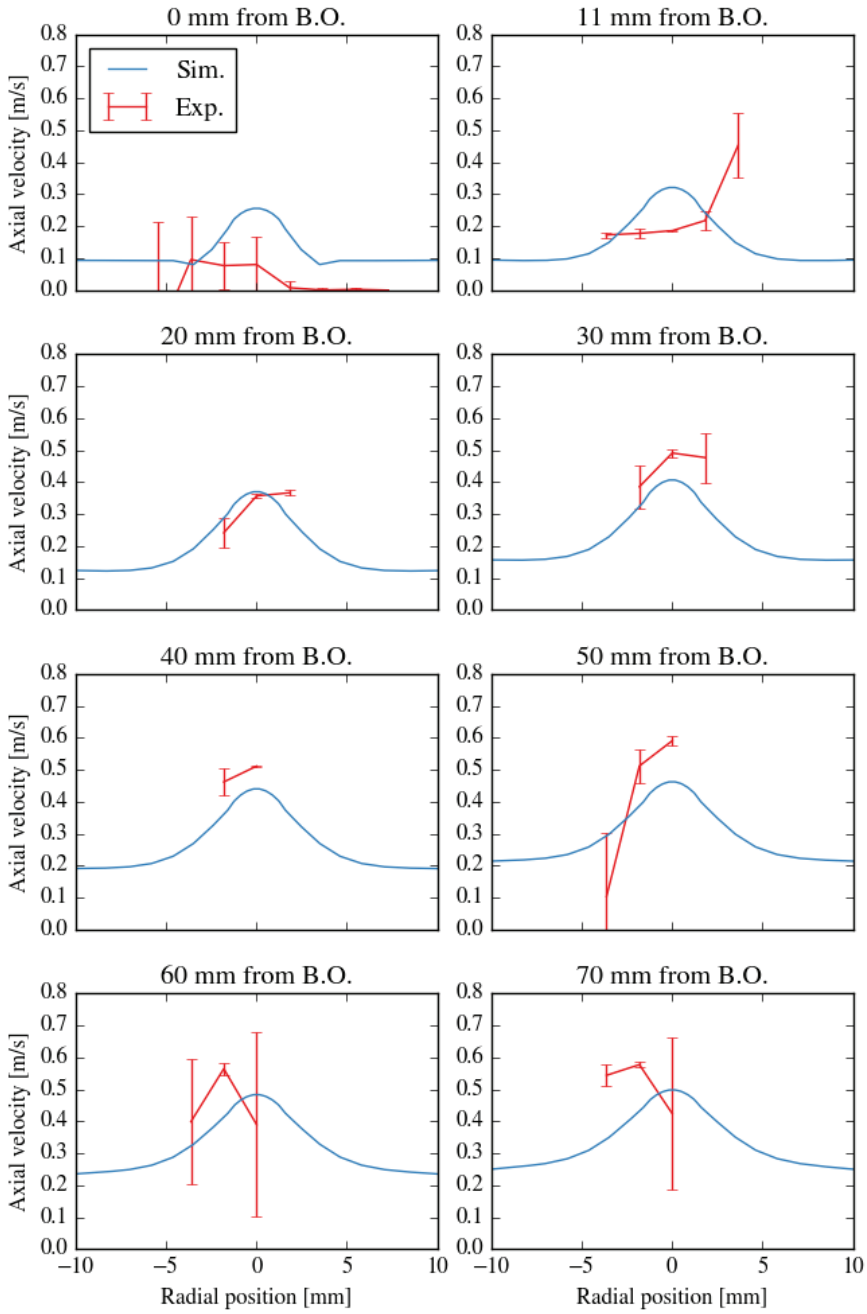

Fig. 5 Axial velocities of gas flow fields along the radial direction of reactor at different positions away from burner outlet under non-reactive conditions without injecting biomass particles. TiO_2, injected through *Inlet F*, acts as tracer particles to obtained velocity data in the experiment. "B.O." stands for burner outlet where Inlet *B* is located. "Sim." and "Exp." mean simulations and experiments, respectively, and are marked by blue and red solid lines, respectively. Error bars represent standard deviations.

728

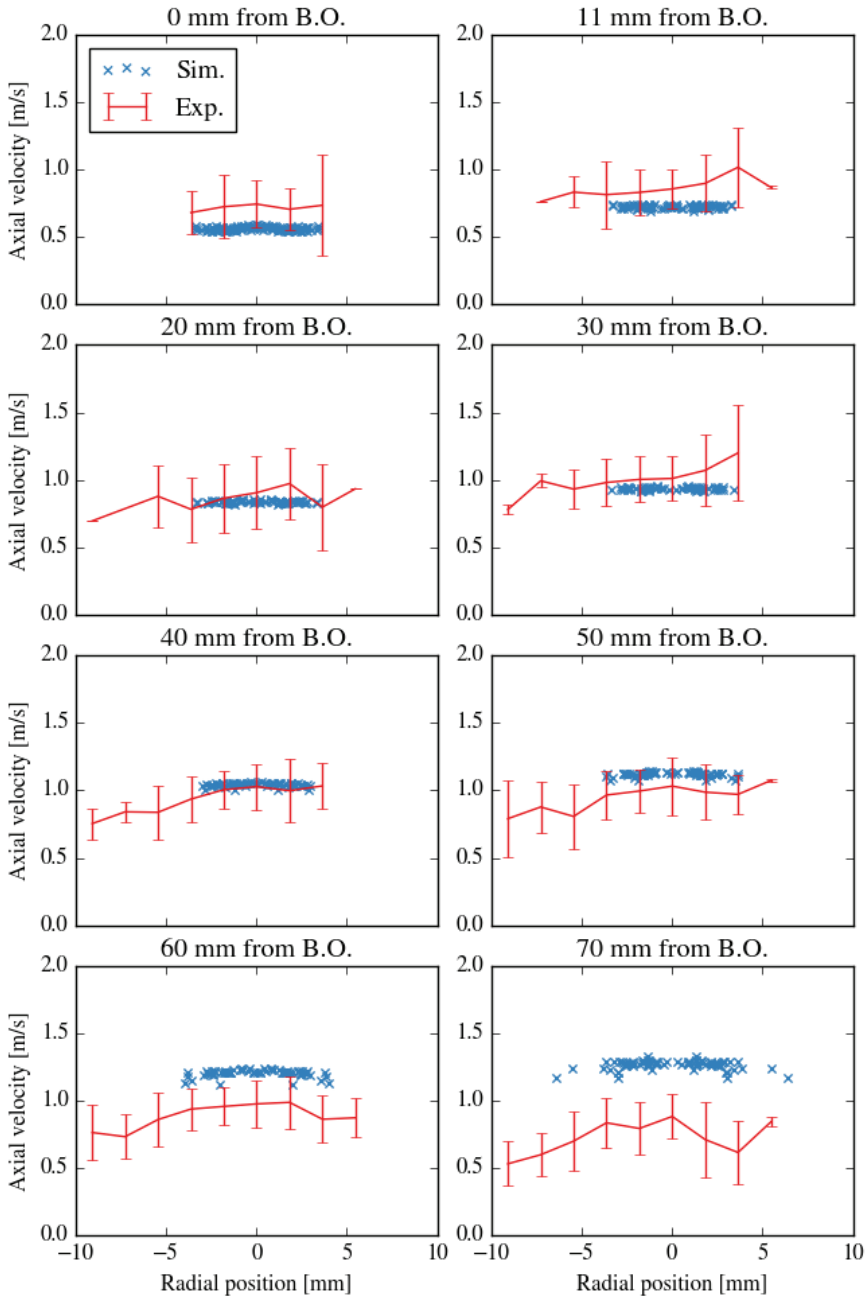

729

730 Fig. 6 Axial velocities of biomass particles along reactor radius at different positions away from
731 burner outlet under reactive conditions. “B.O.” stands for burner outlet. “Sim.” and “Exp.” mean
732 simulations and experiments, respectively, and are marked by blue crosses and red solid lines,
733 respectively. Error bars represent standard deviations.

734

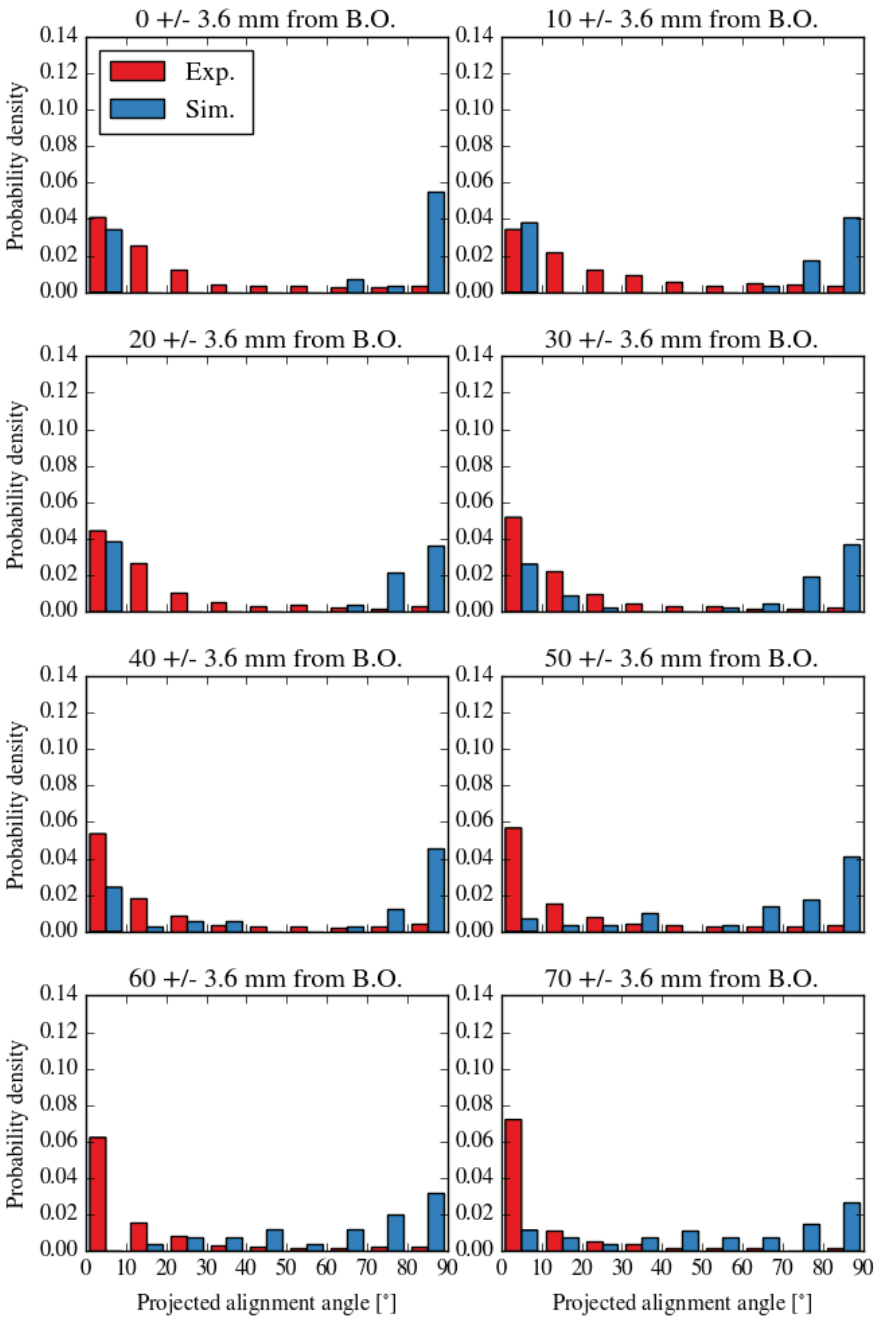

735

736 Fig. 7 Probability density of projected alignment angle of biomass particles at different positions away
737 from burner outlet under reactive conditions. “B.O.” stands for burner outlet. “Exp.” and “Sim.” mean
738 experiments and simulations, respectively, and are marked by red and blue bars, respectively.

739

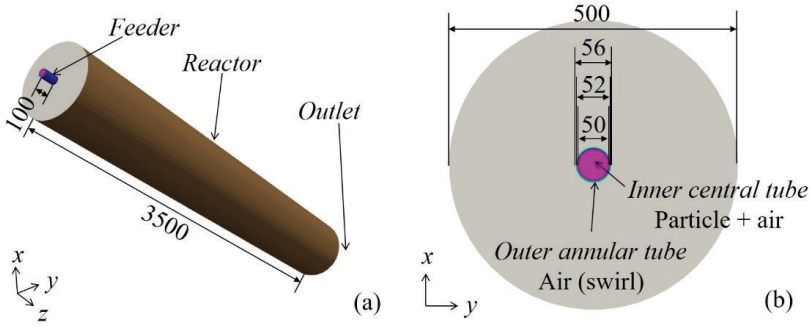

740

741 Fig. 8 Simulation geometry in (a) 3D and (b) *xy*-plane, based on experiments from Simonsson et al.
742 [41]. Dimension unit: mm.

743

744

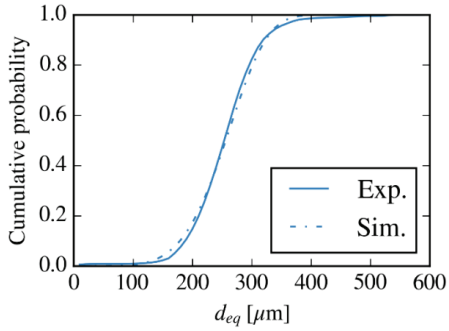

745

746 Fig. 9 Particle size distribution. “Exp.” and “Sim.” represent experiment and simulation data,
747 respectively. d_{ep} is particle equivalent diameter.

748

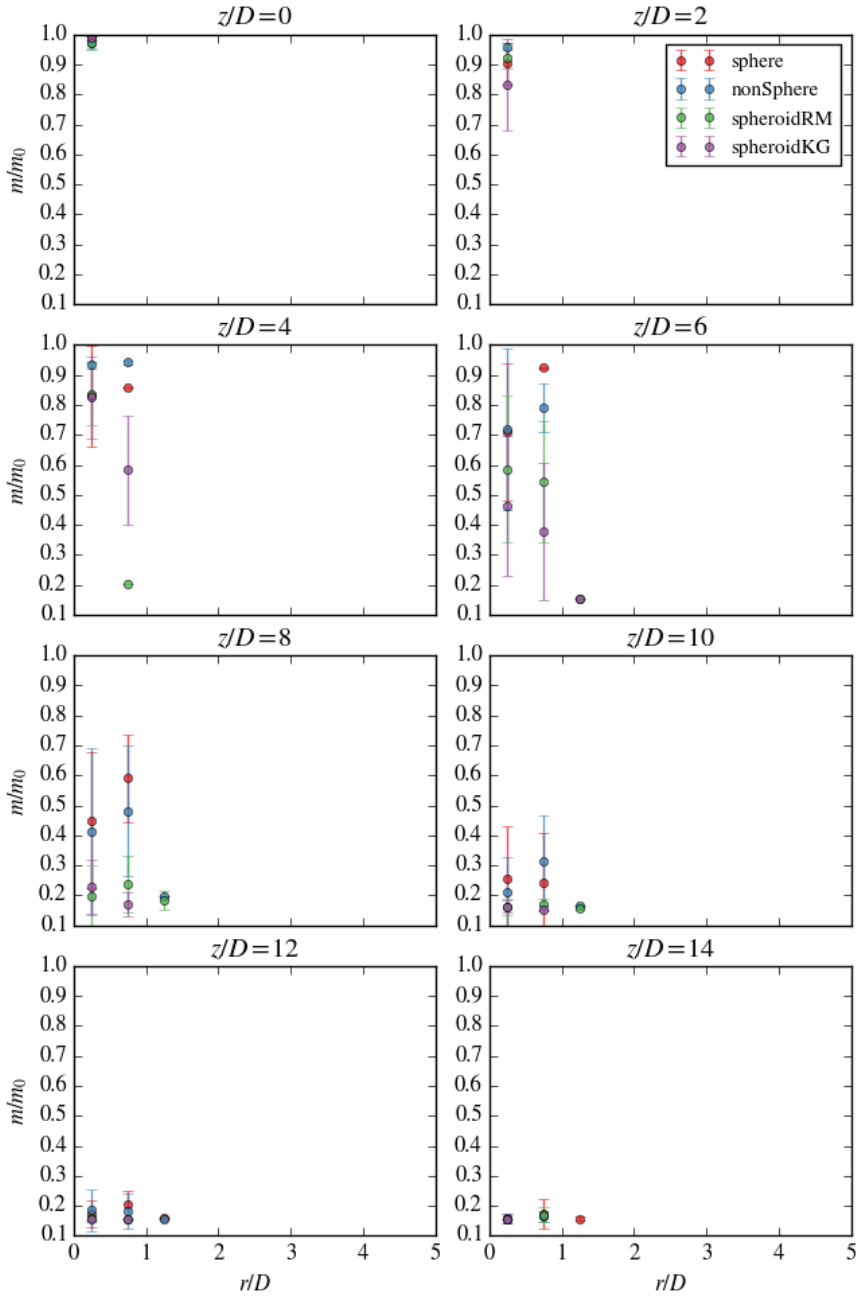

749

750 Fig. 10 Normalized particle mass along reactor radius (*r/D*) at different height (*z/D*) along the reactor.
751 Round dots with error bars are average normalized masses for particles and their standard deviations.

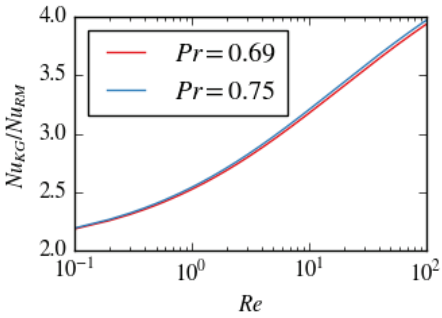

752

753 Fig. 11 Nusselt number, *Nu*, ratio predicted by two heat transfer models at different Prandtl number,
754 *Pr*, and Reynolds number, *Re.* Subscript *KG* and *RM* represent the Kishore-Gu and Ranz-Marshall
755 model, respectively. Particle aspect ratio is 10. The validity for the ranges of *Pr* and *Re* is discussed in
756 Section 2.2.

757

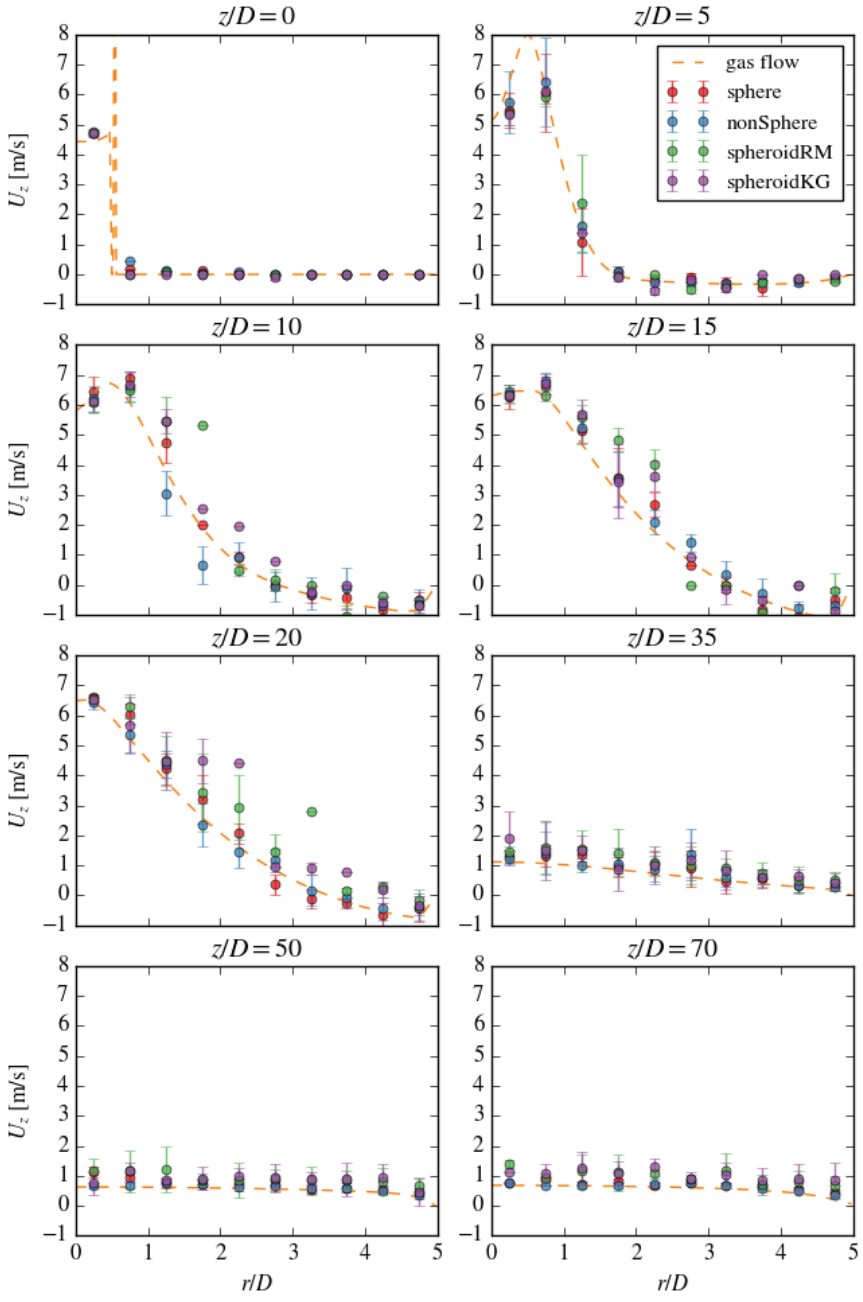

Fig. 12 Axial velocities of gas flow and all particles along reactor radius (*r/D*) at different height (*z/D*) along the reactor. Different color represents difference cases as shown in the legend. Round dots with error bars are particle average velocities and their standard deviations. Dash lines are flow field velocities.

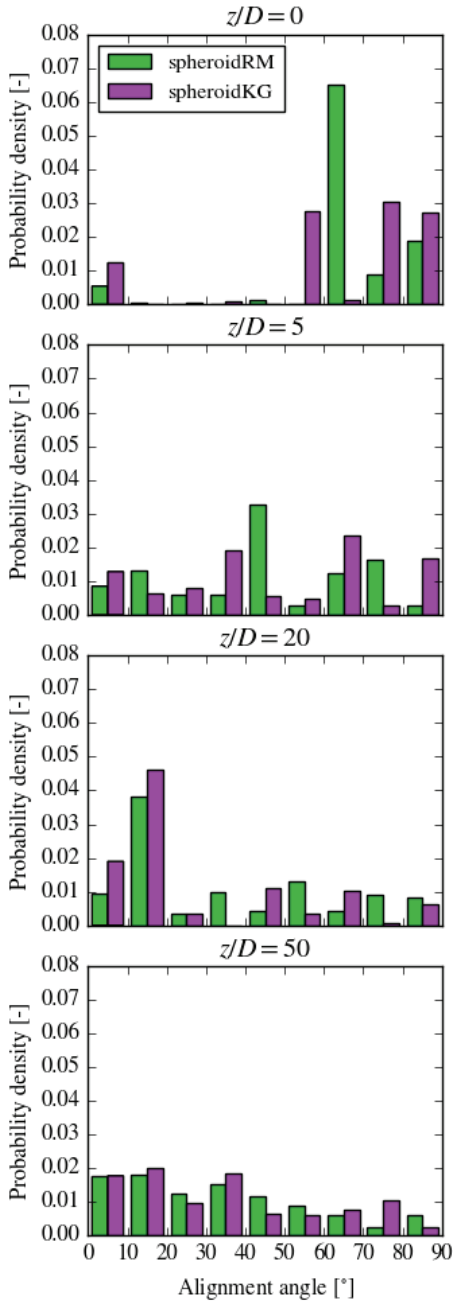

764

765 Fig. 13 Probability density of particle alignment angle at different height (*z/D*) of the reactor.

766

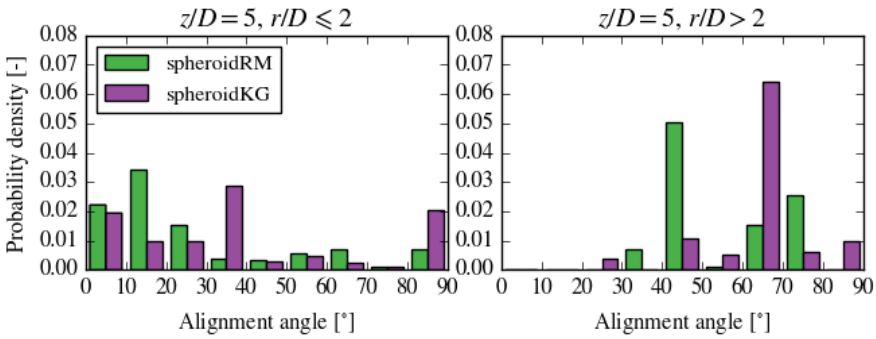

767

768 Fig. 14 Probability density of particle alignment angle at axial location of z/D = 5; (a) only include
769 particles at the radial position of $r/D \leq 2$; (b) only include particles at the radial position of $r/D > 2$.

770

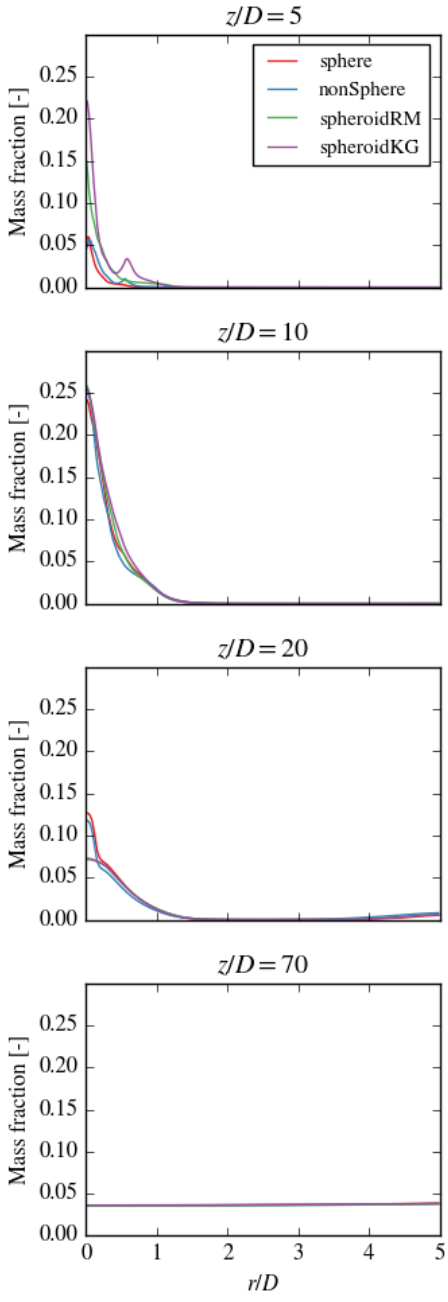

771

772 Fig. 15 Mass fractions of CO along reactor radius (*r/D*) at different height of reactor (*z/D*)

773

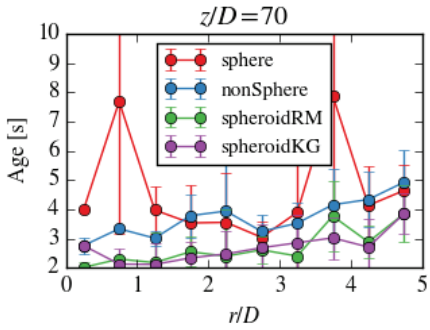

774

775 Fig. 16 Particle age along reactor radius at z/D = 70 (outlet). Round dots with error bars are particle
776 average ages and their standard deviations.

777

778 Table 1 Gases injected via different inlets. The unit "slpm" means standard liter per minute.

Location	Parameter	Unit	N_2	CO_2	CH_4	H_2	O_2	CO	H_2O
Inlet A	Volume flow rate	slpm	6.79	-	-	-	-	-	-
Inlet B (experiment)	Volume flow rate	slpm	-	3.58	4.29	-	5.36	-	-
Inlet B (simulation, post-flame)	Mass fraction	%	-	33.9	-	0.8	0.1	33.9	31.3
Inlet F	Volume flow rate	slpm	-	0.272	-	-	-	-	-

779

780

781 Table 2 Particle composition in the simulations of drop-tube reactor. Volatile gases and their
782 percentages are based on the Beechwood data from Ku et al. [28].

Component	Mass fraction
Volatile	81.16%
CH_4	14.77%
H_2	2.39%
CO_2	33.57%
CO	30.42%
Moisture	0% (dried wood)
Fixed carbon	18.42%
Ash	0.42%

783

784

785 Table 3 Particle composition in the simulations of entrained flow gasifier. Volatile gases and their
786 percentages are based on the data from Thunman et al. [42], which is summarized in Haseli et al. [43].

Component	Mass fraction
Volatile	76.90%
H_2	0.54%
CO	31.84%
CO_2	14.30%
H_2O	14.30%
CH_4	15.92%
Moisture	7.70%
Fixed carbon	15.10%
Ash	0.30%

787

788

789 Table 4 Particle model configurations in different simulation cases

Case No.	Case name	Particle shape	Particle hydrodynamics	Particle heat transfer	Surface area in char surface reaction
1	sphere	Sphere	The sphere model	Ranz-Marshall	Sphere of equivalent volumes
2	nonSphere	Non-sphere	The simplified non-sphere model	Ranz-Marshall	Sphere of equivalent volumes
3	spheroidRM	Spheroid	The spheroid model	Ranz-Marshall	Spheroid of equivalent volumes
4	spheroidKG	Spheroid	The spheroid model	Kishore-Gu	Spheroid of equivalent volumes

790

Supplementary material

Computational fluid dynamic simulations of thermochemical conversion of pulverized biomass in a dilute flow using spheroidal approximation

Ning Guo[1], Ángel David García Llamas[2], Tian Li[1*], Kentaro Umeki[2], Rikard Gebart[2], Terese Løvås[1]

[1]Department of Energy and Process Engineering, Faculty of Engineering, NTNU - Norwegian University of Science and Technology, Trondheim, Norway

[2]Energy Engineering, Division of Energy Science, Luleå University of Technology, Luleå, Sweden

*Corresponding author. Email: tian.li@ntnu.no; Tel: +47-73592696

Table 1 Chemical reactions and their reaction rates considered in the current simulations, based on the work of Ku et al. [1]. "Ref" means reference. E_a is activation energy [$J \cdot kmol^{-1}$], R is gas constant [$J \cdot K^{-1} \cdot kmol^{-1}$] and T is temperature [K].

Reaction	Reaction rate [$kmol \cdot m^{-3} \cdot s^{-1}$]	E_a[$J \cdot kmol^{-1}$]	Ref
$CH_4 + 2O_2 \rightarrow CO_2 + 2H_2O$	$5.16\times10^{13}T^{-1}[CH_4][O_2]\exp(-E_a/RT)$	1.30×10^8	[2]
$CH_4 + H_2O \rightarrow CO + 3H_2$	$7.0\times10^6[CH_4][H_2O]\exp(-E_a/RT)$	1.26×10^8	[3]
$H_2 + 0.5O_2 \rightarrow H_2O$	$2.2\times10^9[H_2][O_2]\exp(-E_a/RT)$	1.09×10^8	[2]
$CO + 0.5O_2 \rightarrow CO_2$	$1.0\times10^{10}[CO][O_2]^{0.5}[H_2O]^{0.5}\exp(-E_a/RT)$	1.26×10^8	[2]
$CO + H_2O \leftrightarrow CO_2 + H_2$	See below		
Forward	$2.78\times10^3[CO][H_2O]\exp(-E_a/RT)$	1.26×10^7	[2]
Backward	$9.59\times10^4[CO_2][H_2]\exp(-E_a/RT)$	4.66×10^7	[2]
Equilibrium	$0.029\exp(-E_a/RT)$	3.40×10^7	[2]

Reference

[1] Ku X, Li T, Løvås T. Eulerian–Lagrangian Simulation of Biomass Gasification Behavior in a High-Temperature Entrained-Flow Reactor. Energy & Fuels 2014;28:5184–96. https://doi.org/10.1021/ef5010557.

[2] Gómez-Barea A, Leckner B. Modeling of biomass gasification in fluidized bed. Prog Energy Combust Sci 2010;36:444–509. https://doi.org/10.1016/j.pecs.2009.12.002.

[3] Jones WP, Lindstedt RP. Global reaction schemes for hydrocarbon combustion. Combust Flame 1988;73:233–49. https://doi.org/10.1016/0010-2180(88)90021-1.

ISBN 978-82-326-4558-9 (printed version)
ISBN 978-82-326-4559-6 (electronic version)
ISSN 1503-8181

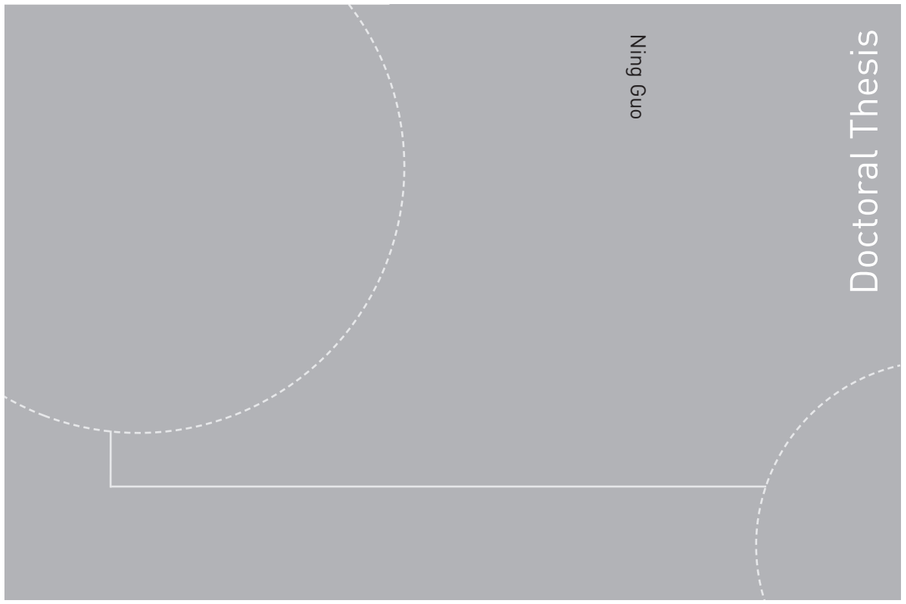

Doctoral theses at NTNU, 2020:103

Ning Guo

Modelling of reacting multi-phase flow for biomass gasification

A realistic approach of particle hydrodynamics and heat transfer under entrained flow gasification conditions

NTNU
Norwegian University of
Science and Technology
Faculty of Engineering
Department of Energy and Process Engineering

Doctoral theses at NTNU, 2020:103

NTNU
Norwegian University of
Science and Technology

NTNU
Norwegian University of
Science and Technology